UNIVERSITY OF THESSALY
FACULTY OF ENFINEERING
DEPARTMENT OF CIVIL ENGINEERING
LABORATORY OF STRUCTURAL ANALYSIS AND DESIGN
MSc APPLIED MECHANICS AND SYSTEMS MODELLING AND SIMULATION

Postgraduate Thesis

Buckling Behavior of Thin Ferrocement Shells

Apostolos I. Koukouselis

Supervisor: Professor Euripidis Mistakidis

July 2013

Examination Committee

Professor E. Mistakidis (Supervisor)
Associate Professor S. Karamanos
Assistant Professor O. Panagouli

Institutional Repository - Library & Information Centre - University of Thessaly
20/05/2024 20:20:43 EEST - 3.139.81.117

Contents

Institutional Repository - Library & Information Centre - University of Thessaly
20/05/2024 20:20:43 EEST - 3.139.81.117

Institutional Repository - Library & Information Centre - University of Thessaly
20/05/2024 20:20:43 EEST - 3.139.81.117

Περίληψη

Το ferrocement, όπως έχει οριστεί από την ACI committee 549 (1999), είναι ένας τύπος οπλισμένου σκυροδέματος αποτελούμενος από πολλαπλές οπλισμικές στρώσεις χάλυβα, μικρής διαμέτρου σε μικρή απόσταση μεταξύ τους και τσιμεντοκονία. Αν και το ferrocement επινοήθηκε από τον Joseph-Louis Lambot το 1848 δεν έτυχε ευρείας χρήσης, μέχρι πρόσφατα, λόγω του αυξημένου κόστους και δυσκολίας παραγωγής πλεγμάτων χάλυβα μικρής διαμέτρου με τα μέσα εκείνης της εποχής. Την τελευταία δεκαετία όμως, η ανάπτυξη στον τομέα τεχνολογίας υλικών έχει κάνει πλέον δυνατή την παραγωγή και διάθεση στην αγορά χάλυβα υψηλής αντοχης αλλά και κονιαμάτων σκυροδέματος υψηλών αντοχών, απλού και ινοπλισμένου.Μία από της σημαντικότερες εφαρμογές του ferrocement είναι η κατασκευή κελυφών και δομικών στοιχείων μικρού πάχους σε επιστεγάσεις και προσόψεις κτιρίων όπου η ελευθερία μορφής για αρχιτεκτονικούς λόγους είναι απαραίτητη. Η παράγραφος 2.1 παρουσιάζει το χρησιμοποιούμενο υλικό και τα χαρακτηριστικά του.

Σε τέτοιου είδους κατασκευές μικρού πάχους, κρίσιμος γίνεται ο σχεδιασμός έναντι απώλειας ευστάθειας. Η έρευνα στην περιοχή του λυγισμού ενισχυμένων κελυφών έχει περιοριστεί όμως κυρίως σε κατασκεύες από δομικό χάλυβα ή παρόμοιων υλικών. Αυτή η εργασία επικεντρώνεται στην διερεύνηση της λυγισμικής συμπεριφοράς ενός κελύφους από ferrocement πάχους 20 και 35 χιλιοστών, το οποίο είναι ενισχυμένο και στις δυο διευθύνσεις με ένα πλέγμα διαδοκίδων. Κατά την διεύθυνση *x* οι διαδοκίδες έχουν ύψος 250 χιλιοστών και η απόσταση μεταξύ τους είναι 2.5 μέτρα, ενώ κατά την διεύθυνση *y* οι διαδοκίδες έχουν ύψος 200 χιλιοστών και η απόσταση μεταξύ τους είναι 625 χιλιοστά. Όλες οι διαδοκίδες έχουν πλάτος 45 χιλιοστών. Σε ρομβοειδή διάταξη, και σε απόσταση 5 μέτρων μεταξύ τους, υπάρχουν στηρίξεις έναντι εκτός επιπέδου μετακινήσεων. Το κέλυφος θεωρείται ότι εκτείνεται στο άπειρο και στις δυο διευθύνσεις ενώ τα χρησιμοποιούμενα υλικά είναι τσιμέντοκονίαμα κατηγορίας C60 και οπλισμικός χάλυβας B500c. Η παράγραφος 2.2 κάνει μια εισαγωγή στον λυγισμό τέτοιου είδους ενισχυμένων κελυφών. Στη παράγραφο 2.3 γίνεται εκτενής παρουσίαση της γεωμετρίας της κατασκευής και των χρησιμοποιούμενων υλικών.

Αν και προφανώς το ferrocement είναι τσιμεντοειδές υλικό, λόγω και της έλλειψης κανονιστικού πλαισίου για τέτοιου είδους κατασκευές από οπλισμένο σκυρόδεμα αλλά και της ομοιότητας της συμπεριφοράς τους σε έναν βαθμό με την συμπεριφορά κελυφών από δομικό χάλυβα, γίνεται χρήση μεθόδων που χρησιμοποιούνται στον σχεδιασμό κελυφών από χάλυβα. Η έντονη μη γραμμικότητα του υλικού όμως, κυρίως λόγω ρηγμάτωσης, καθιστά το συγκεκριμένο πρόβλημα ακόμα πιο περίπλοκο. Εξαιτίας αυτής της πολυπλοκότητας, μία αναλυτική λύση είναι πολύ δύσκολο να επιτευχθεί. Για το λόγο αυτό γίνεται αριθμητική ανάλυση του πρόβλήματος με την μέθοδο των πεπερασμένων στοιχείων, ακολουθώντας την πλήρως αριθμητική προσέγγιση του Ευρωκώδικα 3 μέρος 1.6.

Αρχικά, στο Κεφάλαιο 3, γίνεται μια διερεύνηση της ελαστικής συμπεριφοράς της κατασκευής με ανάλυση λυγισμού στις δυο διευθύνσεις έτσι ώστε να βρεθούν οι κυρίαρχες ιδιομορφές λυγισμού. Η ανεύρεση των αυτών των ιδιομορφών λυγισμού είναι σημαντική καθώς στην συνέχεια χρησιμοποιούνται για τον καθορισμό κατάλληλων περιοδικών συνοριακών συνθηκών ώστε να μειωθεί η μελετούμενη επιφάνεια και επομένως το υπολογιστικό κόστος. Επιπρόσθετα, οι ιδιομορφές αυτές καθορίζουν και το σχήμα των αρχικών ατελειών που χρησιμοποιούνται στην μη γραμμική ανάλυση. Επίσης, γίνεται και μια πρώτη μελέτη της αλληλεπίδρασης των αξονικών φορτίων στις δυο διευθύνσεις στην ελαστική περιοχή ώστε να γίνει κατανοητή η γενικότερη συμπεριφορά που διέπει την κατασκευή. Για την ανάλυση λυγισμού της κατασκευής διερευνώνται τρεις τρόποι προσομοίωσης. Ο πρώτος χρησιμοποιεί επιφανειακά πεπερασμένα για την μόρφωση του προσομοιόματος, ο δεύτερος χωρικά πεπερασμένα στοιχεία, ενώ ο τρίτος χρησιμοποιεί επιφανειακά στοιχεία για την προσομοίωση του κελύφους και γραμμικά για την προσομοίωση της

Institutional Repository - Library & Information Centre - University of Thessaly
20/05/2024 20:20:43 EEST - 3.139.81.117

σχάρας των διαδοκίδων. Τα αποτελέσματα των τριών αυτών τρόπων προσομοίωσης συγκρίνονται ετσι ώστε να ευρεθεί ο βέλτστος τρόπος προσομοίωσης της κατασκευής.

Στην συνέχεια, στο Κεφάλαιο 4 διερευνάται ο τρόπος προσομοίωσης της διατομής των διαδοκίδων με την οπλισμική διάταξη, ώστε να ληφθει υπόψη η μη γραμμική συμπεριφορά του υλικού, δηλαδή η πλαστικοποίηση και η ρηγμάτωση. Εξετάστηκαν δυο μέθοδοι προσομοίωσης. Ο πρώτος χρησιμοποιεί επιφανειακά πεπερασμένα στοιχεία για την προσομοίωση της μήτρας σκυροδέματος και γραμμικά στοιχεία για του οπλισμούς ενώ ο δεύτερος επιφανειακά σύνθετα (composite) στοιχεία πολλαπλών στρώσεων για την ταυτόχρονη προσομοίωση και των δυο υλικών. Για την διερεύνηση των δυο μεθόδων προσομοιώθηκε ένα πείραμα κάμψης τεσσάρων σημείων με και χωρίς αξονικό φορτίο και τα αποτελέσματα συγκρίθηκαν με αντίστοιχα που προκύπτουν από την ολοκλήρωση των τάσεων της διατομής. Τα δεύτερα, τα οποία θεωρούνται αποτελέσματα αναφοράς, προέκυψαν με την βοήθεια του υποπρογράμματος Section designer του SAP2000 v15.

Ακολούθως, στο Κεφάλαιο 5, η εξετάζεται η ακρίβεια της προσομοίωσης με επιφανειακά σύνθετα στοιχεία πολλαπλών στρώσεων της διατομής του κελύφους. Για την προσομοίωση του κελύφους εξαρχής αποκλείεται η προσομοίωση του οπλισμού με γραμμικά στοιχεία, καθώς κρίσιμη είναι η σωστή προσομοίωση του οπλισμού κατά την διεύθυνση του πάχους της διατομής. Τα αποτελέματα της προσομοίωσης συγκρίνονται και πάλι με αντίστοιχα του Section designer του προγράμματος SAP2000 v15.

Τέλος, στο Κεφάλαιο 6, μορφώθηκε το τελικό προσομοίωμα για την αποτίμηση της οριακής αντοχής του κελύφους με την χρήση επιφανειακών σύμμικτων στοιχείων πολλαπλών στρώσεων, καθώς αυτά κρίθικαν ως ο ενδεδειγμένος τρόπος προσομοίωσης από τα αποτελέσματα των κεφαλαίων 4 και 5, . Επειδή ο λυγισμός κατά την διεύθυνση *x* κρίθηκε πιο κρίσιμος μόνο η συκεκριμμένη διεύθυνση μελετήθηκε περαιτέρω. Αρχικά μελετήθηκαν μοντέλα διαστάσεων και συνοριακών συνθηκών που αντιστοιχούν σε ένα άνω όριο της οριακής αντοχής. Αυτό έγινε ώστε να μειωθούν αρχικά οι αριθμητικές αστάθειες και να γίνει μια πρώτη προσέγγιση του προβλήματος στην ελαστοπλαστική περιοχή. Στην συνέχεια μελετήθηκαν προσομοιώματα που αποδίδουν την πραγματική συμπεριφορά της κατασκεύης. Έτσι με την βοήθεια μη γραμμικών αναλύσεων που λαμβάνουν υπόψη και την γεωμετρική αλλά και την μη γραμμικότητα του υλικού διερευνήθηκε η επιρροή του εύρους των αρχικών ατελειών καθώς και της ύπαρξης αξονικού φορτίου σε δυο διευθύνσεις, στην οριακή αντοχή της κατσκευής.

Τα αποτελέσματα της παρούσας διερεύνησης αναδεικνύουν την πολυπλοκότητα του συγκεκριμένου προβλήματος και παρουσιάζουν ένα τρόπο αντιμετώπισης του με χρήση μεθόδων που χρησιμοποιούνται στο σχεδιασμό κελυφών από χάλυβα. Η ανάλυση λυγισμού της κατασκεύης έδειξε ότι δυο μορφές λυγισμού έιναι κρίσιμες, ο τοπικός λυγισμός μεταξύ διαδοκίδων και ο καθολικός μεταξύ στηρίξεων. Ο κύριος παράγοντας που επηρεάζει την μορφή λυγισμού φαίνεται να είναι ο λόγος της δυσκαμψίας των διαδοκίδων ως προς αυτή του κελύφους. Ο άλλος σημαντικός παράγοντας είναι οι συνοριακές συνθήκες, οι οποίες επηρεάζουν και την αλληλεπίδραση των δυο μορφών λυγισμού. Όσον αφορά στην προσομοίωση του υλικού, τα επιφανειακά σύνθετα στοιχεία πολλαπλών στρώσεων φαίνεται να αποτελούν τον ακριβέστερο τρόπο προσομοίωσης. Για την αποτίμηση της ελαστοπλαστικής αντοχής της κατασκευής, η αριθμητική προσέγγιση του Ευρωκώδικα 3 μέρος 1.6 αποδεικνύεται ικάνη να χρησιμοποιηθεί και σε προβλήματα περά αυτών του δομικού χάλυβα καθώς δεν βασίζεται σε παραδοχές που ισχύουν μόνο για το συγκεκριμένο υλικό. Όπως προέκυψε από τις μη γραμμικές αναλύσεις, το εύρος των αρχικών ατελειών δεν φαίνεται να έχει μεγάλη επιρροή στην οριακή αντοχή. Σημαντική επιρροή έχει η διαφοροποίηση της ατέλειας από άνοιγμα σε άνοιγμα καθώς οδηγεί την κατασκεύη σε πρόωρη αστοχία λόγω συγκέντρωσης της αστοχίας σε συγκεκριμένα φατνώματα. Τέλος, μικρή επιρροή φαίνεται να έχει και η παρουσία αξονικού φορτίου σε δυο διευθύνσεις, φαινόμενο αναμενόμενο για κατασκευές μικρής λυγηρότητας στην μια απο τις δυο διευθύνσεις .

Institutional Repository - Library & Information Centre - University of Thessaly
20/05/2024 20:20:43 EEST - 3.139.81.117

1 Abstract

Ferrocement, as defined by the ACI committee 549 (1999), is a form of reinforced concrete using closely spaced multiple layers of mesh and/or small diameter rods, usually made of steel, completely infiltrated with, or encapsulated, in mortar. One of its most common applications is the manufacturing of shells of small thickness, in which buckling failure may occur.

This study focuses on the investigation of the behavior of a ferrocement shell structure, enhanced in both directions by the means of an appropriate grid of ribs perpendicular to the shell surface. Although ferrocement is a cementitious material, the small thickness of the shell dictates the application of methods usually used in the study of the buckling behavior of steel structures. However, the intrinsic issues of cracking in cementitious composites, make the study of this particular problem even more complicated.

Due to the aforementioned complexity, an analytical method could be quite difficult if not impossible to be applied. Therefore, a numerical approach is imperative. In the present paper the Finite Element Method will be applied. Detailed three-dimensional numerical models will be formulated for the simulation of the behavior of the under study structure, which will be able to take into account both the geometric and the material nonlinearities that are present in the subject at hand. The difference among the formulated simulation models lies on the use of various types of finite elements. The numerical results obtained by each numerical model will be compared and the most efficient model will be determined.

Finally the optimum F.E. model will be then used for the further investigation of the effect of different parameters on the ultimate load capacity. Such parameters are the initial imperfection of the structure and the interaction between the axial loads and bending moments in both directions.

Institutional Repository - Library & Information Centre - University of Thessaly
20/05/2024 20:20:43 EEST - 3.139.81.117

2 Introduction

2.1 Introduction to Ferrocement

Ferrocement is a form of reinforced concrete, widely used in the construction of thin-walled shell structures, that consists of closely spaced multiple layers of mesh and/or small diameter rods, usually made of steel and a hydraulic cement mortar. It was invented by Joseph-Louis Lambot in 1848 and was originally meant to replace construction wood. In order to demonstrate his patent, Lambot actually built two rowboats in 1848 and 1849. Lambot's work, together with Monier's , who during the same period constructed flower pots and garden tubs made of cement and iron rods, can be considered the origin of reinforced concrete (Naamaan (2000)).

Because 19th century technology could not facilitate the production of small diameter rods and meshes, larger diameter rods were used leading to the transition from ferrocement to reinforced concrete. As Naamaan (2000) states in, it was not until the early 1960's that ferrocement finally achieved wide acceptance for boat building and in 1991 the International Ferrocement Society was established at the Asian Institute of Technology in Bangkok.

Nowadays. the applications of ferrocement include both the construction of new structures and the repair and rehabilitation of existing ones. It is widely used in the manufacturing of thin elements and sandwich type construction using thin skins providing light weight, water tightness and impact resistance.

As far as the repair and rehabilitation of structures are considered, ferrocement is commonly used as a low cost and easy to use material for small scale repair work. Moreover, ferrocement can also be used for manufacturing of confinement jacket for R/C columns or skin reinforcement for unreinforced brick or masonry building to improve their seismic resistance.

Figure 2.1 demonstrates a typical ferrocement cross section. Naamaan (2000) provides typical ferrocement cross sections and composition ranges. Table 2.1 (Naaman (2000)) summarizes the most important composition ranges and mechanical properties.

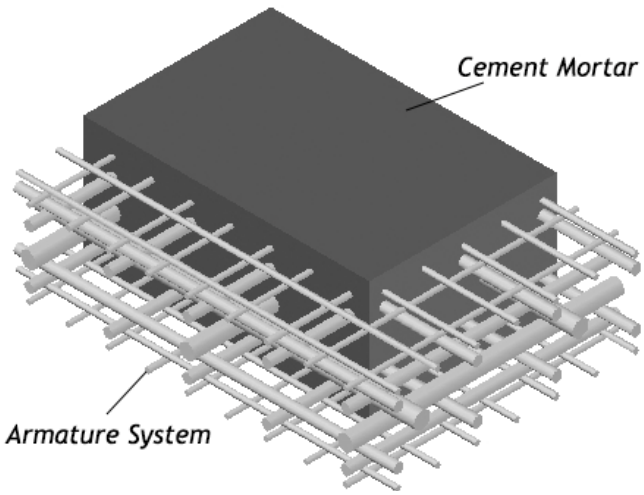

Figure 2.1 Typical ferrocement cross section.

Institutional Repository - Library & Information Centre - University of Thessaly
20/05/2024 20:20:43 EEST - 3.139.81.117

WIRE-MESH REINFORCEMENT	• Wire Diameter:	• $0.5 \le d_w \le 1.5$ mm; ($0.020 \le d_w \le 0.062$ in.)
	• Type of Mesh:	• Square woven or welded galvanized wire mesh; aviary (chicken) wire mesh; or expanded metal mesh
	• Size of Mesh Openings:	• $6 \le D \le 25$ mm ($1/4 \le D \le 1$ in.)
	• Number of Mesh Layers:	• Up to 6 layers per cm of thickness (Up to 14 layers per in. of thickness)
	• Volume Fraction of Reinforcement:	• Up to 8% in both directions corresponding to up to 630 kg/m^3 (40 lb per ft^3) of steel mesh reinforcement
	• Specific Surface of Reinforcement:	• Up to 4 cm^2/cm^3 in both directions (up to 10 in.^{2}/in.^{3} in both directions)
INTERMEDIATE SKELETAL REINFORCEMENT	• Type:	• Wires; wire fabric, rods; strands
	• Diameter:	• $3 \le d_b \le 10$ mm; (1/8 to 3/8 in.)
	• Grid Size:	• $5 \le G \le 15$ cm; ($2 \le G \le 6$ in.)
	Skeletal reinforcement not always present.	
TYPICAL MORTAR COMPOSITION	• Portland Cement:	• Any type depending on application
	• Sand-to-Cement Ratio:	• $1 \le S/C \le 2.5$ by weight
	• Water-to-Cement Ratio:	• $0.35 \le W/C \le 0.6$ by weight
	• Recommendations:	• Fine sand all passing U.S. sieve No. 16 (1.5 mm) and having 5% by weight passing No. 100 (0.25 mm), with a continuous grading curve in-between.
		• Additives: (Fly Ash / C) = 0.2 Air entraining agent; Corrosion inhibitor; Water reducing agent, or Superplasticizer, as needed.
COMPOSITE PROPERTIES	• Thickness:	• $6 \le h \le 50$ mm ; ($1/4 \le h \le 2$ in.) [mostly < 30 mm]
	• Steel Cover:	• $1.5 \le$ cover ≤ 3 mm; ($1/16 \le$ cover $\le 1/8$ in.)
	• Ultimate Tensile Strength:	• Up to 35 Mpa (5,000 psi)
	• Allowable Tensile Stress:	• Up to 14 MPa (2,000 psi)
	• Modulus of Rupture:	• Up to 70 MPa (10,000 psi)
	• Ratio Bending/Tension:	• From 2 to 2.5
	• Compressive Strength:	• 21 to 96 MPa (3,000 to 12,000 psi)

Table 2.1 Composition ranges and mechanical properties of ferrocement (Naaman (2000)).

Institutional Repository - Library & Information Centre - University of Thessaly
20/05/2024 20:20:43 EEST - 3.139.81.117

Materials

The materials used in the production of ferrocement are similar to those used for reinforced concrete constructions. Thus, it is quite clear that the regulations and standards that apply for common R/C structures should be satisfied. The " Guide for the Design, Construction and Repair of Ferrocement" reported by the ACI committee 549 (1999) provides the basic material requirements and in combination with other codes such as ACI 318 "Building Code Requirements for Reinforced Concrete" , Eurocode-2 (2005) and Eurocode-8 fully describe the technical specification and requirements for the construction of quality ferrocement structures.

Matrix

The matrix used in the production of ferrocement consists of mortar made with portland cement, fine aggregate, and water. For special applications various admixtures may be added. As the aforementioned report of the ACI committee states (ACI committee 549 (1999)) , aggregates (sand) should comply with ASTM C 33 requirements or an equivalent standard. It should be clean, inert, free of organic matter and deleterious substances and relatively free of silt and clay. The maximum particle size depends on the distance between the layers and the mesh size and for general applications should not exceed 1.18mm (sieve No 16). 2.2 adopted by ASTM C 33 provides a guideline for its grading, which should be uniform in order to achieve a workable high-density mortar mix.

As shown in table 1.1 usually the sand to cement ratio varies from to 1 to 2.5 and the water to cement ratio from 0.35 to 0.6. Usually, the higher the sand content, the more water is required to achieve the same workability. The mix should be as stiff as possible, without preventing the reinforcing mesh to fully penetrate the matrix . Normally the slumb of fresh mortar should not exceed 50mm.

Sieve Size, U.S. standard square mesh	Percent passing by weight
No. 8 (2.36 mm)	80-100
No. 16 (1.18 mm)	50-85
No 30 (0.60 mm)	25-60
No 50 (0.30 mm)	10-30
No100 (0.15 mm)	2-10

2.2 Grading of the cement mortar according to the ASTM C 33.

Reinforcement

As ACI committee 549 (1999) reports, in order to achieve a high quality final product, the mesh reinforcement should be free from deleterious materials, on the grounds that they may cause the reinforcing wires to slip and thus the ultimate resistance is reduced and brittle failure may occur.

In most cases the reinforcement of ferrocement is a wire mesh (hexagonal or square). Wire meshes with square openings may be welded or woven. Welded-wire meshes have higher modulus and hence stiffness and their thickness is usually 2 wire-diameters(one layer of wires in each direction). However the production procedure of welded-meshes lead to a lower tensile force because of the welding (ACI committee 549 (1999)).

Institutional Repository - Library & Information Centre - University of Thessaly
20/05/2024 20:20:43 EEST - 3.139.81.117

In addition to the reinforcing mesh, skeletal steel is often used in the production of ferrocement elements. Skeletal steel is a grid of steel wires or rods that form the skeleton of the desired shape of the structure. The mesh reinforcement is later attached on the skeletal reinforcement (usually on both sides) which acts as a spacer for the main reinforcement layers. The contribution of skeletal steel in the ultimate resistance of the section is mainly in tension and punching. As far as bending is concerned, because it is placed close to the middle of the section, its contribution is less significant (Naaman (2000)).

Differences between Ferrocement and common reinforced concrete.

Although there are many similarities between ferrocement and reinforced concrete and the general guidelines and standards regarding R/C structures also apply in ferrocement ones, the distinct differences in their behavior should be taken into account during the analysis and design of such elements.

First, as mentioned before, ferrocement is mainly used in the construction of elements of relatively small thickness. Thus, buckling failure, both local and global, should be taken under consideration by the designer.

Next, in contrast to reinforced concrete, ferrocement elements have reinforcement distributed throughout their thickness and in both directions with typical reinforcement ratios that are a lot higher than those of conventional reinforced elements (2- 8 % total or 1 – 4 % in each direction). Those facts lead to an element with

a) high tensile strength (of the same order as the compressive),

b) high ductility that unlike in reinforced concrete elements increases with the increase of the reinforcement ratio and

c) homogeneous-isotropic properties in two directions and high punching shear resistance.

Also because the reinforcement comes in the form of thin wire-meshes and not of thick rods the cracking, and thus bending behavior, behavior differs. Similar to fiber-reinforced concrete elements, the cracking stage (stage II) can be quite extensive sometimes even until the yielding of the mesh (no stage III). Moreover, the crack width and spacing observed in ferrocement is an order of magnitude smaller than that of reinforced concrete. That leads to excellent and durability.

Institutional Repository - Library & Information Centre - University of Thessaly
20/05/2024 20:20:43 EEST - 3.139.81.117

2.2 Introduction to Buckling of Stiffened Shells

Over the years, extensive research has been made in the area of buckling of stiffened steel or aluminium shells especially by engineers in the field of marine and offshore structures. The high compressive and tensile ultimate stress of structural steel and aluminium lead engineers into the construction of structures of small thickness sensitive to buckling. Ferrocement, as a high performance composite material, also finds application in such lightweight structures of small thickness but little research is made concerning the buckling behavior of ferrocement structures. Although the same analysis and design principals also apply in ferrocement stiffened shells certain parameters such as cracking may differentiate their behavior and need to be taken under consideration.

Important parameters in the behavior of stiffened shell are

- The geometry and spacing of the stiffeners
- The aspect ratio of the shell between the stiffeners
- The thickness of the shell
- The boundary conditions

In the analysis of such stiffened shells, as mentioned in the relevant literature (Ventsel and Krauthammer (2001); Tvergaard V. (1973); Stamatelos et al (2011); Paik et al (2008)), three cases may appear (Figure 2.2):

a) Global buckling modes, which are dominant in the case of rather thick shells

b) Local buckling modes of the shell between the stiffeners. These modes are dominant in cases of thin shells under the presence of strong stiffeners.

c) Mixed buckling modes. These modes arise in case of thin shells stiffened by relatively weak stiffeners.

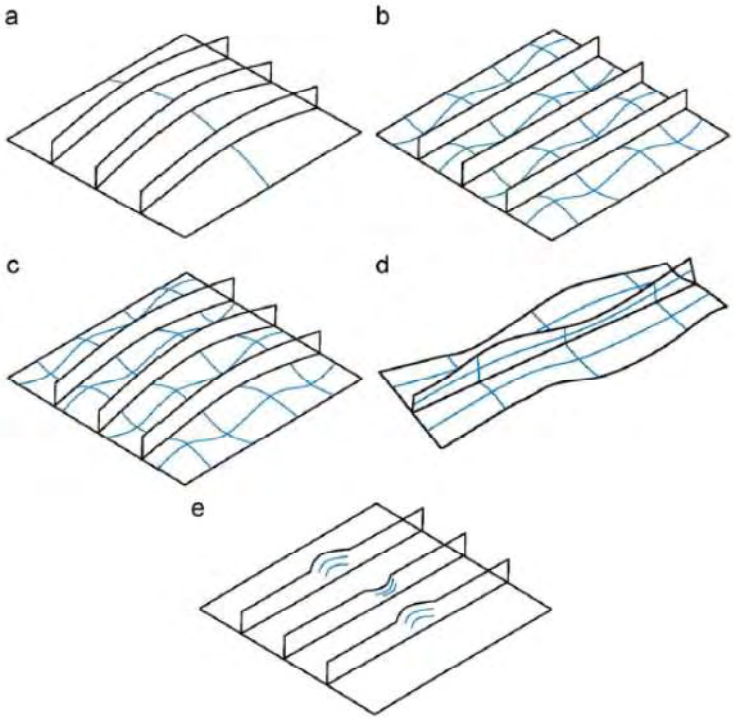

Figure 2.2 Different buckling modes of stiffened panels. Stamatelos et al. (2011)

Institutional Repository - Library & Information Centre - University of Thessaly
20/05/2024 20:20:43 EEST - 3.139.81.117

As Stamatelos et al. (2011) describes, Figure 2.2(a) depicts the global buckling of the panel, (b) the local buckling of the shell,(c) the beam-column type, (d) local buckling of the stiffener web and (e) the lateral torsional(tripping) buckling of the stiffeners which is usually followed by global buckling. Because global buckling is usually more sudden while local buckling allows the redistribution of the loads most steel, thus ductile, stiffened panels are designed so that local buckling occurs prior to global failure (Amdahl (2009); Stamatelos et al. (2011)). During the post-buckling phase, as Amdahl (2009) mentions, the boundary conditions are very important and significant interaction may occur between the stiffeners and the shell. While relatively weak stiffeners will tend to follow the deformation of the shell, strong stiffeners can provide significant increase of the load capacity during the post-buckling phase by redistribution of the loads.

As mentioned above, the boundary conditions that apply at the edges of the panel and each shell element have a significant influence on the buckling and post-buckling behavior of the structure. These boundary conditions depend on the position of the shell under study in the structure. Amdahl (2009) in Figure 2.3 demonstrates the influence of the position of the shell in the panel.

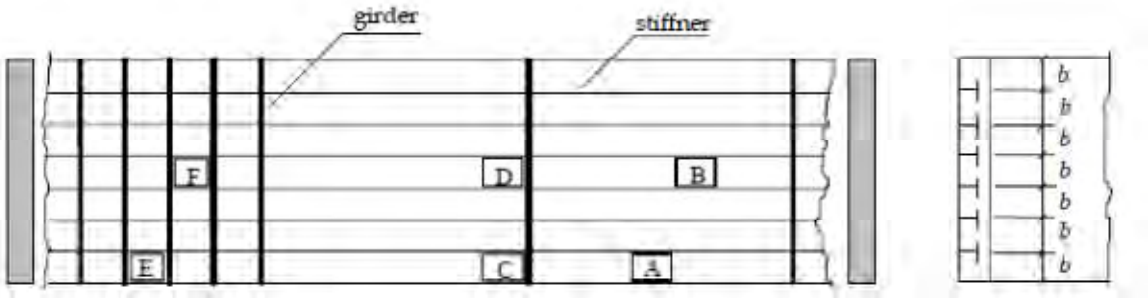

Figure 2.3 Boundary conditions of shells according to their position in the panel. Amdahl (2009)

As Amdahl (2009) notes, shell F due to its aspect ratio may be considered restrained on the grounds that the small spacing of the transverse stiffeners (or girders) does not allow transverse displacement and edges remain undistorted. Shell B, on the other hand, can be considered constrained which means that transverse displacement are allowed but the edges must remain straight. Finally, the edges of shell A are completely free. It is quite obvious that in many cases the boundary conditions are difficult to be determined. While the loaded edges are usually considered simply supported, the unloaded ones can be either considered pinned or rigidly connected to the remaining panel, which is a rather idealized approach, or elastically restrained.

Another important parameter in the behavior of stiffened shells that may cause a reduction in ultimate load-capacity is the initial imperfection of the shell. Significant interaction between the modes may occur and thus stiffened shells are considered very “imperfection sensitive”. Out of mode initial imperfections may even lead to an increase in the ultimate strength as shown in Figure 2.4 Amdahl (2009). As a result, the strength of perfect shells, easily calculated by analytical methods, can and should be used as an important reference, however the analyses that take into account the geometrical and material nonlinearities taking into account the possible shape imperfections have to be performed by the use of effective methods such as the FEM (Ueda et al. (1995)).

Institutional Repository - Library & Information Centre - University of Thessaly
20/05/2024 20:20:43 EEST - 3.139.81.117

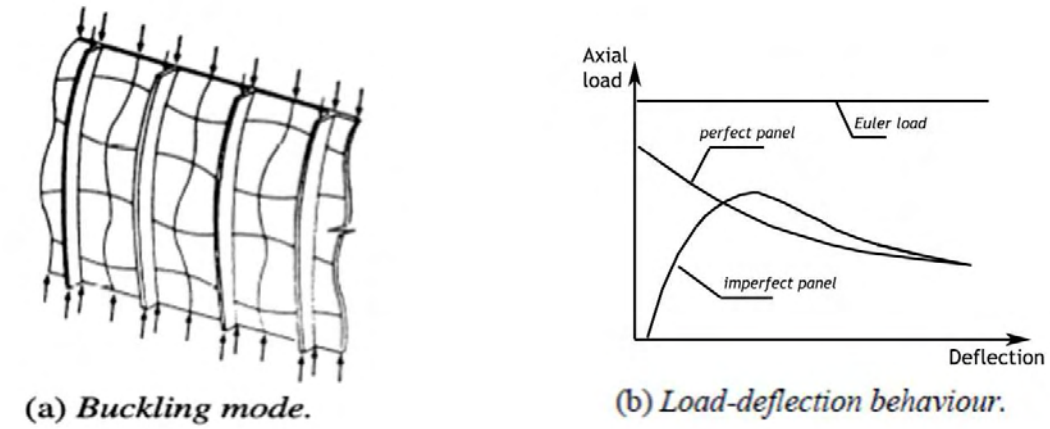

Figure 2.4 Local Buckling and Imperfection Sensitivity. Amdahl (2009)

When a stiffened shell is subjected in a combined biaxial in-plane load condition its behavior differs depending on its geometry and combination of applied loads (Ueda et al. (1995)). The behavior of the panel in each direction, as mentioned above, is controlled by the boundary conditions and the relative stiffness ratio of the stiffeners to the shell referred as $\gamma = EI/bD$ where E stands for the modulus of elasticity, I the moment of inertia of the stiffeners b the spacing of the stiffeners and D the bending stiffness of the shell. Depending on these factors the panel will either buckle in a global-overall mode or in a local one. When the structure is compressed in both directions it will again buckle in one of the two modes also depending upon the ratio of the compressive loads in each direction σ_χ / σ_y. Ueda et al (1995) based on analytical solutions expressed the following equation for the buckling interaction of a shell in the case in which both σ_x and σ_y are compressive.

$$\left[\frac{N_x / N_{xcr}}{1-\left(V_{xy} / V_{xycr}\right)^2}\right]^{e1} + \left[\frac{N_y / N_{ycr}}{1-\left(V_{xy} / V_{xycr}\right)^2}\right]^{e2} = 1 \qquad (2.2.1)$$

where $e1$ and $e2$ are given as follows

for $1/\sqrt{2} \le \beta \le \sqrt{2}$ $\quad e1 = e2 = 1$

for $\beta > \sqrt{2}$ $\quad e1 = 0.0293\beta^3 - 0.3364\beta^2 + 1.5854\beta - 1.0596$

$e2 = 0.0049\beta^3 - 0.1183\beta^2 + 0.6153\beta - 0.85$

N_{xcr} is the buckling load along the x axis

N_{ycr} is the buckling load along the y axis

V_{xycr} is the buckling shearing load

$\beta = a/b$

a is the length of the shell

b is the width of the shell

The above equation also applies to stiffened shells by assuming an orthotropic shell for overall buckling.

Institutional Repository - Library & Information Centre - University of Thessaly
20/05/2024 20:20:43 EEST - 3.139.81.117

2.3 The Structure under Investigation

2.3.1 Geometry of the Structure

The structure under investigation is a stiffened in both directions shell, under in plane loads. The structure consists of a repeating 5x5m unit, whose geometry is shown in Figure 2.5. It consists of a ferrocement skin of small thickness, stiffened in both directions by a grid of ribs. In the *x* direction the spacing of the 250mm deep ribs (ribs-*x*) is 2500mm while parallel to the *y* axis there is a 200mm deep rib (rib-*y*) every 625mm. Both ribs-*x* and ribs-*y* are 45mm thick. The out-of-plane displacement (u_z) of the stiffened shell is restrained by lines of point supports in a pattern shown in Fig. 3. The distance between point supports in each line of support is 5 meters while a line of support exists every 2.5m. The materials used in the structure at hand are cement mortar C60 and reinforcing mesh of grade B500c. Due to the small thickness of the structure, the buckling response governs the structural behavior. In addition to the geometrical nonlinearities, material nonlinearities are expected to have a great effect on the overall resistance of the structure, as is the case with all reinforced concrete structures. Due to the lack of detailed analysis and design recommendations in the Eurocode parts related to the design of concrete or cementitious structures (Eurocode 2 (2005)), methodologies followed in the design of steel structures are applied here (Eurocode 3 (2007)). The structure is studied following the fully numerical calculation procedure named by EC3 as "Design by global numerical analysis using GMNIA analysis" (GMNIA: Geometrical and Material Nonlinear analysis of the Imperfect shell).

In order to investigate the effect of the thickness of the shell on the ultimate buckling load, two cases were studied. One with subpanel-shell thickness of 20mm and one with 35mm. The loading conditions investigated were axial compression in each direction separately as well as simultaneous axial compression in both directions. Finally, the impact of the imperfections is studied by implementing initial imperfection of varying magnitude in the geometry of the shell.

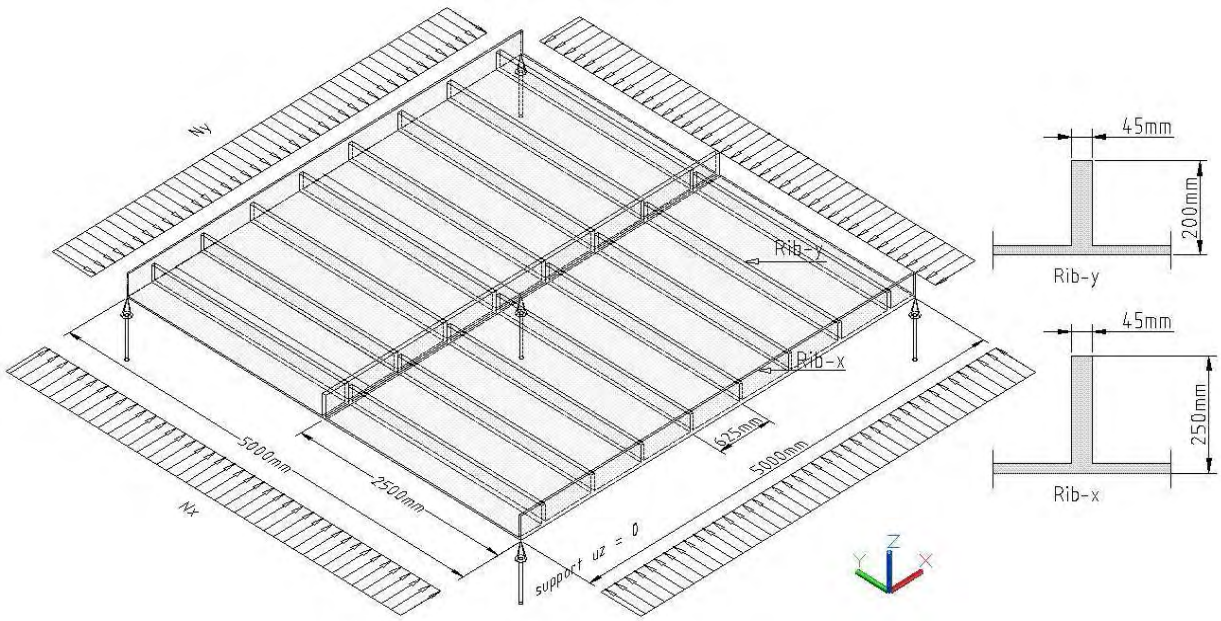

Figure 2.5 The Geometry of the repeating 5x5m Unit.

Institutional Repository - Library & Information Centre - University of Thessaly
20/05/2024 20:20:43 EEST - 3.139.81.117

As far as the reinforcement is concerned, in the case of the 20mm thick subpanel shell, it consists of three types of mesh (# Ø0.8/6.25mm, # Ø1.6/12.5mm and # Ø2.5/25mm) and two types of rods (Ø8 and Ø12). Figure 2.6 shows the different reinforcing patterns for the grid of ribs. The reinforcement ratio is about 5% in each direction. As mentioned before, although very similar to common reinforced concrete, this high reinforcement ratio, the small diameter of the rods and their distribution is expected to differentiate the behavior of the material, bringing it closer to the ductile and homogeneous behavior of steel.

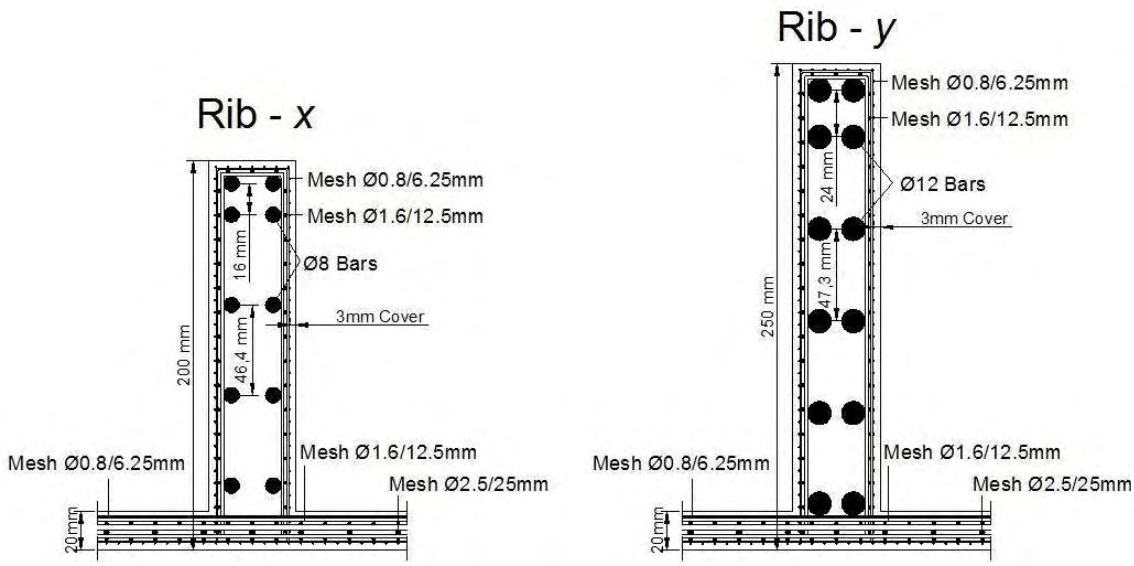

Figure 2.6 Reinforcing patterns for the grid of ribs and the 20mm thick shell.

2.3.2 Material Properties and Simulation

The stiffened shell mentioned above was considered to be constructed by C60 grade cementitious mortar and B500c reinforcing steel. As mentioned in chapter 2.1 the same regulations and standards that apply to common reinforced concrete also apply to ferrocement. Thus the material properties were based on the European norm for reinforced concrete Eurocode 2 (2005). Table 2.3 and Table 2.4 present the mechanical properties of the used materials, while Figure 2.7 and Figure 2.8 their constitutive laws. For the linear analyses all elements were considered to be made of a homogeneous isotropic elastic material with a Young's modulus of 34000 N/mm^2 and a Poisson's ratio of 0.1. For the nonlinear analyses, reinforcing steel was considered to be anisotropic, with stiffness only in the direction of the reinforcement rods, equal to 200000 MPa. Its elastic-plastic constitutive law was considered bilinear with a yield stress of 435 MPa and no hardening (Fig. 8a). As far as the cementitious mortar is concerned, it was considered isotropic, while cracking was taken under consideration by enabling the damage effect capabilities of MSC Marc with a softening modulus equal to 34000 MPa (Fig. 8b). The Tresca yield stress criterion was used.

Institutional Repository - Library & Information Centre - University of Thessaly
20/05/2024 20:20:43 EEST - 3.139.81.117

Cement Mortar

Cement mortar C60		
		Reference
Material Partial Safety Factor γ_c	1.5	EN-1992-1-1 Table 2.1N
Material Partial Factor on the Elastic Modulus γ_{cE}	1.2	EN-1992-1-1 5.8.6(3)
Characteristic Compression Strength f_{ck}	60 MPa	
Mean Value of concrete cylinder compressive strength $f_{cm}= f_{ck} + 8$	68 MPa	EN-1992-1-1 Table 3.1
Design Compression strength $f_{cd}= f_{ck}/\gamma_c$	40 MPa	EN-1992-1-1 3.1.6 (1)
Design tension strength $f_{ctd}= f_{ctk}/\gamma_c$	2.0 MPa	EN-1992-1-1 3.1.6 (2)
Young Modulus E_c	34000 MPa See note	EN-1992-1-1 Table 3.1 EN-1992-1-1 5.8.6

Table 2.3 Properties of the cement mortar.

Note: The Young modulus for non-linear analysis is divided by γ_{cE}

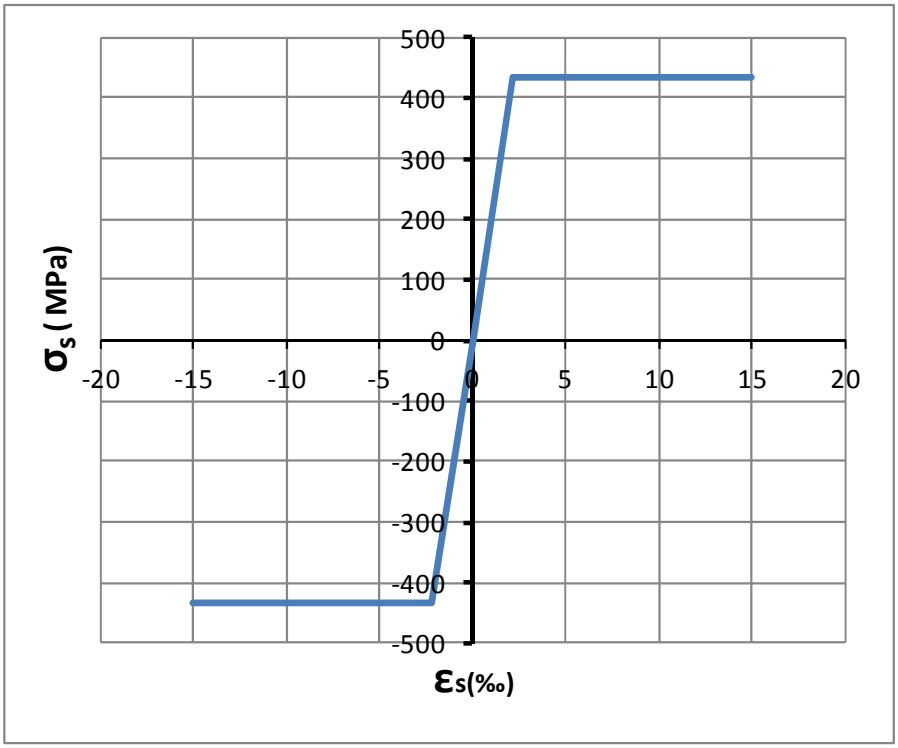

Figure 2.7 Material law for the matrix.

Institutional Repository - Library & Information Centre - University of Thessaly
20/05/2024 20:20:43 EEST - 3.139.81.117

Reinforcing Mesh

Steel B500c		
		Reference
Material Partial Safety Factor γ_s	1.15	EN-1992-1-1Table 2.1N
Young Modulus E_r	200000 MPa	EN-1992-1-13.2.7 (4)
Yield Stress f_{yk}	500 MPa	EN-1992-1-13.2.2 (3)
Design Steel Stress $f_{yd}=f_{yk}/\gamma_s$	435 MPa	
Design Yield Strain f_{cd}/E_s	0.002174	
Mesh Efficiency Factor η	0.5	Same reinforcement in both directions

Table 2.4 Properties for the reinforcing mesh.

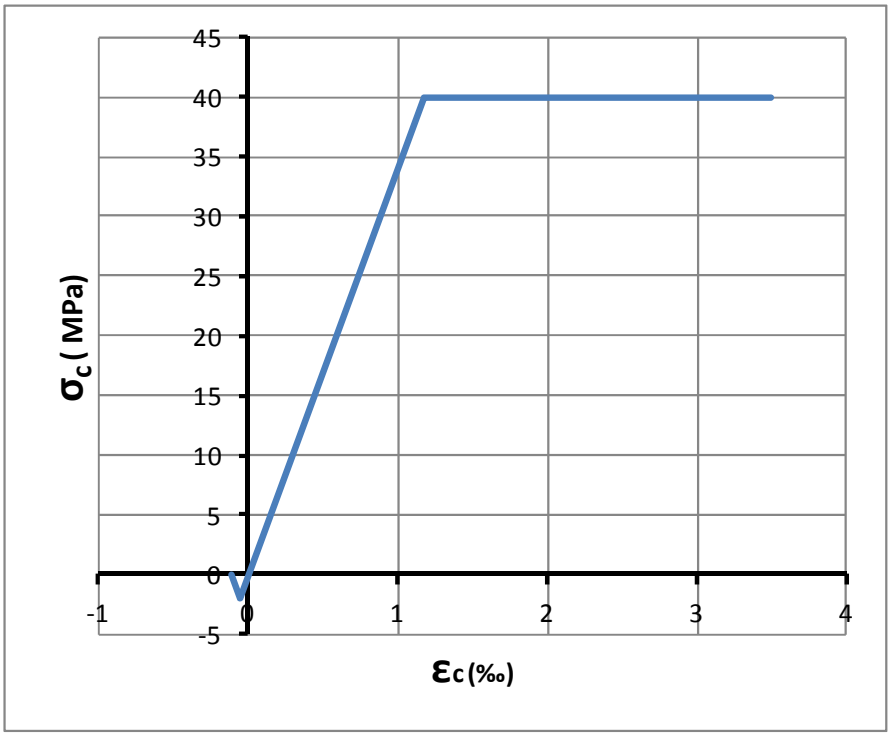

Figure 2.8 Material law for the reinforcing steel.

Institutional Repository - Library & Information Centre - University of Thessaly
20/05/2024 20:20:43 EEST - 3.139.81.117

3 Modal Buckle Analysis

3.1 Scope

For the elastic buckle analysis of stiffened shells many methods exist, analytical, semi-analytical and numerical. Given the complexity of the problem especially when plasticity is taken into consideration a numerical FE approach is used. The scope of this set of analyses was to determine the fundamental buckle eigenmodes of the ribbed skin in each direction and investigate how they are affected by the thickness of the skin. Moreover, the interaction between the axial loads in the *x* and *y* directions is of interest. In the sequel, the buckling modes, appropriately scaled, will be used in the nonlinear analysis as initial imperfections of the structure and the boundary conditions that will be applied in a reduced 5x5m area of the ribbed skin (symmetric or antisymmetric), will be determined. It is common practice in this type of studies to use periodical boundary conditions in order to reduced the modeled area and study the buckling and post buckling behavior of continuous stiffened shells and shells (Khedmati et al (2009); Mittelstedt (2007);(2009); Fujikubo et al(2006); Byklum et al (2004); Paik and Seo (2009)). The investigation of the interaction between the two axial loads (*Nx* and *Ny*) is a first approach towards understanding the behavior of the ferrocement skin under complex loading conditions.

Three simulation techniques were used. The first one utilized 4-node thick shell elements for both the shell and the grid of ribs. The second model simulated the stiffened shell by the use of 8-node solid elements in order to simulate the bending of the plate more efficiently. Finally the third one was a hybrid model, in which the grid of ribs was simulated by the use of 2-node Timoshenko beam elements and the skin by 4-node thick shell elements

The models were solved by an iterative full Newton-Raphson procedure and the convergence criterion was based on residual forces. The inverse power sweep method was used for the buckle solution.

3.2 Material Properties for the Analysis

For the modal analysis of the ribbed skin all elements were consider to be made of a homogeneous isotropic elastic material with a Young's modulus of 34000 N/mm^2 (E_c/γ_{cE} = 40800/1.2) based on the properties of the cement mortar and a Poisson's ratio of 0.1 due to the fact that the bi-directional mesh and the grid of ribs and shells reduce the extensions in orthogonal directions.

3.3 Modeling by the Use of Shell Elements

First, in order to reduce the computational time needed for the analysis, and based on the fact that the structure actually consists of a repeating 5 x 5 ribbed skin area, an area of 25 m x 27.5 m is simulated. Both the skin and the grid of ribs were modeled by the use of shell elements. The shell elements representing the skin were 156.25 x 156.25 mm and have a thickness of 20 or 35 mm depending on the case under study while the ones representing the ribs 45mm. The element type 75 is used for all shells (see Appendix A for more information on element type technology used in MSC Marc).

In order to obtain an equivalent load of 1 kN per meter of stiffened shell without eccentrity, the load is applied as an edge pressure load both on the skin and the ribs with its value depending on the thickness of the shell element according to the following calculations.

Institutional Repository - Library & Information Centre - University of Thessaly
20/05/2024 20:20:43 EEST - 3.139.81.117

$F_i = \sigma * t_i$, with *i* either sl or p depending on whether it is applied on a stiffener or the plate

t_i the thickness of the shell element

σ pressure in the loaded direction

$\sigma = 1\ kN / A_{tot}$

$A_{tot} = A_{sl} + A_p$

A_{tot} total area in the loaded direction per meter of ribbed skin

A_{sl} total area of the longitudinal stiffeners per meter of ribbed skin

A_p total area of the plate per meter of ribbed skin

	Direction	A_{sl} (mm)	A_p (mm)	A_{tot} (mm)	σ (N/mm^2)	F_{sl} (N/mm)	F_p (N/mm)
20mm thick shell	x	4320	20000	24320	0.0411	1.850	0.822
	y	13680	20000	33680	0.0297	1.336	0.594
35mm thick shell	x	4185	35000	39185	0.0255	1.148	0.893
	y	13140	35000	48140	0.0208	0.935	0.727

* In some cases the external ribs-*x* were loaded with half the load because only half the section belongs to the simulated and/or loaded area. (0.925 N/mm or 0.574 N/mm)

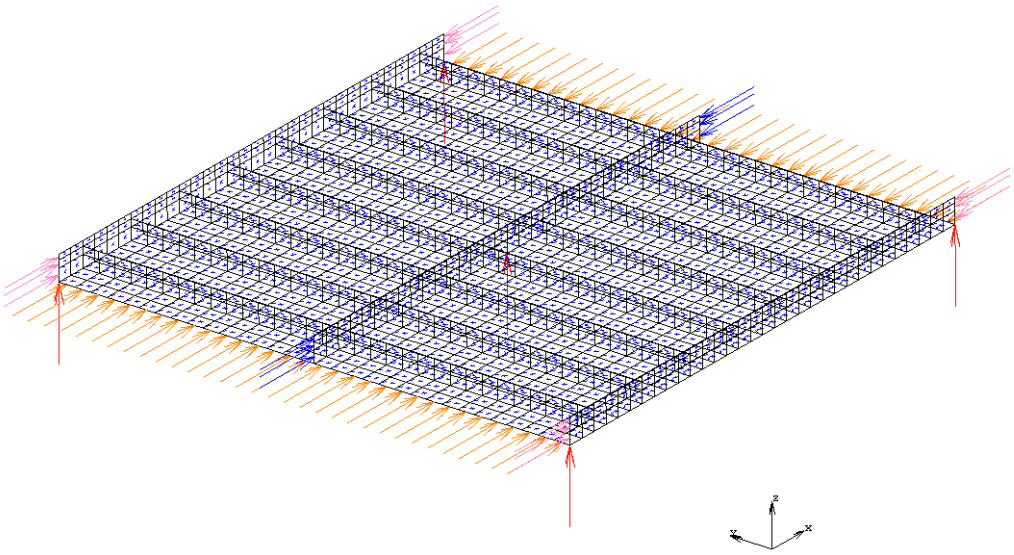

Figure 3.1 Load application and out of plane restrains of the repeating 5x5m unit in the x direction.

Institutional Repository - Library & Information Centre - University of Thessaly
20/05/2024 20:20:43 EEST - 3.139.81.117

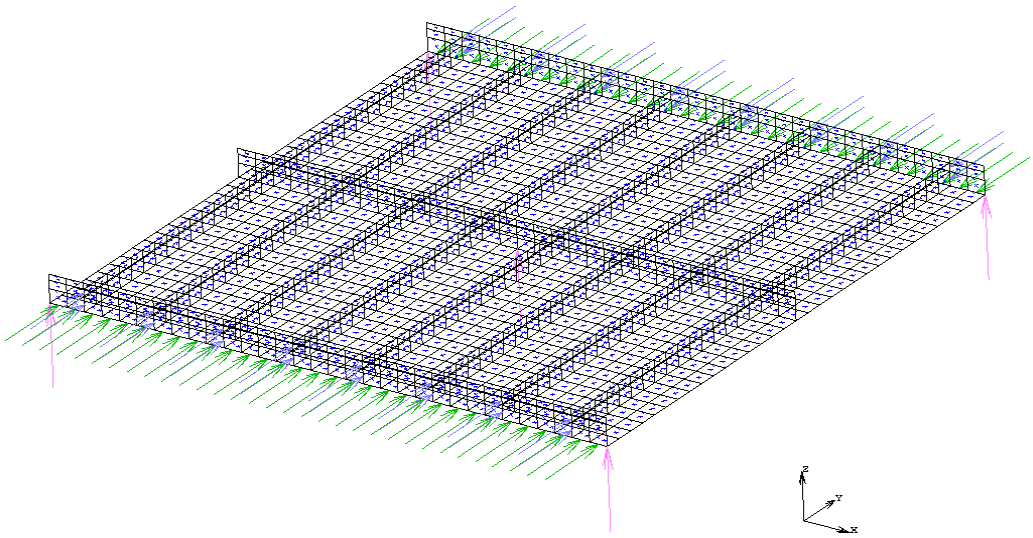

Figure 3.2 Load application and out of plane restrains of the repeating 5x5m unit in the *y* direction.

3.3.1 20mm Thick Skin Modal Buckle Analysis

3.3.1.1 Analysis of the 25x27.5m models

The complexity of the geometry and support conditions of the structure cause the boundary conditions that apply on the outer edges of this reduced 25 x 27.5m area not to be clear from the beginning. Thus, a preliminary analysis was carried out in order to determine the predominant buckle modes in both directions. The only restrains of the structures were the out of plane supports (the deflection equals to zero) and the central 5x5 m area was loaded with a compressive axial load. The outer spans simulate the continuity of the ribbed skin in both directions without imposing any additional boundary conditions that may lead the model to buckle in a certain way which may not be the critical. In order to prevent a rigid body movement in the *x-y* plane the displacement along the *x* axis of two nodes in the *y-z* plane of symmetry and the displacement along the *y* axis in the *x-z* plane of symmetry was restrained (Figure 3.3). In the sequel, the loaded region was increased to 15x15 m so that the supporting effect of the not loaded outer spans is reduced.

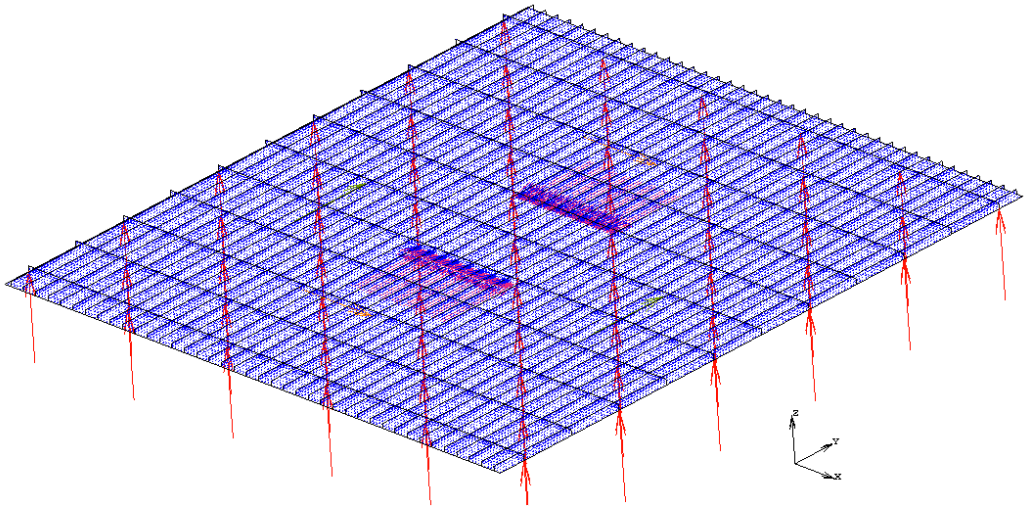

Figure 3.3 The 25 x 27.5 m model with the central loaded area and out of plane restrains.

Institutional Repository - Library & Information Centre - University of Thessaly
20/05/2024 20:20:43 EEST - 3.139.81.117

3.3.1.1.1 Results for a 5x5 m loaded region

When the central 5x5m region was subjected to compressive loading parallel to the *x* axis the stiffened shell buckled locally due to the slenderness of the shell, the low aspect ratio of the subpanels and torsional flexibility of the transverse stiffeners. The critical buckle eigenmode according to MSC Marc 2011 is shown in Figure 3.4. The effective length (or half-wave length) is 625mm and the buckling load is 2307 N/mm. It should be noted that the axial load capacity of the cross section is A_c*f_{cd} = 24320*40/1000 = 972.8 N/mm which is lower than the N_{cr}, but the actual inelastic buckling load is expected to be much lower than the elastic one due to the initial imperfections and great non-linear behavior of the section. Also, as mentioned before, this set of analysis is carried out in order to determine the buckling shape rather than determine the critical buckling load .

Parallel to the *y* axis the buckling mode changed to the global one. This is caused by the presence of a stiffener every 625mm. The buckle shape was chessboard like and had an effective buckle length (or half-wave length) of about 5m (Figure 3.5). The "imperfect" shape of the mode is caused by the stiffness provided by the outer spans, which act as springs. This is somehow similar to the expected buckling behavior of a five span continuous beam with only the two central spans loaded.

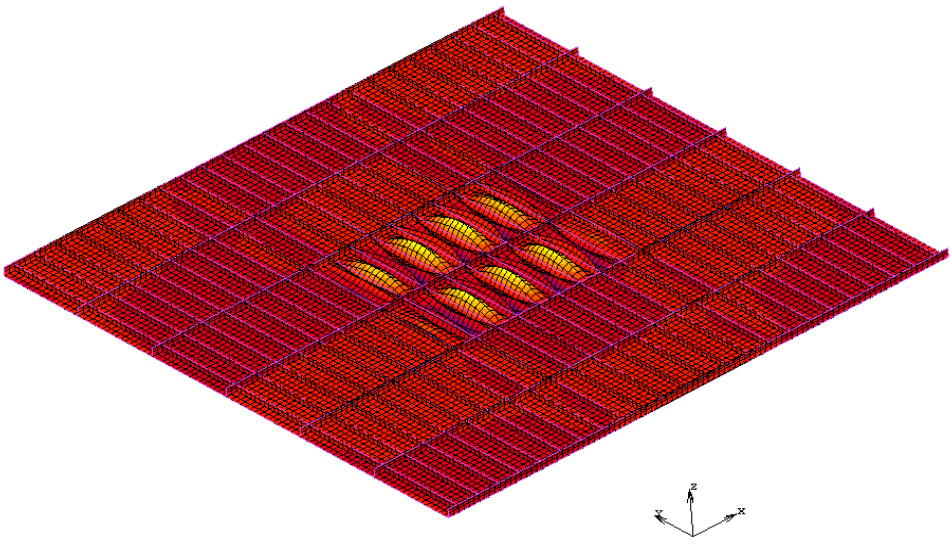

Figure 3.4 First buckle eigenmode along the *x* axis.

Institutional Repository - Library & Information Centre - University of Thessaly
20/05/2024 20:20:43 EEST - 3.139.81.117

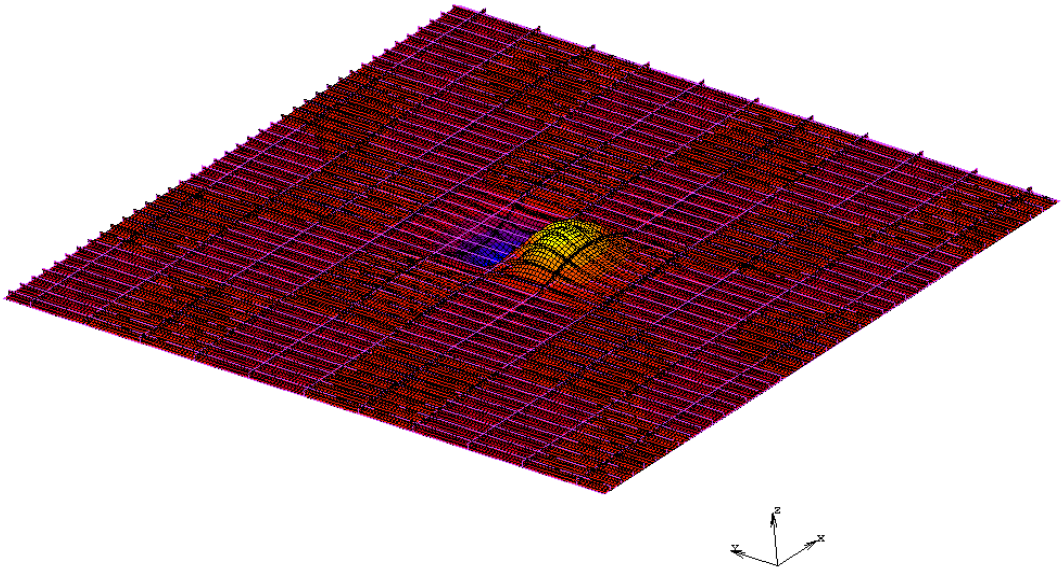

Figure 3.5 First buckle eigenmode along the *y* axis.

Next, in order to further examine the buckling behavior of the structure, a broader region (15m x 15m) was loaded. As mentioned before, this will reduce the supporting effect of the outer spans and is expected to lead to a reduction of the buckling load and a more perfect buckling shape. The results are presented in the following pages.

3.3.1.1.2 Results for a 15 x 15m Loaded Region

Even with a broader loaded region and only one span providing rotational support to the inner loaded region the skin buckles again between the transverse stiffeners (ribs – *y)* (l_b = 625 mm) along the *x* axis. The first 60 eigenmodes correspond to local buckling between ribs, with loads ranging from 1617 to 2555 N/mm. This is indicative of the high sensitivity of the local buckling to variations of the buckling shape and ultimate buckling resistance. Figure 3.6 shows the first of these buckle eigenmodes. This buckle mode corresponds to a local buckling with decreasing maximum deflections from the outer loaded edge to the center.

Parallel to the *y* axis the chessboard buckling shape becomes clearer as the loaded region is broadened. Figure 3.8 shows the shape of the central 5x5m region. It is obvious that the buckling length of the structure is the span between the supports (5m)

The results of this set of analysis were considered to be more representative over the ones of the 5x5m loaded region on the grounds that this study focuses on the simultaneous buckling of the whole structure (even if the magnitude of deformation may not be equal between all half-waves) and thus the supporting effect of unloaded spans that do not buckle needs to be eliminated.

Institutional Repository - Library & Information Centre - University of Thessaly
20/05/2024 20:20:43 EEST - 3.139.81.117

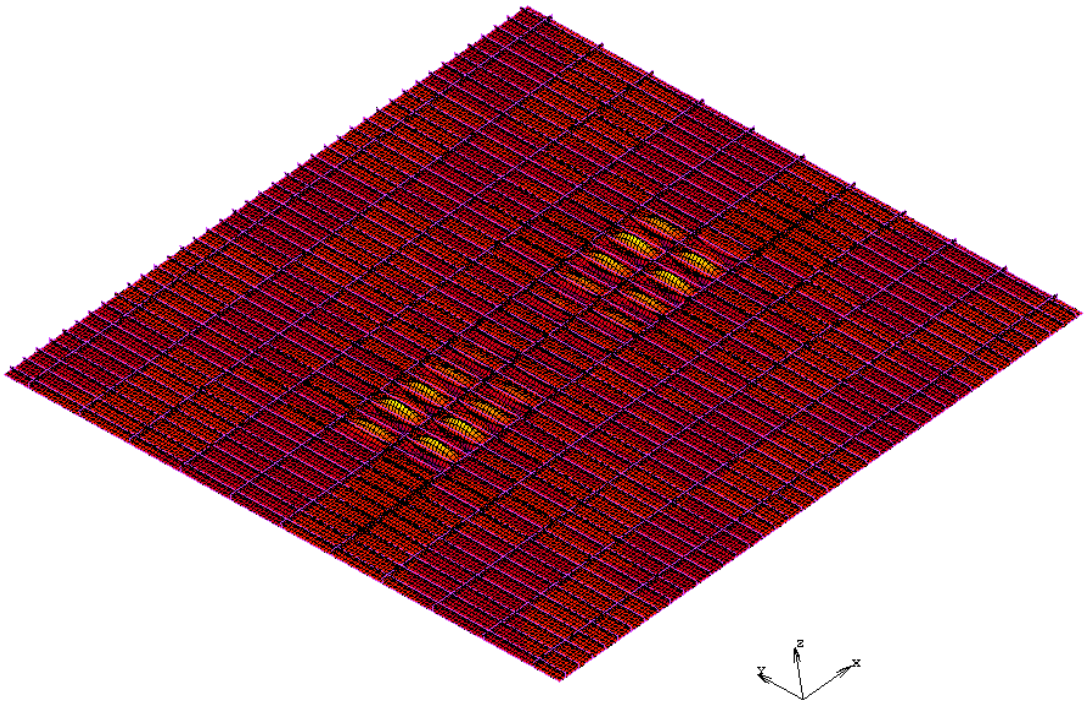

Figure 3.6 First buckle eigenmode along the *x* axis.

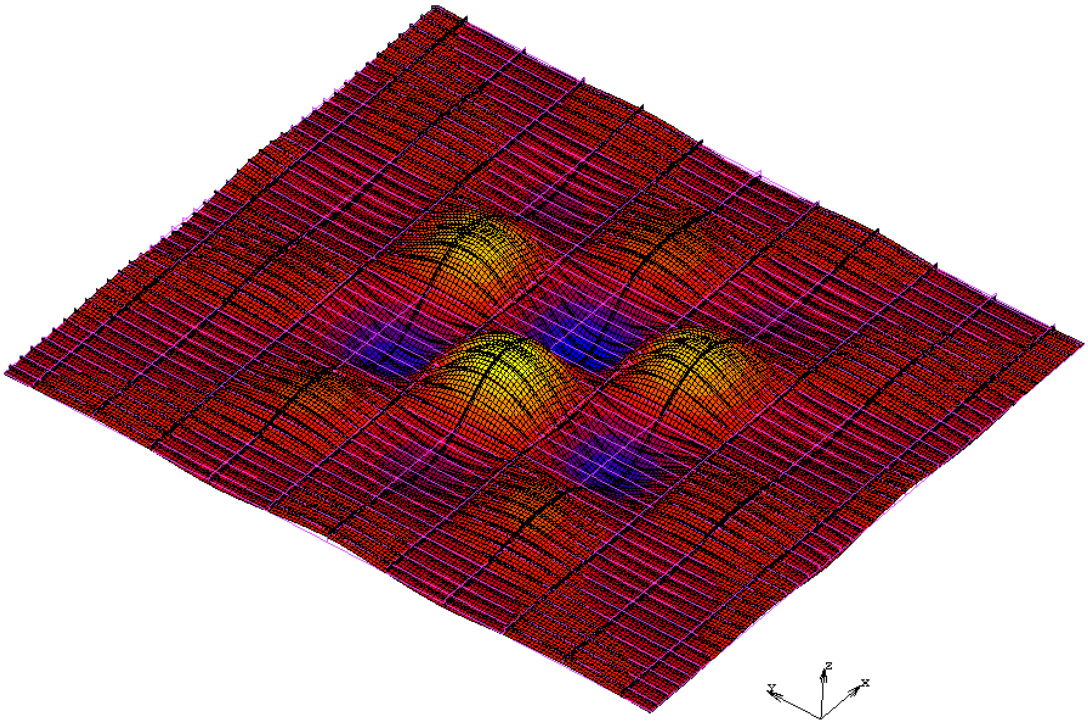

Figure 3.7 Buckling along the *y* axis.

Institutional Repository - Library & Information Centre - University of Thessaly
20/05/2024 20:20:43 EEST - 3.139.81.117

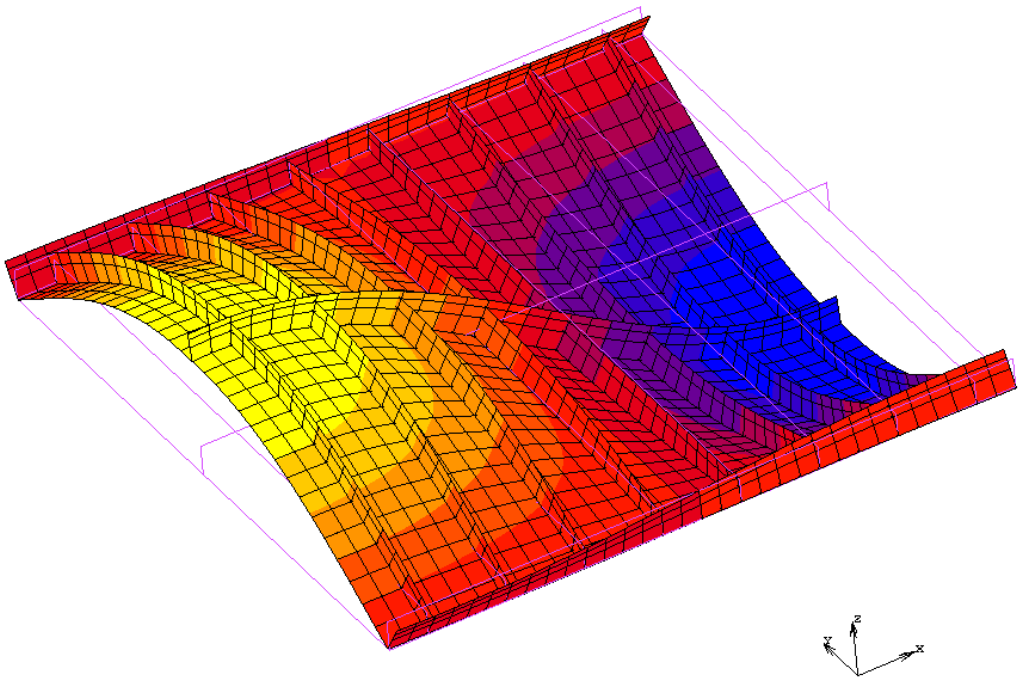

Figure 3.8 Buckling along the *y* axis. Deformed shape of the central 5x5 region

3.3.1.2 Discussion of the results of the 25x27.5m model

The results of the above modal analysis indicate that the 20mm thick ribbed shell tends to buckle along the *x* axis locally between the ribs and along the y axis between supports. The buckle shape along the *x* axis is typical for such structures and many studies use similar or identical shape functions for the investigation of local buckling of the subpanels (Fukikubo et al. (2006); Mittelstedt (2007); Mittelstedt (2009); Paik et al. (2008); Paik and Seo (2009)).

Based on the buckle shapes that the modal analyses predict, the boundary conditions that apply on the basic 5x5 m unit of which the entire structure consists can be determined. Figure 3.9 and Figure 3.10 show boundary conditions that correspond to the buckle shape along the *y* and *x* axis respectively. These boundary conditions are compatible as shown in Figure 3.11, meaning that they cause the same periodic boundary conditions at the edges of the repeating 5x5 m unit and thus any *n**5 x *m**5 model (*n,m* integers) will have boundary condition of symmetry along the y edges and antisymmetry along the x edges.

Next, in order to further verify the results of the aforementioned set of analysis and at the same time reduce the computational time required for the analysis of the structure, a 15 x 15 m model was formulated.

Institutional Repository - Library & Information Centre - University of Thessaly
20/05/2024 20:20:43 EEST - 3.139.81.117

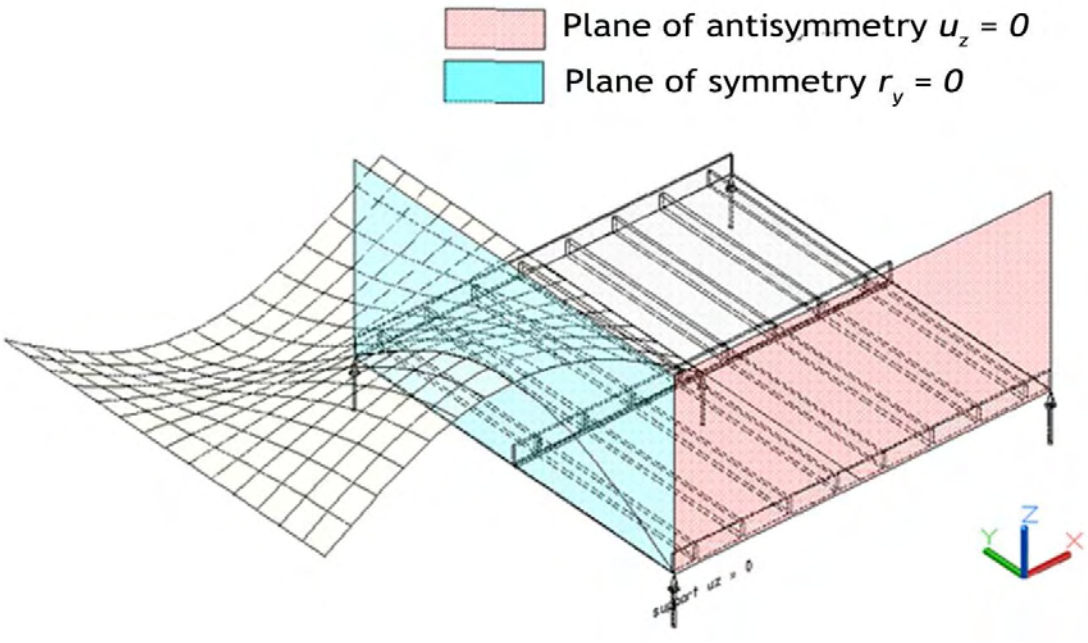

Figure 3.9 Buckle shape and boundary conditions of the central region for the buckling along the *y* axis.

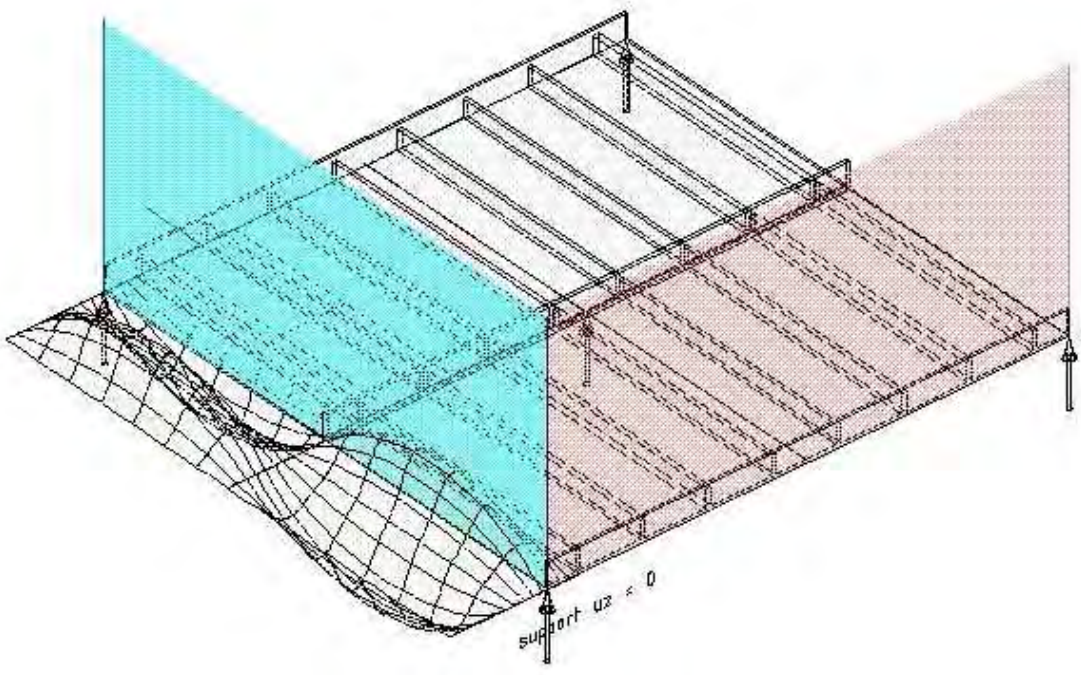

Figure 3.10 Buckle shape and boundary conditions of the central region for the buckling along the *x* axis.

Institutional Repository - Library & Information Centre - University of Thessaly
20/05/2024 20:20:43 EEST - 3.139.81.117

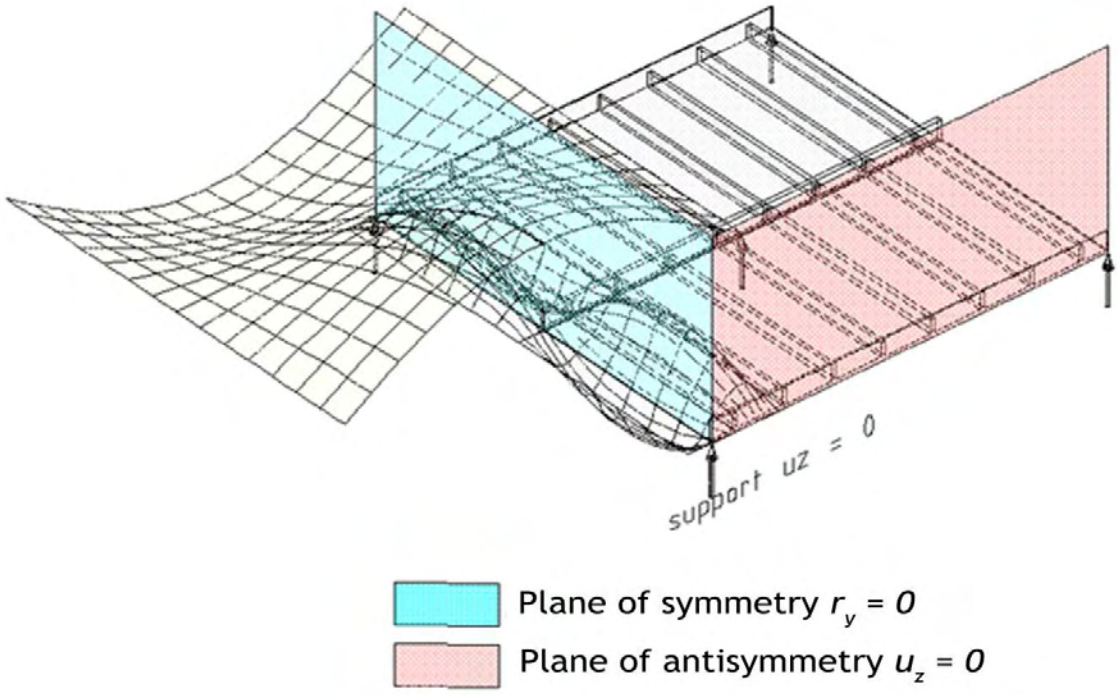

Figure 3.11 Summary of the buckle shapes and boundary conditions of the central 5x5m region

3.3.1.3 Analysis of the 15x15m model

The boundary conditions discussed above (Figure 3.11) are applied at the *x* and *y* outer edges of the model and the ribbed skin was compressed with and axial load of 1 kN/m of ribbed skin, in such a way that no load eccentricity arises. The displacement along the *z* axis was restrained along the nodes of both edges parallel to the *x* axis as well as the rotation around the *y* axis for all nodes along the y edges. In addition, a RBE2 link between the nodes of the cross section parallel to the y axis was created so that all nodes have the same *x* displacement, since the rotation of the cross section equals to zero and the cross section remains plane and normal to the deformed axis (see Appendix A for an explanation of RBE2 links). Figure 3.12 shows all the boundary conditions and constrains applied to the model. The entire model was loaded as the boundary conditions simulate the continuity of the shell and loading only a reduced central area will produce results similar to that of the 25x27.5 m models. The buckle loads correspond to simultaneous buckling of all spans, in contrast to the ones of the 25x27.5m model, which are less conservative on the grounds that unbuckled spans exist in the model.

Institutional Repository - Library & Information Centre - University of Thessaly
20/05/2024 20:20:43 EEST - 3.139.81.117

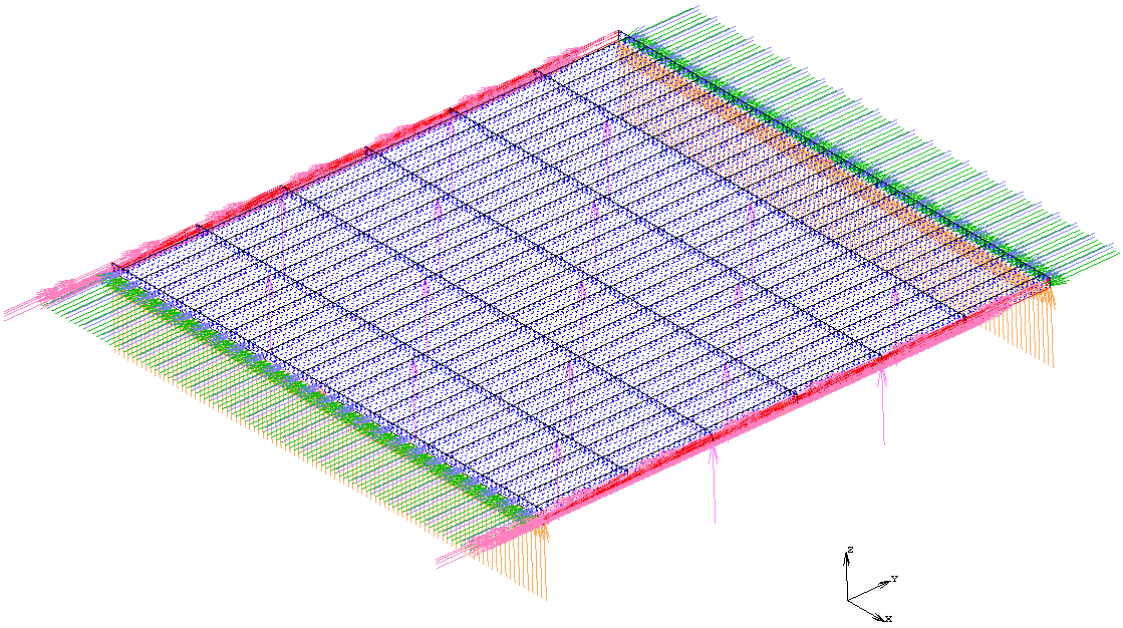

Figure 3.12 Loads and boundary conditions of the 15x15 m model.

3.3.1.4 Results and discussion for the 15x15 m model

The structure buckles in both directions as expected (Figure 3.13 and Figure 3.14) and the critical loads are 2725 kN/m in the *y* direction and 1453 kN/m in the *x* direction respectively. As mentioned above, these loads correspond to simultaneous buckling of the entire structure. This is more obvious in the case of the buckling along the *y* axis, where all spans have equal maximum deflection. In the case of the buckling along the *x* direction, although all the subpanels buckle, the deflection has an increasing magnitude towards the outer spans. This is caused by the aforementioned sensitivity of local buckling to deviations. Local buckling appears in more than one buckling shapes with buckling loads very close to one another. A way to force the model to buckle in the desired way (equal deflection of all spans) would be to impose the periodic boundary conditions of symmetry and antisymmetry not only on the outer edges but inside the structure as well. That would mean that along the ribs-*x* and ribs-*y* conditions of antisymmetry should apply and in the middle of the span they form conditions of symmetry should be imposed. This would result in a “perfect” shape, however it would make the model unable to capture the interaction between global and local modes and the possible change from local to global buckling, on the grounds that these boundary conditions are not compatible with the global mode. In the sequel, the size of the model was further reduced to the 5 x 5 m basic repeating unit. Since the 15x15 m and the 5x5 m model are considered to be equivalent (boundary conditions on the outer edges and buckling of all spans), no major changes either on the buckling shape or on the buckling loads are expected.

Institutional Repository - Library & Information Centre - University of Thessaly
20/05/2024 20:20:43 EEST - 3.139.81.117

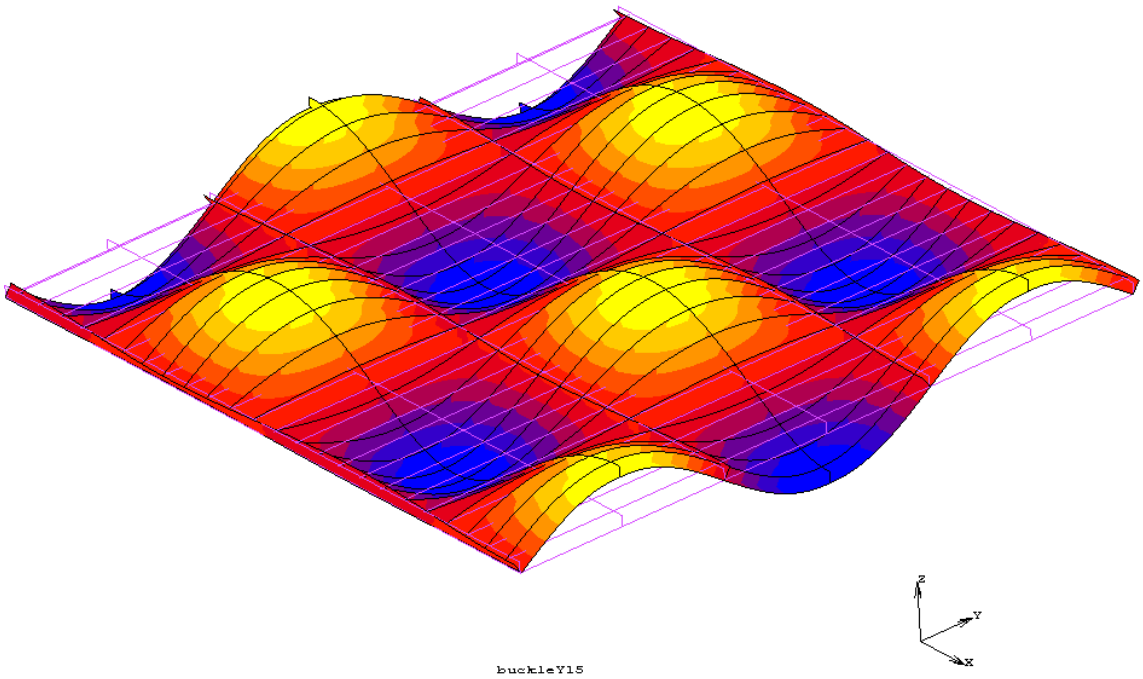

Figure 3.13 First buckle eigenmode along the *y* axis.

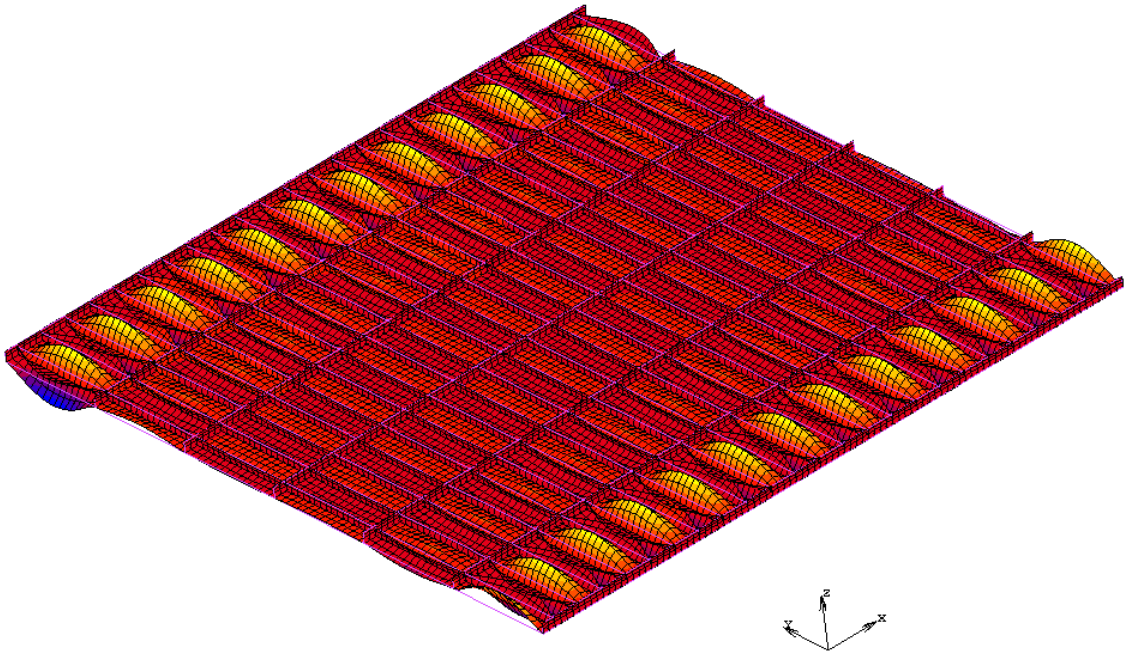

Figure 3.14 First buckle eigenmode along the *x* axis.

Institutional Repository - Library & Information Centre - University of Thessaly
20/05/2024 20:20:43 EEST - 3.139.81.117

3.3.1.5 Analysis of the 5x5 m models

As in the 15 x 15 m model the displacement along the *z* axis was restrained along the nodes of both edges parallel to the *x* axis. Moreover, no rotation around the *y* axis of the two outer cross sections parallel to the *y* was allowed. As mentioned before, the load was applied uniformly along the edges of the finite element both on the skin and on the ribs, with its value depending on the thickness of the shell element, so that no eccentricity arises. In order to investigate the mesh dependency and sensitivity of the numerical simulation, besides the model consisting of 156.25 x 156.25 mm, two more models were formulated with a finer mesh sizing. In the first one the mesh sizing was 78.125 x 78.125 mm while in the second one 39.0625x39.0625 mm. This procedure is very important for the prediction of the ultimate load capacity of stiffened shells using FE models and the relevant regulations and standards impose the verification of the adequacy of the mesh sizing by refinement of the model and calculating the deviation.

3.3.1.6 Results and discussion for the 5x5 m models

The analyses of the 5x5 m model with a square mesh sizing of 156 mm predicted a buckling load along the *x* direction of 1449 kN/m while along the *y* direction the computed buckling load was 2678 kN/m. The very small and expected deviation of the buckling load along the *x* axis was caused, as mentioned in Section 3.3.1.4, by the fact that the 15 x 15 model calculates the load according to a buckling shape that has an increasing maximum deflection towards the outer spans while in the 5x5 model the absolute maximum deflection was equal for all spans. Although the 15x15 m and the 5x5 m model are similar, as in both models the boundary conditions are imposed on the outer edges and the entire structure is loaded so no unloaded spans add undesirable false stiffness to the structure, the 5x5 m model is equivalent to a 15x15 m model with periodic boundary conditions every 5 meters. This slight change of imposed boundary conditions causes the high sensitivity of the local buckling mode and leads to a differentiation of the shape and load. The differences of the load carrying capacities is considered insignificant as it is only 0.2%, while what is of more importance is the shape of the buckling mode which will be used as the shape of the initial imperfections of the GMNIA. Keeping in mind that in global buckling the structure will tend to keep the deflection equal for all spans, the 5x5 m model is considered as more accurate.

When each shell of the 5 x 5 model skin was subdivided in 4 elements and thus the mesh grid was 78.125x78.125, the predicted elastic buckling loads where

$N_{bx} = 1287\ \text{kN/m}$

$N_{by} = 2665\ \text{kN/m}.$

A further refined model consisting of 39.0625 mm square elements results in the following buckling loads:

$N_{bx} = 1245\ \text{kN/m}$

$N_{by} = 2661\ \text{kN/m}.$

It is obvious that the buckling load along the *y* axis is not sensitive to mesh sizing, mainly because of its buckle length while the *x* buckling load is mesh dependant. On the grounds that the second refinement causes only a 3.4% decrease of the buckling load, a model with a skin consisting of 78.125x78.125 mm shell elements was considered to be accurate enough for the needs of our study.

Institutional Repository - Library & Information Centre - University of Thessaly
20/05/2024 20:20:43 EEST - 3.139.81.117

3.3.2 35mm Thick Skin Modal Buckle Analysis

3.3.2.1 Results and discussion of the 25x27.5 m models

As with the 20 mm thick model, the boundary conditions that apply on the outer edges of the model cannot be determined from the beginning. Thus, again a larger model was originally created (25 x 27.5 m) and the central 5x5m and 15x15m areas were loaded while the outer spans (not loaded) simulate the continuity of the ribbed skin in both directions without imposing any additional restrictions. The output of the analysis will provide the necessary information to define the boundary conditions of the final smaller model and the shape of the initial imperfections of the GMNIA. The edge loads of the shell and the ribs are calculated so that an equivalent load of 1 kN per meter of stiffened shell was applied to the structure with no eccentricity.

Both in the case of a 5 x 5 m loaded region and in the case a 15 x 15 loaded region the results were similar. The analyses predicted that, when loaded parallel to the *x* axis, the stiffened shell has the tendency to buckle in an almost one-dimension buckle shape, as shown in Figure 3.15, with an effective length of 2.5 m (one dimensional buckle shape) at an axial load of 3697kN/m (15 x 15 m loaded region). However, the main objective of this thesis is to study the simultaneous buckling of the entire structure and not localized failure. Thus, when the entire structure buckles simultaneously it is assumed that the shape of this buckle mode will have a sinusoidal shape in the *x* direction with constant amplitude along the *y* axis as shown in Figure 3.16. Thus, the boundary conditions of the central 5x5 area are considered again to be that of the symmetry along the *x* edges and that of the antisymetry along the *y* edges. This assumption is expected to have little influence on the accuracy of the investigation as these boundary conditions will be finally imposed on the basic repeating 5x5 m unit and at least the shape of the central region of the stiffened shell extending to infinity is expected to have an almost perfect sinusoidal shape.

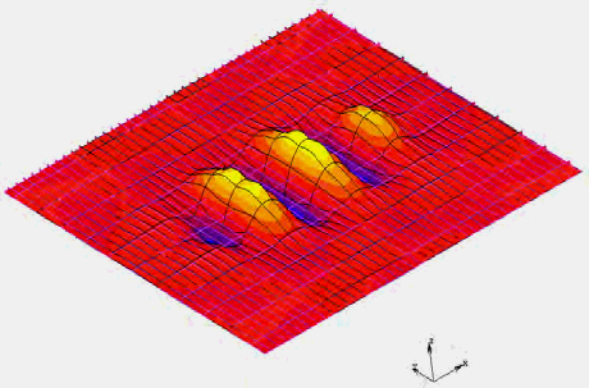

Figure 3.15 Buckling along the *x* axis. 15x15 m loaded region

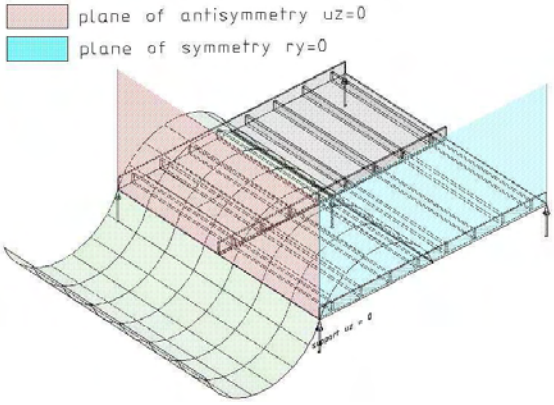

Figure 3.16 Buckle shape and boundary conditions for the buckling along the *x* axis

Parallel to the *y* axis the stiffened shell buckled globally and the same boundary conditions discussed in the 20mm thick models also apply to the 35 thick model (Figure 3.17).

Institutional Repository - Library & Information Centre - University of Thessaly
20/05/2024 20:20:43 EEST - 3.139.81.117

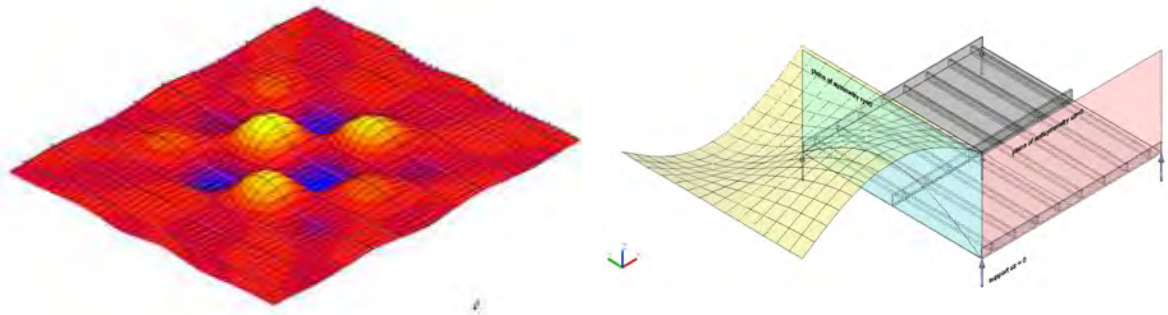

Figure 3.17 First buckle shape along the *y* axis and its boundary conditions

3.3.2.2 Results and discussion for the 15x15 m model

In order to further investigate the buckling behavior parallel to *x* axis a 15 x 15 m model was created with the boundary conditions shown in Figure 3.16. Surprisingly the structure buckled in a chessboard-like pattern exactly as in the *y* direction when the axial load equals to 2822 kN/m (Figure 3.18). The buckling load that corresponds to a one dimensional buckle shape as discussed in Figure 3.16 and shown in Figure 3.19 was 3127 kN/m. The cause of this phenomenon was mainly that in the 25 x 27.5 m model the outer not loaded spans act like as a rotational spring, adding stiffness to the structure, while in the 15x15 m model a global buckling was considered where all spans lose their stability at the same time. This phenomenon is also a strong indication of the interaction between global and local buckling modes. This interaction is greatly affected by the boundary and loading conditions of the structure. Luckily, the boundary conditions of the global buckling are interchangeable between the two axes, meaning that the same results would be produced if boundary conditions of symmetry were imposed along the *x* edges and that of the antisymmetry along the *y* edges. That made the boundary conditions of global and the local column-like buckling compatible and the model was able to capture this phenomenon. It is obvious that when the buckling behavior of such stiffened shells is investigated, special care is needed. Different boundary conditions that correspond to potentially critical buckling modes should be imposed to the model so that no buckling mode is omitted.

After these analyses, it is safe to say that the 35mm thick ribbed skin will buckle globally in both directions with a chessboard-like pattern. A buckle analysis in the y direction calculated a buckle load of 2813 kN/m. It must be noted that the buckling loads in the x and y direction should be equal. The 9 kN/m of difference is only 0.3% of the critical elastic buckling load. Again, the periodic boundary of the two buckle shapes at the edges of the repeating 5x5 m unit are the same and thus any *n**5 x *m**5 model (*n,m* integers) will have boundary conditions of symmetry along the y edges and antisymmetry along the x edges.

Institutional Repository - Library & Information Centre - University of Thessaly
20/05/2024 20:20:43 EEST - 3.139.81.117

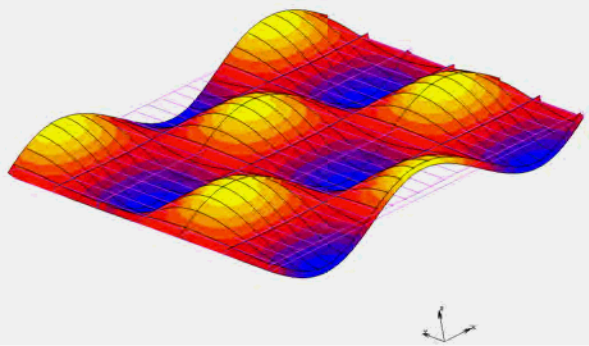

Figure 3.18 Critical global buckle eigenmode along the *x* axis.

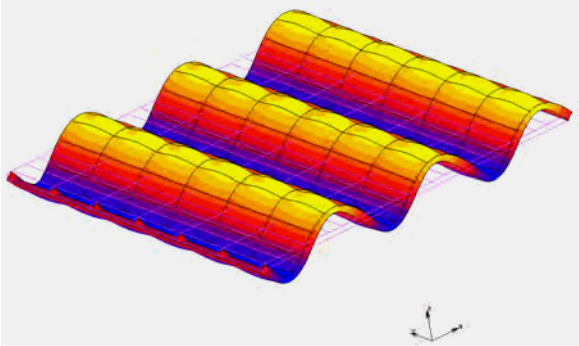

Figure 3.19 Column-like global buckle eigenmode along the *x* axis.

3.3.2.3 Results and discussion of the 5 x 5 m model

A unified 5 x 5 m model was formulated as shown in Figure 3.20 with boundary conditions of symmetry along the y edges and antisymmetry along the x edges in order to study both the x and y buckling behavior and their interaction. It was chosen not to keep the boundary conditions discussed in Figure 3.16, as the possibility of one dimensional buckling was already excluded from the study of the 15x15m model. By imposing boundary conditions of symmetry along the y edges and antisymmetry along the x edges, the global buckling is not affected while possible change of the buckling mode to the one of buckling between stiffeners can be captured. The shell buckled in both directions globally as shown in Figure 3.21 and 3.22 and the calculated loads were:

$N_{bx} = 2792\ \mathrm{kN/m}$

$N_{by} = 2785\ \mathrm{kN/m}$

The difference is about 1% between the 15x15 m and the 5x5 m model and only 0.25% between the x and y direction

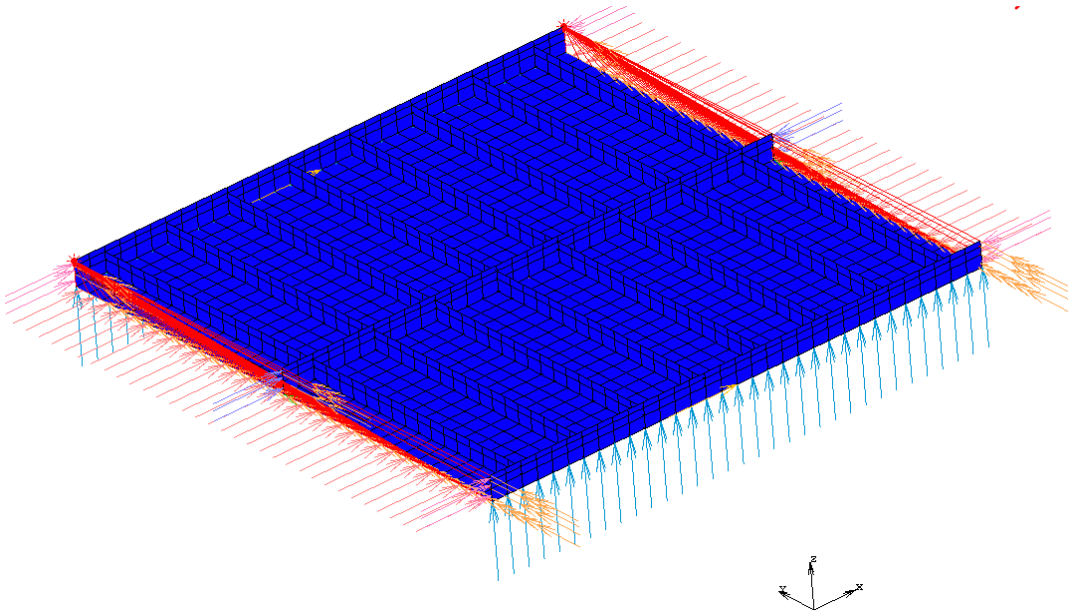

Figure 3.20 35mm thick 5x5m model

Institutional Repository - Library & Information Centre - University of Thessaly
20/05/2024 20:20:43 EEST - 3.139.81.117

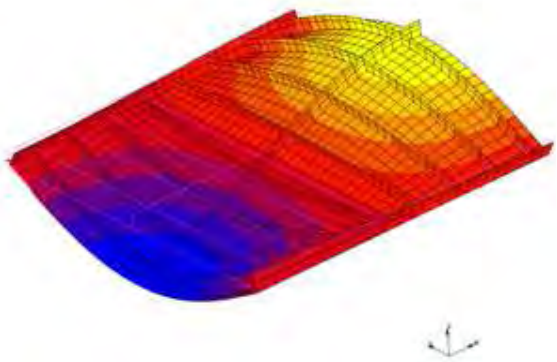

Figure 3.21 Buckle shape along the *x* axis.

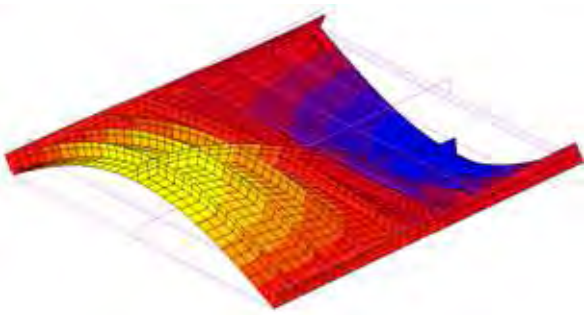

Figure 3.22 Buckle shape along the *y* axis.

As with the 20 mm thick shell, the model was refined in order to study the effect of the mesh on the buckling load. The shell elements of the skin were subdivided into four 78.125 x 78.125mm square elements and the following buckling loads were calculated

$N_{bx} = 2780\ \text{kN/m}$

$N_{by} = 2774\ \text{kN/m}$

Difference between models *x-x* = 0.4%
Difference between models *y-y* = 0.4%
Difference between the two directions = 0.2%

A further refined model consisting of 39.0625 mm square elements results in the following buckling loads:

$N_{bx} = 2776\ \text{kN/m}$

$N_{by} = 2770\ \text{kN/m}$

Difference between models x-x = 0.1%
Difference between models y-y = 0.1%
Difference between the two directions = 0.2%

As a conclusion, it can be said that even the model with a skin consisting of 156.25 mm shell elements can be considered to be accurate enough for the needs of our investigation, as global buckling is not highly mesh dependant. However, the mesh grid of the final non-linear model will be consisting of 78.125 mm elements so that the results between the 20 mm and 35 mm thick models are comparable.

Institutional Repository - Library & Information Centre - University of Thessaly
20/05/2024 20:20:43 EEST - 3.139.81.117

3.4 Modeling by the Use of Solid Elements

In order to demonstrate an alternative way of simulation of the structure, but also for verification reasons, another model consisting of 8-node solid elements was formulated. All elements are of type 7 (see Appendix A for explanation of element types) in order to simulate the bending of the shell more efficiently. Both the skin and the grid of ribs have one element in the thickness direction. The axial pressure was applied on the face of the solid elements (0.041118 N/ mm^2 load parallel to the *x* axis, 0.02969 N/ mm^2 load parallel to the y axis), again taking care to eliminate any load eccentricities. The mesh sizing of the elements consisting the subpanels was 145x153.438 mm. As the critical buckle modes had already being determined by the modal analysis of the shell model, the analysis of 25x27.5 m and 15x15 m model was considered unnecessary. Thus, a 5x5 m model was formulated and investigated right from the beginning. A mesh dependency test was also carried out in order to determine the mesh sizing that is adequate to accurately predict the ultimate load carrying capacity of the shell.

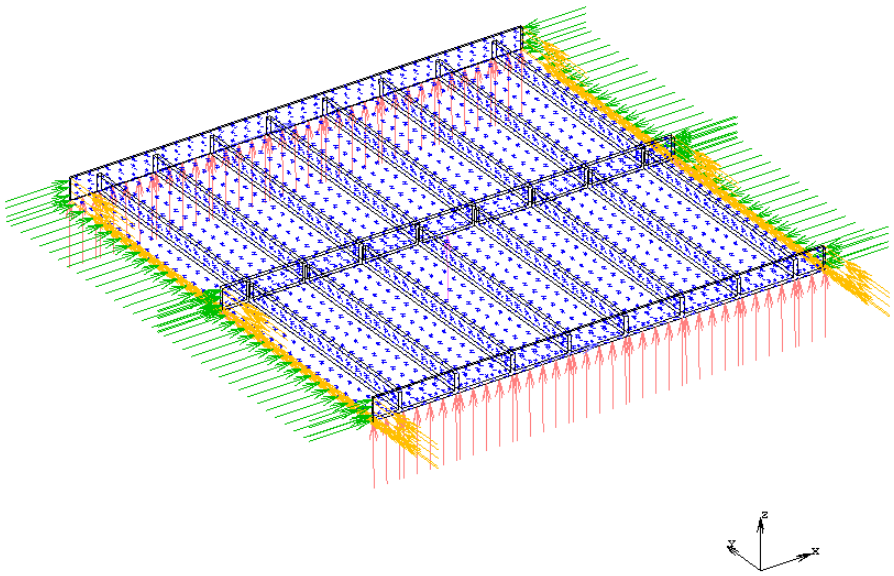

Figure 3.23 The repeating 5x5m unit as simulated with 8-node solid elements.

3.4.1 20mm Thick Skin Modal Buckle Analysis

The analysis of the 20mm thick solid model verifies the buckle modes predicted by the shell model and presented in the previous section. The buckling modes are shown in Figure 3.24 and Figure 3.25 and the calculated elastic buckling loads were

$$N_{bx} = 1467\ \text{kN/m}$$
$$N_{by} = 2771\ \text{kN/m}.$$

As the solid model had a mesh sizing of 145x153.438 mm, its results are comparable to those of the shell model consisting of 156x156 mm shell elements which were a buckling load of 1449 kN/m along the *x* direction and 2678 kN/m along the *y* direction. It should be noted that the two models are equivalent on the ground that with a similar meshing, similar buckling loads are calculated.

Institutional Repository - Library & Information Centre - University of Thessaly
20/05/2024 20:20:43 EEST - 3.139.81.117

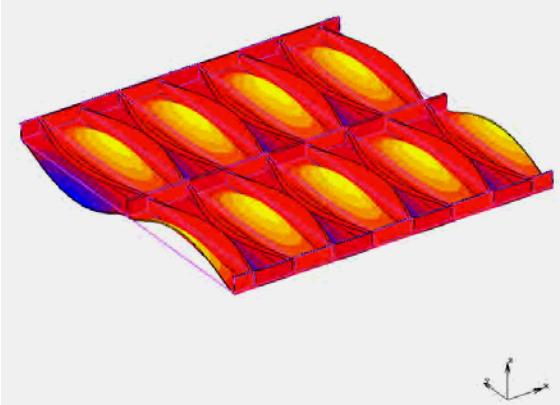

Figure 3.24 Buckle mode along the *x* axis.

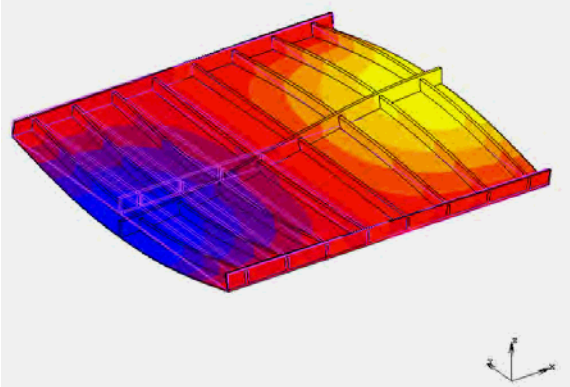

Figure 3.25 Buckle Mode along the *y* axis.

As with the shell model, a refined model was created and analysed. Each shell element was divided into two elements in each direction (1 element subdivided into 8 elements).The refined model (each skin element was now 72.5 x76.719 mm and there were two elements in the thickness direction) leaded to the following buckling loads:

$N_{bx} = 1333\ \text{kN/m}$

$N_{by} = 2748\ \text{kN/m}.$

It is obvious that the shell model converges more quickly to the actual critical load and thus is more efficient. A further refined solid model, in which each element of the previous one was now 8 new elements (subdivided into 2 in each direction) gave the results:

$N_{bx} = 1290\ \text{kN/m}$

$N_{by} = 2737\ \text{kN/m}.$

This mesh sizing (equivalent to the one of the 39x39 mm of the shell model) produces results similar to the ones produced by the 78x78 mm shell model. Thus, the solid model is considered less efficient than the shell one.

3.4.2 35mm Thick Skin Modal Buckle Analysis

The 35mm thick model with a mesh sizing for the subpanels of 145mm x 153.438 mm calculated the following elastic buckling loads along the *x* and *y* axis

$N_{bx} = 2859\ \text{kN/m}$

$N_{by} = 2905\ \text{kN/m}.$

The refined model (72.5 x76.719mm mesh sizing in plan)

$N_{bx} = 2835\ \text{kN/m}$

$N_{by} = 2882\ \text{kN/m}.$

The further refined model (36.25x38.36mm mesh sizing in plan)

$N_{bx} = 2824\ \text{kN/m}$

$N_{by} = 2871\ \text{kN/m}.$

Institutional Repository - Library & Information Centre - University of Thessaly
20/05/2024 20:20:43 EEST - 3.139.81.117

3.5 Modelling by the Use of Beam Elements and Shells, Hybrid Model

Finally, the third simulation method that was tested was a hybrid model, in which the grid of ribs was simulated by the use of 2-node beam elements (element 98 Timoshenko beam. See Appendix A) and the shell by type 75 4-node thick shell elements (Figure 3.26). The centers of mass of the shell elements were connected with the centers of the ribs-*y* with links while the real position of the center of the ribs-*x* was defined through an offset of the beam. Figure 3.27 provides a detail of the previous described hybrid model. First, two solid section beams were created and the properties of the rib sections were calculated by hand and inserted in MSC Marc.

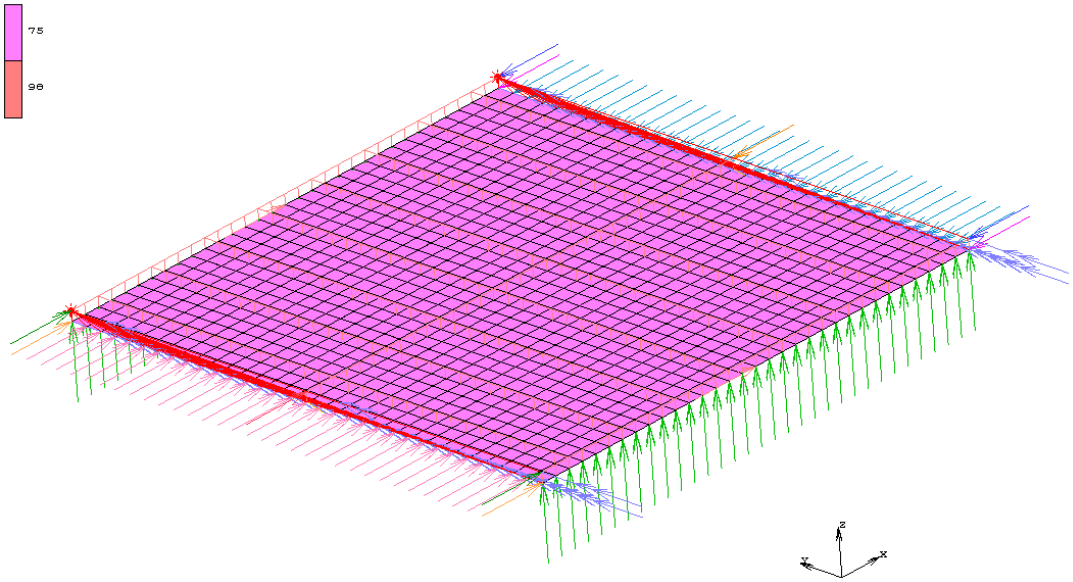

Figure 3.26 Hybrid Shell-Beam 5x5m Model

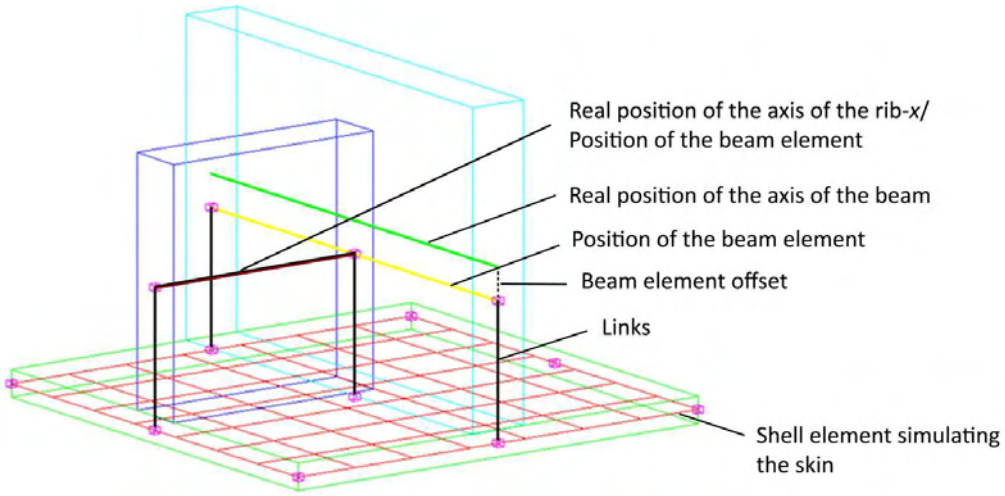

Figure 3.27 Hybrid model detail.

Institutional Repository - Library & Information Centre - University of Thessaly
20/05/2024 20:20:43 EEST - 3.139.81.117

3.5.1 20mm Thick Skin Modal Buckle Analysis

As with the solid model, a 5x5 m model was formulated from the beginning as it has already been determined that the structure will buckle locally in the *x* direction and globally in the *y* direction. The calculated properties of the beam elements for the 20mm thick shell are presented in the table below.

Properties for the line elements simulating the stiffeners and the links

Element	*H* (mm)	*t* (mm)	I_{11} (mm^4)	I_{22} (mm^4)	*J* (mm^4)	*A* (mm^2)	*G* (mm^2)	Offset mm
Rib - *x*	240	45	51840000	1822500	6428868.75	10800	10800	25
Rib - *y*	190	45	25721250	1442812.5	4910118.75	8550	8550	-
Links	-	-	infinite	1186523	infinite	7031	7031	-

*The outer ribs-*x* that only have half the cross section have all their properties divided by two

**The links that connect the outer rib-*x* have their properties divided by two

Loads

The compressive loading was imposed at nodal locations. The load at each node was calculated according to its effective area and so that no load eccentricity exists.

Direction	Skin load per node	Rib load per node
Parallel to the X axis	156.25*20*0.041118= 128.49375 KN	10800*0.041118 = 444.0744 KN
Parallel to the Y axis	156.25*20*0. 02969 = 92.78125 KN	8550 * 0.02969 = 253.8495 KN

*The outer ribs-*x* that only have half the cross section have their loads divided by two

Results

As expected, the stiffened shell buckled locally along the *x* axis and globally along the *y* axis (Figure 3.28 and Figure 3.29). The elastic buckling loads for each direction were:

$N_{bx} = 1396\ kN/m$

$N_{by} = 2673\ kN/m.$

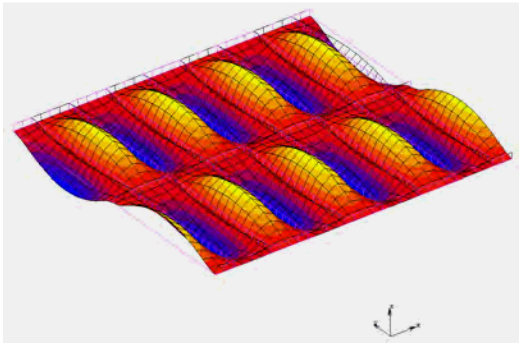

Figure 3.28 Buckle Mode along the x Axis

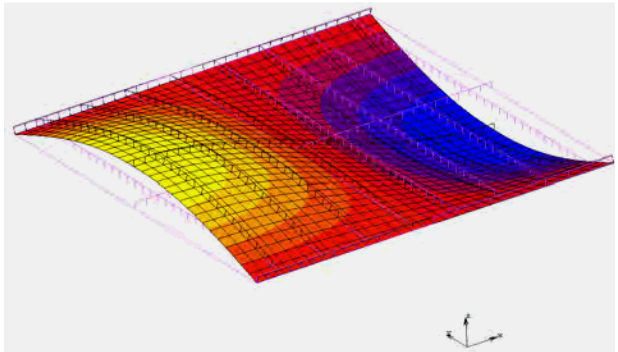

Figure 3.29 Buckle Mode along the y Axis

Institutional Repository - Library & Information Centre - University of Thessaly
20/05/2024 20:20:43 EEST - 3.139.81.117

Refined Model, Mesh Size 78.125x78.125mm

As with the previous models (shell and solid), in order to determine the effect of the mesh sizing on the predicted ultimate elastic buckling loads, the model was further refined and reanalyzed. The loads had to be recalculated as the effective area of each node was different. The recalculated nodal loads and the results of the analysis of the refined and doubly refined model are presented in the following pages.

Loads

Direction	Skin load per node	Rib load per node
Parallel to the X axis	78.125*20*0.041118 = 64.246875 KN	10800*0.041118 = 444.0744 KN
Parallel to the Y axis	78.125*20*0. 02969 = 46.390625 KN	8550 * 0.02969 = 253.8495 KN

Results

$N_{bx} = 1261\ \text{kN/m}$

$N_{by} = 2661\ \text{kN/m}.$

Doubly Refined Model, Mesh Size 39.0625x390625mm

Loads

Direction	Skin load per node	Rib load per node
Parallel to the X axis	39.0625*20*0.041118 = 32.1234375 KN	10800*0.041118 = 444.0744 KN
Parallel to the Y axis	39.0625*20*0. 02969 = 23.1953125 KN	8550 * 0.02969 = 253.8495 KN

Results

$N_{bx} = 1230\ \text{kN/m}$

$N_{by} = 2649\ \text{kN/m}$

3.5.2 35mm Thick Skin Modal Buckle Analysis

Properties for the line elements simulating the stiffeners and the links

Element	H (mm)	t (mm)	I_{11} (mm^4)	I_{22} (mm^4)	J (mm^4)	A (mm^2)	G (mm^2)	Offset mm
Rib - *x*	232.5	45	47130292	1765546.875	6201056.25	10462.5	10462	25
Rib - *y*	182.5	45	22793964.84	1385859.375	4682306.25	8212.5	8212.5	-
Rigid	-	-	infinite	1186523	infinite	7031	7031	-

*The outer rib-*x* that only have half the cross section have all their properties divided by two

**The links that connect the outer rib-*x* have their properties divided by two

Institutional Repository - Library & Information Centre - University of Thessaly
20/05/2024 20:20:43 EEST - 3.139.81.117

Loads

All the compressive loading was imposed as node loads. The load at each node was calculated according to its influence area and so that no load eccentricity was created.

Direction	Skin load per node	Rib load per node
Parallel to the X axis	156.25*35*0.02552 = 139.5625 KN	10462.5 *0.02552 = 267.003 KN
Parallel to the Y axis	156.25*35*0.02077 = 113.5859375 KN	8212.5 * 0.02077 = 170.574 KN

*The outer rib-*x* that only have half the cross section have their loads divided by two

Results

The analysis of the model verified the results of the shell and solid models. The structure buckled locally in both directions and the calculated elastic buckling loads were:

$N_{bx} = 2789\ \text{kN/m}$

$N_{by} = 2783\ \text{kN/m}.$

Refined Model, Mesh Sizing 78.125x78.125mm

Loads

Direction	Skin load per node	Rib load per node
Parallel to the X axis	78.125*35*0.02552 = 69.78125 KN	10462.5 * 0.02552 = 267.003 KN
Parallel to the Y axis	78.125*35*0.02077 = 56.79296875 KN	8212.5 * 0.02077 = 170.574 KN

Results

$N_{bx} = 2778\ \text{kN/m}$

$N_{by} = 2773\ \text{kN/m}.$

Doubly Refined Model, Mesh Sizing 39.0625x390625mm

Loads

Direction	Skin load per node	Rib load per node
Parallel to the X axis	39.0625*35*0.02552 = 34.890625 KN	10462.5 *0.02552 = 267.003 KN
Parallel to the Y axis	39.0625*35*0.02077 = 28.39648438 KN	8212.5 * 0.02077 = 170.574 KN

Results

$N_{bx} = 2774\ \text{kN/m}$

$N_{by} = 2769\ \text{kN/m}.$

Institutional Repository - Library & Information Centre - University of Thessaly
20/05/2024 20:20:43 EEST - 3.139.81.117

3.6 Summary and Discussion of the Results of the Modal Analysis in Each Direction

The two following tables summarize the results of the previous presented analyses. As a reminder the shell model refers to the model formulated solely by the use of 4-node thick shell elements, the solid model refers to the model consisting of 8-node solid elements while finally the hybrid model refers to the model that utilized 4-node thick shell elements to simulate the shell skin and 2-node Timoshenko beam elements for the grid of ribs. The "original" columns correspond to the results of the original mesh sizing (e.g. 156x156 mm for the shell elements) while the "refined" and "doubly refined" columns to the results calculated when each element was subdivided into two in each direction.

20mm Thick Ribbed Skin

	Shell Model			Solid Model			Hybrid Model		
Load (kN/m)	Original	Refined	Doubly Refined	Original	Refined	Doubly Refined	Original	Refined	Doubly Refined
N_{bx}	1449	1287	1245	1467	1333	1290	1396	1261	1230
N_{by}	2678	2665	2661	2771	2748	2737	2673	2661	2649

35mm Thick Ribbed Skin

	Shell Model			Solid Model			Hybrid Model		
Load (kN/m)	Original	Refined	Doubly Refined	Original	Refined	Doubly Refined	Original	Refined	Doubly Refined
N_{bx}	2792	2780	2776	2859	2835	2824	2789	2778	2774
N_{by}	2785	2774	2770	2905	2882	2871	2783	2773	2769

Institutional Repository - Library & Information Centre - University of Thessaly
20/05/2024 20:20:43 EEST - 3.139.81.117

Based on the results of the buckle analysis, it is safe to say that the dominant buckle shapes of the ribbed skin are the local buckling of the subpanels with the ribs following their deformation in the *x* direction and the global buckle between supports every 5m in the *y* direction. The main factor that affects the shape of buckling seems to be the thickness of the shell or, more accurately, the ratio of the stiffness of the skin to the stiffness of the supporting ribs. While in the case of the 20mm thick skin the structure buckle between the ribs along the *x* axis, when the thickness is increased to 35mm, the buckling between supports becomes dominant. In the *y* direction, the contribution of the ribs to the stiffness of the skin is only half of that of the ribs and thus the ribbed skin tends to buckle between the supports. This type of buckling behavior is common in stiffened steel and aluminum shells as former studies have shown (Paik et al. (2008); Mittelstedt (2007)(2009); Fujikubo et al(2006); Byklum et al (2004); Paik and Seo (2009)).

Ueda et al (1995) mention, concerning the buckling behavior of longitudinal stiffened shells, that the switch from overall to local buckling is governed by the relative stiffness ratio of the stiffeners to the shell γ, which is given by the relation

$$\gamma = EI_{sl} / b'D \quad (2)$$

where

I_{sl} is the moment of inertia of the stiffeners

b' is the spacing of the stiffeners

D is the bending resistance of the plate ($Et^3/12(1-\nu^2)$)

Thickness of shell	h_{sl} (mm)	b_{sl} (mm)	I_{sl}/b' (mm^4/mm)	D (mm^4)	γ
20mm	250	45	23437.5	673.4	34.8
35mm	250	45	23437.5	3609	6.5

Table 3.1 Calculation and comparison of the γ ratios

If γ is smaller than a certain value $\gamma_{\min}^{B}$ then the shell buckles in a global mode while if it is larger then the subpanels buckle locally. As we can see from the table above, the value of γ between the two cases under investigation differ significantly. Hence the difference in their behavior is justified. The value of $\gamma_{\min}^{B}$ depends upon the geometry and mechanical properties of the structure as well as the ratio of the load components in the two transverse directions. As again Ueda et al. (1995) mention, $\gamma_{\min}^{B}$ represents the intersection of the buckling curves of the two modes and provides a figure demonstrating this graphically (Figure 3.30).

We should keep in mind that the ribs in the perpendicular direction also resist the buckle between supports by their torsional resistance increasing the critical load. If the difference between the two ratios is relatively small, attention is required.

Institutional Repository - Library & Information Centre - University of Thessaly
20/05/2024 20:20:43 EEST - 3.139.81.117

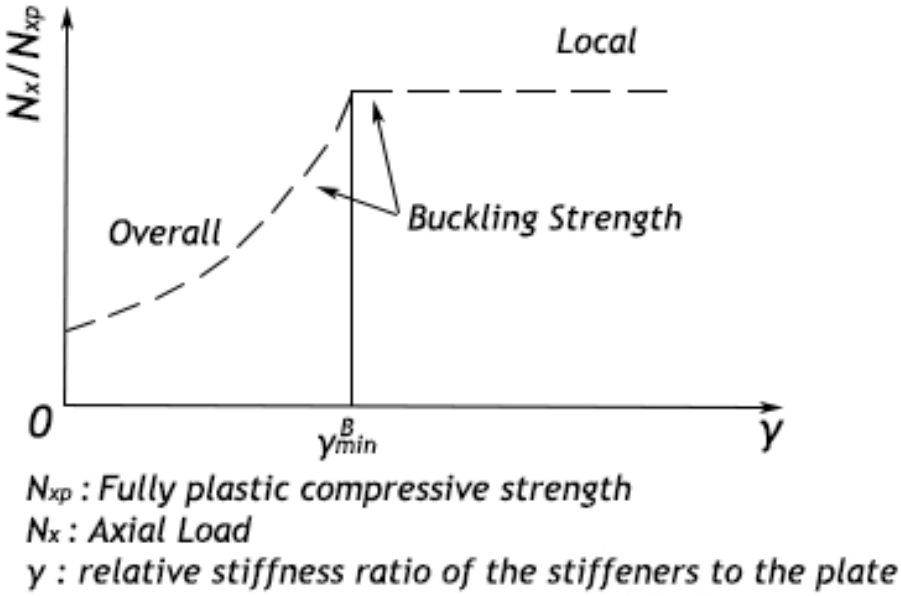

Figure 3.30 The buckling curves representing the two modes and their intersection $\gamma_{\min}^{B}$. Ueda et al. (1995)

Moreover, as the analyses have shown, another important factor governing the buckling behavior of the structure is the applied boundary conditions. These boundary conditions greatly affect the interaction between the global and local buckling modes. The interaction between buckling modes is more profound in the case of the 35mm thick shell, where depending on whether or not the outer spans provide rotational support to the inner region, the buckle mode in the *x* direction switches from a rather sinusoidal shape to a more complex chessboard-like one.

As far as the simulation method is concerned, if the structure at hand consists of a basic repeating unit, the modeled area, and thus the computational cost, can be reduced to the one of the basic unit by applying appropriate periodical boundary conditions. These boundary conditions should be carefully chosen according to the critical buckling mode so that they represent the real behavior of the structure. It seems that the most efficient way of simulation is by the use of a hybrid model. The hybrid model calculates the buckle load only with small error even with the original meshing of 156.25 x 156.25 mm. This is probably caused by the fact that the actual properties of the grid of ribs are calculated manually and inserted in the program by the user and thus are mesh independent and only the calculation of the bending stiffness of the skin depends on the mesh sizing. However, keeping in mind that the model will be used in a non-linear analysis in which the reinforcement of the ribs and the shell need to be simulated, the hybrid model is inappropriate. The shell model, compared to the solid one, converges to the actual buckle load with a mesh of lower density and so less computational time is required. Judging all the above, a shell model will in the sequel be used for the nonlinear analysis of the structure. If only an elastic analysis was to be performed the preferred way of modelling the structure would be by the use of a hybrid model.

Institutional Repository - Library & Information Centre - University of Thessaly
20/05/2024 20:20:43 EEST - 3.139.81.117

3.7 Interaction of the Axial Loads

After investigating the behavior of the stiffened shell for axial compression in each direction separately, and in order to fully comprehend the buckling behavior of the structure, the interaction of the axial loads in the *x* and *y* directions is investigated. Similarly to the previous set of analyses, a 5x5m model is formulated, with boundary conditions corresponding to the dominant buckling shapes and additional out of plane restrains (deflection equals to zero) at the positions of the point supports. The mesh sizing in the *x-y* plane was 78.125mm x 78.125mm and type 75 shell elements were used. The Elastic Moduli of the material used was 34000 N/mm^2 based on the properties of the concrete used while the Poisson's ratio was reduced to 0.1 to take into account the existence of bi-directional reinforcement and the additional stiffness of the supporting grid of ribs. The load was applied uniformly along the edges of the finite element, both on the skin and on the ribs, with its value depending on the thickness of the shell element, so that no eccentricity arises.

As Figure 3.31 and Figure 3.32 demonstrate, the axial load in the transverse direction reduces the bearing capacity of the ribbed shell. If the ratio of N_x / N_{bx} (applied axial load *x-x* to buckling load *x-x*) exceeds the value of 0.9, the buckling resistance in the *y* direction drops dramatically (Table 3.2 and Figure 3.31). This is cause by the change of the buckling mode from buckling between supports to buckling between ribs. On the other hand, when the thickness of the shell is increased, both directions buckle under the same axial load between the point supports (global mode) and therefore, as shown in Table 3.3 and Figure 3.32, the decrease of the bearing capacity is linear and symmetric as expected. This results are in agreement with former research on similar problems (Paik et al. (2008)). The results of the 35mm shell are also in agreement with equation (2.2 .1) by considering a = b = 5 and thus $e_1 = e_2 = 1$. In the case of the 20mm thick shell, the above equation can predict the buckling loads of the overall buckling but not the ones of the local one.

20mm thick skin

N_x (kN/m)	N_x/N_{bx}	N_y (kN/m)	N_y/N_{by}
0	0	2665	1
380.9	0.296	2285.4	0.858
592.5	0.460	2073.75	0.778
666.6	0.518	1999.8	0.750
761.8	0.592	1904.5	0.715
888.7	0.691	1777.4	0.667
1066	0.828	1599	0.6
1199	0.932	1199	0.450
1242	0.965	621	0.233
1287	1	0	0

Table 3.2 Interaction for 20mm thick shell.

Institutional Repository - Library & Information Centre - University of Thessaly
20/05/2024 20:20:43 EEST - 3.139.81.117

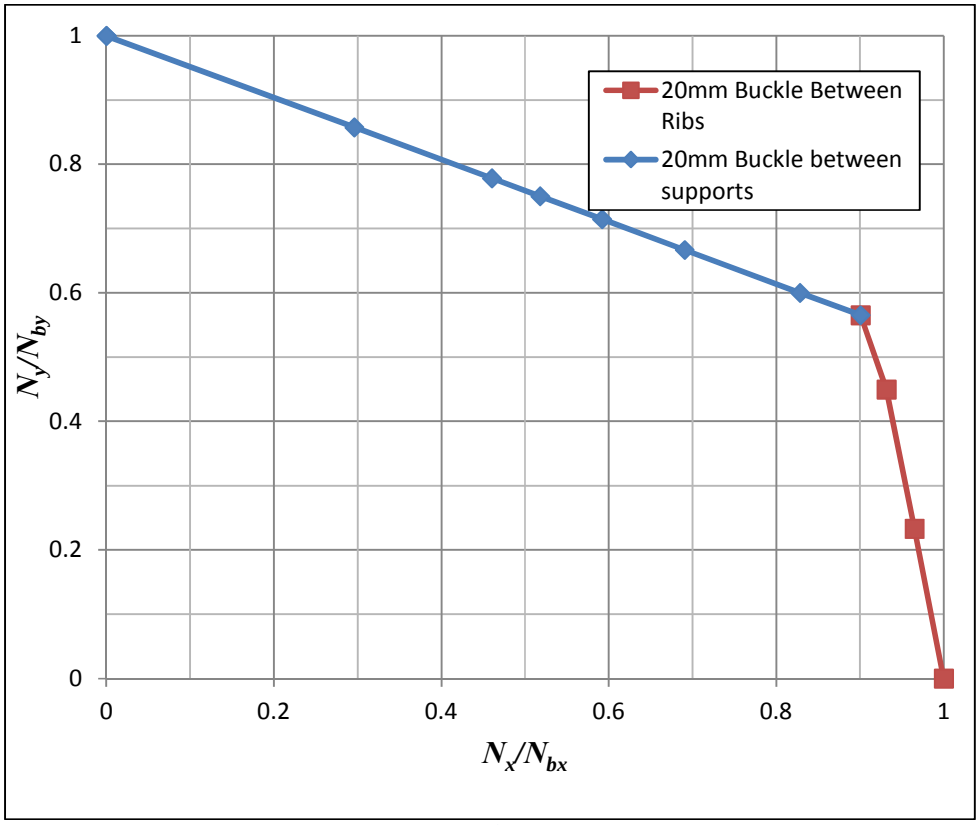

Figure 3.31 Interaction curve for the 20mm thick shell.

35mm thick

N_x (kN/m)	N_x/N_{bx}	N_y (kN/m)	N_y/N_{by}
0	0	2774	1
694	0.250	2082	0.751
925.5	0.333	1851	0.667
1389	0.450	1389	0.501
1852	0.666	926	0.334
2780	1	0	0

Table 3.3 Interaction for 35mm thick shell.

Institutional Repository - Library & Information Centre - University of Thessaly
20/05/2024 20:20:43 EEST - 3.139.81.117

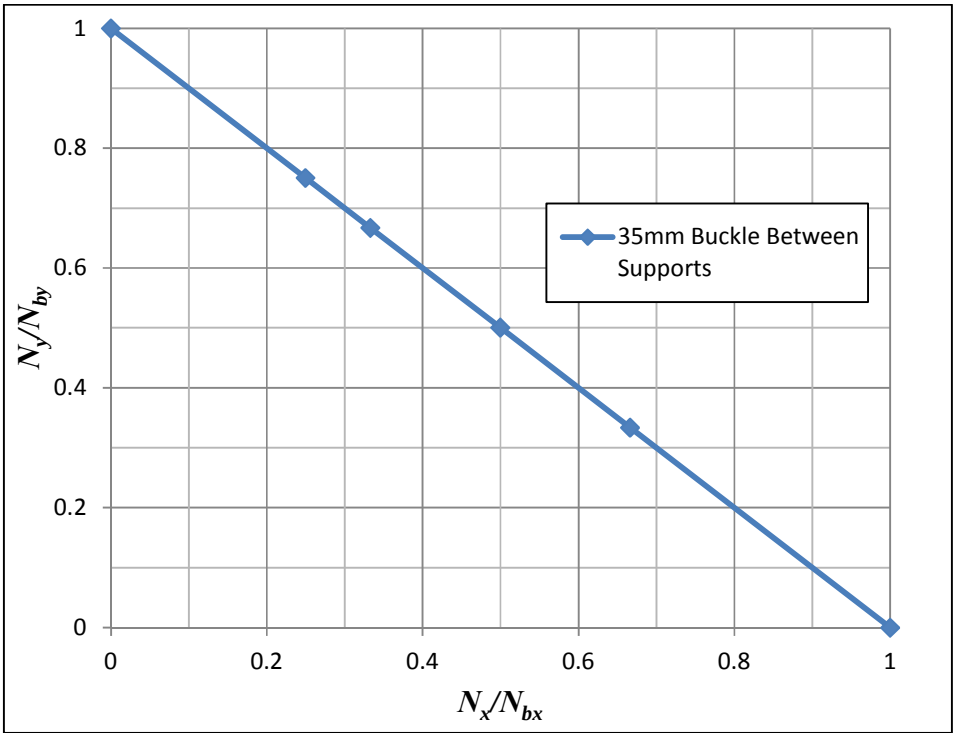

Figure 3.32 Interaction curve for the 35mm thick shell.

Institutional Repository - Library & Information Centre - University of Thessaly
20/05/2024 20:20:43 EEST - 3.139.81.117

4 Nonlinear Modeling of the Grid of Ribs

Before modeling the entire structure, consisting of the ferrocement skin and the ribs, a single reinforced rib-*y* was modelled and tested numerically, in order to verify that its bending behavior is accurately represented. As early as the late 80's (Bergan and Holand (1979)), methods and guidelines for the simulation of R/C elements existed. Two methods of modeling seem to be appropriate. The first one is to use shell elements to simulate the cement mortar and beam elements to simulate the reinforcing rods and mesh. The second method is to use composite layered shells to simulate the entire reinforced section.

Both simulation methods were examined by simulating a four point bending test around the strong axis in MSC Marc (2011). The behavior of the beam was not only investigated under pure bending but also under bending with axial force. The results of the analysis were compared with the ones calculated by the section designer of SAP 2000 v15 (2011) by direct integration of the section.

The models were solved by an iterative full Newton-Raphson procedure and the convergence criterion was based on residual forces. Second order effects were not taken under consideration as the scope of this investigation is to verify that material nonlinearity is accurately simulated. The Tresca criterion was used for the concrete mortar and the Von Mises for the reinforcing steel. Finally, for the second method three cases were investigated regarding the strain limitations. The first set of analyses had no strain limitations, the second one considered an ultimate concrete compressive strain under pure compression $\varepsilon_{xu,c}$ = 0.2%, an ultimate concrete compressive strain under bending $\varepsilon_{xu,b}$ = 0.35% and an ultimate steel tensile strain ε_{su} = 2 %. The third case limited the material in the elastic region.

4.1 Geometry and Reinforcing Pattern of the Rib

The geometry of the tested cross section and its reinforcing pattern were based on the ones of the ribs-*y* and are shown in Figure 4.1. The rib under study was 5 meters long and since the loading and geometry were symmetrical, only half the rib was simulated. The zone of constant moment was 2031.25 mm long while the lever arm 1484.375.

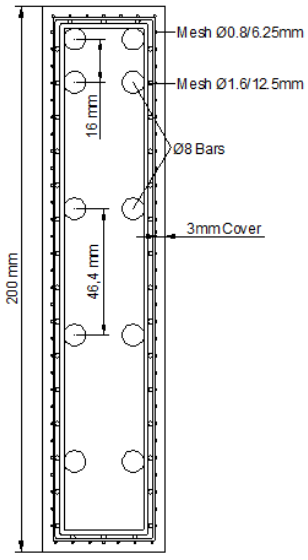

Figure 4.1 Cross Section of the Rib

Institutional Repository - Library & Information Centre - University of Thessaly
20/05/2024 20:20:43 EEST - 3.139.81.117

4.2 Modeling by the Use of Shell and Beam Elements

The concept of the method is to use shell elements to simulate the cement mortar of the rib and beam elements for the rods and mesh reinforcement. As (Bergan and Holand (1979) mention the finite element mesh division is restricted as common nodes are required in order to combine the reinforcement and concrete elements. Thus the shell elements had a height restricted by the position of the reinforcement rods, while the mesh reinforcement is added to the main reinforcement according to the effective zone of each main reinforcement node. The vertical wires are actually the shear reinforcement of the rib and are simulated as beam elements every 78,125 mm, which is the mesh division along the longitudinal axis.

4.2.1 Material Properties and Preliminary Calculations

Two materials were created in MSC Marc. The first one representing the C60 cement mortar was considered isotropic with a Young's modulus of 34000 MPa and a bilinear constitutive law. The ultimate compressive stress of the concrete was considered to be 40 MPa, while under tension it was considered to have an ultimate strength of 2 MPa with a softening modulus of 34000MPa. Plasticity and cracking were handled by the built-in capabilities of the finite element analysis program MSC Marc and the Tresca yield criterion was used. The material simulating the reinforcing steel was also considered isotropic, with a Young's Modulus of 200000 MPa. The plasticity law was bilinear with a yield stress of 435 MPa and the Von Mises criterion was used. Finally, no strain limitations were imposed in the analysis.

	Behavior	E (MPa)	f_{cd} / f_{yd} (MPa)	f_{ctd} (MPa)
Concrete C60/75	Isotropic Elastic-perfectly plastic	34000	40	2 Cracking with softening modulus 34000 MPa
Steel B500c	Isotropic Elastic-perfectly plastic	200000	435	-

Table 4.1 Material Properties

*No strain restrictions are imposed on the model ($\varepsilon_u = \infty$)

The coordinates of the beams simulating the reinforcement rods are derived by the geometry of the section. The effective height of each internal node was considered to be half the distance between its upper and lower nodes. As far as the external nodes are concerned, they are considered to gather half the reinforcement mesh between them and the lower or upper node and the mesh between them and the outer edge of the section taking into account the 3mm cement cover (Figure 4.2) . The rods are simulated as circular beams of diameter depending on their total area of reinforcement. Table 4.2 summarizes the data of the reinforcement layers.

Institutional Repository - Library & Information Centre - University of Thessaly
20/05/2024 20:20:43 EEST - 3.139.81.117

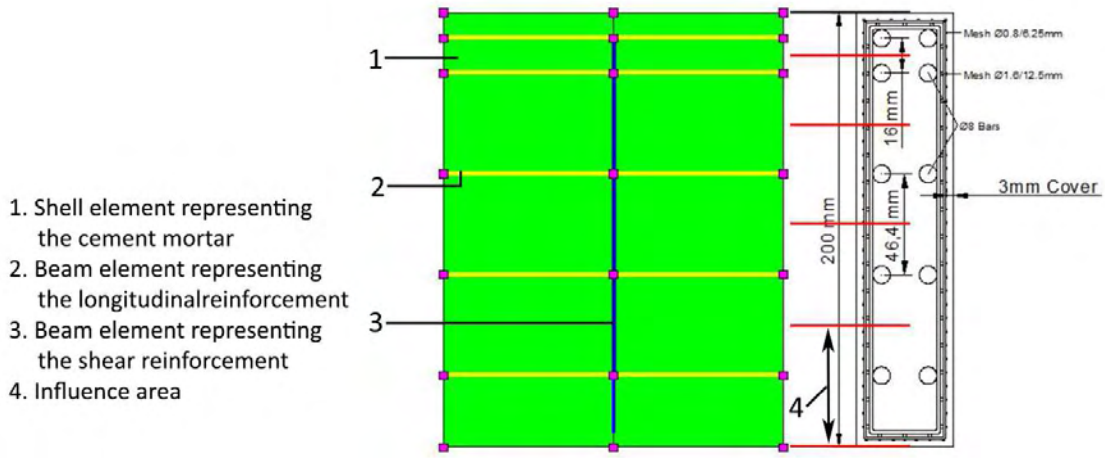

Figure 4.2 The beam-shell elements model.

Reinforcement layer	Coordinates mm	As of mesh mm^2	As of Reinforcement rods mm^2	Total As mm^2	Diameter of beam element mm
1	11.8	15.200	2C8 = 100.531	115.731	12.139
2	27.8	15.056	100.531	115.587	12.131
3	74.2	22.390	100.531	122.921	12.510
4	120.6	22.390	100.531	122.921	12.510
5	167	28.567	100.531	129.098	12.821

Table 4.2 Properties of the Reinforcement Layers.

Shear reinforcement = (0.080+0.161)*78.125*2 = 37.699 mm^2
Equivalent Diameter = 6.928 mm

4.2.2 Results for Strong Axis Bending

While SAP reduces the area of the concrete by the area of the reinforcement, the model in Marc has overlaps. Therefore, another section was created in SAP 2000 that calculates the resistance of a section with material overlaps. Both results are presented as the comparison between *"Marc"* and *"SAP with Overlaps"* measures the error between the model and the classic strain compatibility theory applied in reinforced concrete elements, while the comparison between *"Marc"* and *"SAP"* measures the error between the model and what would be closer to reality.

Analysis	M_{rd} (+ve) kNm	M_{rd} (-ve) kNm
MARC (shell-beam model)	16.729	21.24
SAP with Overlaps (direct integration)	16.72	20.91
SAP (direct integration)	16.56	20.66

Table 4.3 Comparison of the results for pure bending between the models.

Institutional Repository - Library & Information Centre - University of Thessaly
20/05/2024 20:20:43 EEST - 3.139.81.117

4.2.3 M-N Interaction

SAP 2000 performs all calculations with the axial load applied at the center of the concrete section rather than the center of mass of the section, so in order for the results to be comparable, the axial load in the model in Marc was also applied at the center of the concrete section. Table 4.4 and Figure 4.3 present the results of the M-N Interaction Analysis according to SAP 2000 V15 and MSC Marc 11. The comparison of the results shows that the shell – beam model accurately simulates the bending behavior of the rib cross section.

	Sap	Marc
N (kN)	M (kNm)	M (kNm)
0	16.72	16.73
-50	19.23	19.44
-100	20.59	21.08
-150	21.83	22.41
-200	22.93	23.45
-250	22.85	23.72
-300	21.81	22.97
-350	20.73	21.98
-400	19.36	20.64
-478	15.14	16.82
-478	-9.11	-9.82
-400	-14.3	-15.45
-350	-17.72	-18.63
-300	-19.96	-20.51
-250	-21.23	-21.9
-200	-22.47	-23.11
-150	-23.42	-23.91
-100	-23.07	-23.35
-50	-21.99	-22.4
0	-20.91	-21.24

Table 4.4 Results of the M-N Interaction Analysis.

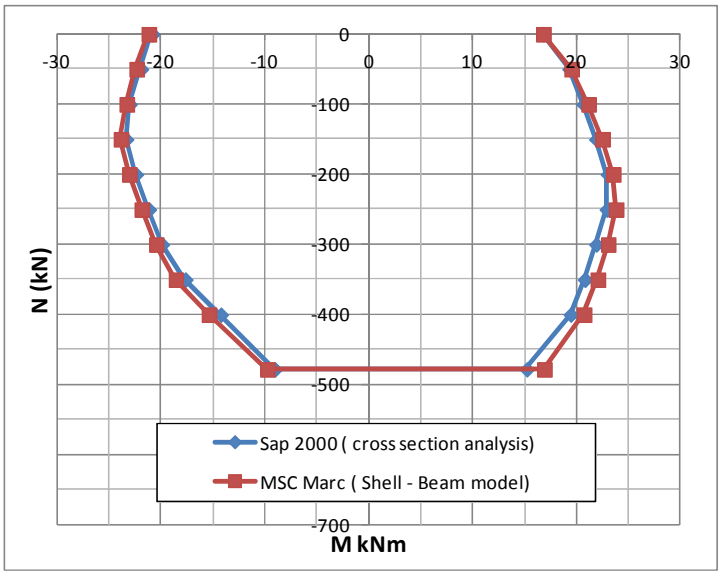

Figure 4.3 M-N Interaction Curves According to SAP and the Shell-Beam Model in Marc.

Institutional Repository - Library & Information Centre - University of Thessaly
20/05/2024 20:20:43 EEST - 3.139.81.117

4.3 Modeling by the Use of Composite Layered Shell Elements

This method of simulation of reinforced concrete elements utilizes layered composite shell elements. The reinforcement rods and mesh are simulated by equivalent reinforcement layers that have stiffness only in the direction of the reinforcement wires and rods. The main advantage of this method is that very few restrictions are imposed to the finite element mesh division and the exact position of the reinforcement rods in the thickness direction can be modeled. Two models were formulated. The first one considered the reinforcement concentrated at the location of the main reinforcement rods. This model is equivalent to the shell-beam elements model and provides a good comparison of the two simulation methods when similar assumptions are made. The second model, named "detailed", fully utilizes the capability of the composite shell model to accurately simulate the actual position of the reinforcing rods and meshes. This model is compared to a model formulated in the section designer module of SAP2000 that simulates the reinforcing steel in its actual position so that the real behavior of the rib according to the fiber model direct integration theory is calculated.

4.3.1 Material Properties

For the simulation by the use of composite layered shells three materials were created in MSC Marc. The first one representing the C60 cement mortar was identical to the one used in the beam shell simulation method. It was considered isotropic with a Young's modulus of 34000 MPa and a bilinear constitutive law, it had an ultimate compressive stress of the concrete was of 40 MPa, while under tension it was considered to have an ultimate strength of 2 MPa with a softening modulus of 34000MPa. Plasticity and cracking were handled by the built-in capabilities of the finite element analysis program MSC Marc and the Tresca yield criterion was used. As reinforcement is considered to have stiffness only in its longitudinal direction, two materials were created to simulate the B500c steel. Both of them were considered orthotropic and had a Young's modulus of 200000 MPa in one only direction. Thus, a steel material with stiffness along the 1st local axes of the shell element was created (B500c-*x*) and another one with stiffness only parallel to the 2nd local axis of the shell (B500c-*y*). Both material had a bilinear constitutive law with a yield stress of 435 MPa. The Von Mises criterion was used and no strain limitations were imposed in the analysis at this point.

	Behavior	E (MPa)	f_{cd} / f_{yd} (MPa)	f_{ctd} (MPa)
Concrete C60/75	Isotropic Elastic-perfectly plastic	34000	40	2 Cracking with softening modulus 34000 MPa
Steel B500c	Orthotropic Elastic-perfectly plastic	200000 only in the direction of the reinforcement	435	-

Table 4.5Material Properties.

No strain restrictions are imposed on the model ($\varepsilon_u = \infty$)

Institutional Repository - Library & Information Centre - University of Thessaly
20/05/2024 20:20:43 EEST - 3.139.81.117

4.3.2 Preliminary Calculations for concentrated reinforcement at the location of the main rods

The coordinates of the beams simulating the reinforcement rods are derived by the geometry of the section. The effective height of each internal node was considered to be half the distance between its upper and lower nodes. As far as the external nodes are concerned, they are considered to gather half the reinforcement mesh between them and the lower or upper node and the mesh between them and the outer edge of the section taking into account the 3mm cement cover. Based on the diameter of the main rods, each composite element was 8 mm high and had two reinforcement layers in the longitudinal direction (one in each side) and two in the transverse one, acting as shear reinforcement. The equivalent thickness of each longitudinal reinforcement layer is $(A_s/2)/8$. Table 4.6 and Table 4.7 present the calculation of the reinforcement area A_s per layer and the composition of the composite shell element respectively. Figure 4.4 and Figure 4.5 present the two composite layered shells used in this set of analyses, while Figure 4.6 demonstrates the simulation of the rib section by the use of two shell elements.

Reinforcement layer	Coordinates mm	As of mesh mm^2	As of Reinforcement rods mm^2	Total As mm^2	Equivalent Thickness mm
1	11.8	15.200	2C8 = 100.531	115.731	7.233
2	27.8	15.056	100.531	115.587	7.224
3	74.2	22.390	100.531	122.921	7.686
4	120.6	22.390	100.531	122.921	7.686
5	167	28.567	100.531	129.098	8.069

Table 4.6 Properties of the Reinforcement Layers

Shear reinforcement = (0.0804+0.161) = 0.241mm
Distance of longitudinal reinforcement from edge = 3+(2*0.8+2*1.6+8)/2 = 9.4
Distance of shear reinforcement from edge = 3+(2*0.8+2*1.6)/2 = 5.4

Material	Thickness mm					representation
	reinforcement layer 1	reinforcement layer 2	reinforcement layer 3 & 4	reinforcement layer 5	concrete with shear reinforcement	
C60	2.640	2.640	2.640	2.640	2.640	Cover
C60	2.640	2.640	2.640	2.640	2.640	Cover
B500c *y*	0.241	0.241	0.241	0.241	0.241	Shear reinforcement
C60	0.268	0.267	0.038	0.045	4.245	Concrete between reinforcement
B500c *x*	3	7.224	7.686	8.069	4.245	Longitudinal reinforcement
C60	4.742	4.744	4.629	4.433	4.245	Concrete between reinforcement
C60	4.742	4.744	4.629	4.433	4.245	Concrete between reinforcement

Table 4.7 Composition of Shell Elements Used in the Model.
Due to symmetry only half the section is presented

Institutional Repository - Library & Information Centre - University of Thessaly
20/05/2024 20:20:43 EEST - 3.139.81.117

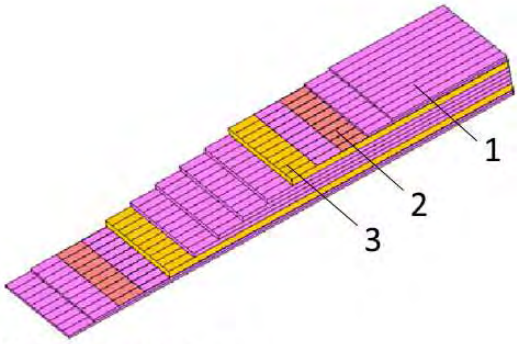

1 C60 cement mortar
2 Shear reinforcement layer
3 Longitudinal reinforment layer

Figure 4.4 Composite representing the reinforced layers

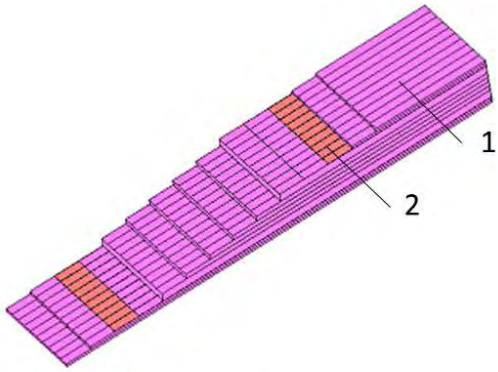

1. C60 cement mortar
2. Shear reinforcement layer

Figure 4.5 composite representing the concrete with shear mesh reinforcement

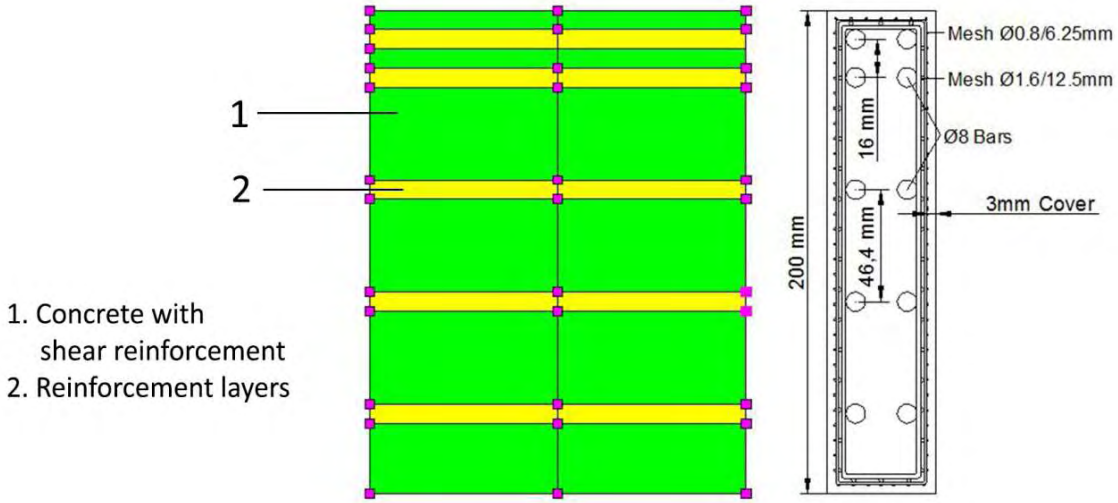

Figure 4.6 Rib section with the various composite shell elements

4.3.3 Results for Strong Axis Bending for concentrated reinforcement at the location of the main rods

In contrast to the shell-beam model, the composite layered shell has no overlaps, thus it is closer to the actual cross section and there is no need to compare the results to a SAP2000 with overlaps section. Table 4.8 presents the results of the numerical analysis of the composite layered shell model with the assumption that all reinforcing steel is concentrated at the position of the Ø8 rods. As a reminder, the shell-beam model calculated an ultimate bending moment resistance of 16.729 kNm and 21.24 kNm for positive and negative bending respectively. The difference between the two models is relatively small, with the composite shell being closer to

Institutional Repository - Library & Information Centre - University of Thessaly
20/05/2024 20:20:43 EEST - 3.139.81.117

the actual resistance of the rib. This is caused by the fact that the reinforcement is considered to be distributed at an area of 8mm height, rather than a point element. As mentioned before, no material overlaps exist. It should be noted that the model in SAP2000 also assumes that all the steel is concentrated at the location of the Ø8 rods and thus the error measures the difference between the fiber model direct integration theory (SAP2000) and the composite layered shell numerical analysis.

Analysis	M_{rd} (+ve) kNm	M_{rd} (-ve) kNm
MARC (composite shells)	16.625	21.24
SAP (direct integration)	16.56	20.66

Table 4.8 Comparison of the Bending Resistance Calculated by Marc and SAP

4.3.4 M-N Interaction for concentrated reinforcement at the location of the main rods

SAP2000 performs all calculations with the axial load applied at the center of the concrete section rather than the center of mass of the section, so in order for the results to be comparable the axial load in the model in Marc is also applied at the center of the concrete section. Table 4.9 and Figure 4.7 present the results of the M-N Interaction Analysis according to SAP2000 V15 and MSC Marc 11.

	Sap	Marc
N (kN)	M (kNm)	M (kNm)
0	16.56	16.625
-50	18.87	18.94
-100	20.20	20.45
-150	21.49	21.73
-200	22.42	22.68
-250	22.01	22.53
-300	20.98	21.60
-350	20.73	20.51
-400	18.21	19.04
-450	15.16	16.22
-450	-8.86	-10.08
-400	-12.47	-13.69
-350	-16.06	-17.09
-300	-18.77	-19.49
-250	-20.25	-20.96
-200	-21.54	-22.23
-150	-22.70	-23.19
-100	-22.69	-22.99
-50	-21.69	-22.03
0	-20.66	-21.24

Table 4.9 Results of the M-N Interaction Analysis

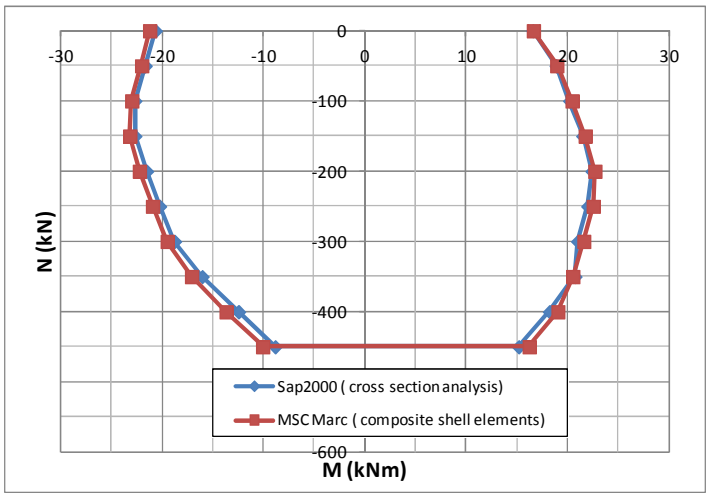

Figure 4.7 M-N Interaction Curves According to SAP and the Composite Model in Marc

Institutional Repository - Library & Information Centre - University of Thessaly
20/05/2024 20:20:43 EEST - 3.139.81.117

4.3.5 Detailed Model

Finally a detailed model is formulated with two types of composite shells. The first shell is used to simulate the cross section at the location of the reinforcement Ø8 rods (Figure 4.8) while the second one the section between main reinforcement layers where cement mortar with only mesh reinforcement exists (Figure 4.9). Each reinforcement layer on the actual cross section is simulated as a equivalent layer of steel in the model. Also a beam element is used in order to simulate the mesh reinforcement at the upper and lower edge of the stiffener.

Figure 4.10 presents the simulation of the rib by the use of these three elements.

Material	Thickness mm	representation
C60	1.680	cover
C60	1.680	cover
B500c X	0.080	Longitudinal reinforcement
C60	0.720	Concrete between reinforcement
B500c Y	0.080	Shear reinforcement
C60	1.079	Concrete between reinforcement
B500c X	0.161	Longitudinal reinforcement
C60	1.439	Concrete between reinforcement
B500c Y	0.161	Shear reinforcement
C60	1.578	Concrete between reinforcement
B500c X	6.283	Longitudinal reinforcement
C60	3.779	Concrete between reinforcement
C60	3.779	Concrete between reinforcement

Beam element at edge *As* = 3.016 mm2 + 4.021 mm2, thus, diameter of element = 2.993 mm

Institutional Repository - Library & Information Centre - University of Thessaly
20/05/2024 20:20:43 EEST - 3.139.81.117

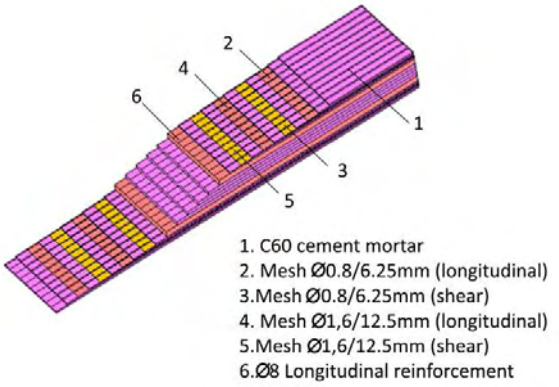

Figure 4.8 Composite representing the reinforced layers.

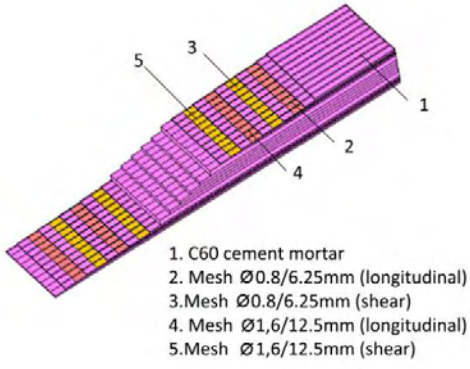

Figure 4.9 composite representing the concrete with mesh reinforcement.

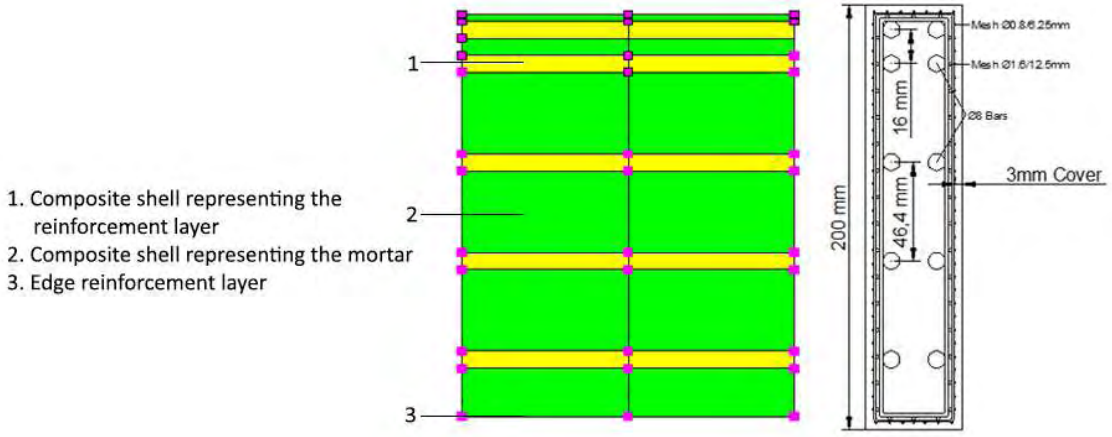

Figure 4.10 The simulation of the rib by the use of the two different composite shells.

4.3.6 Results for Strong Axis Bending for the detailed model

As this model is considered to by a detailed simulation of the rib-*y* cross section, it is compared to a section created in the section designer module of SAP2000 that all reinforcement rods and meshes are drawn in their actual position. This is considered to be the actual behavior of the rib cross section. Table 4.10 demonstrates the results obtained by the numerical analysis (MARC) and the ones obtained by direct integration of the cross section (SAP2000). As it is shown, the error of the numerical simulation is very small.

Analysis	M_{rd} (+ve) kNm	M_{rd} (-ve) kNm
MARC (composite shells)	17.055	21.34
SAP (direct integration)	17.15	21.15

Table 4.10 Comparison of the Bending Resistance Calculated by Marc and SAP

Institutional Repository - Library & Information Centre - University of Thessaly
20/05/2024 20:20:43 EEST - 3.139.81.117

4.3.7 M-N Interaction for the detailed model

As it is going to be used for the calculation of the ultimate plastic buckling load it is important that the simulation method used in the nonlinear analysis accurately simulates the behavior of the cross section under the presence of compressive loading. Thus, the M-N interaction curve of the composite layered shell detailed model is calculated and compared to the one obtained by SAP2000. As mentioned before, due to the fact that SAP 2000 performs all calculations with the axial load applied at the center of the concrete section, in Marc the axial load is also applied at the center of the concrete section. Table 4.11 and Figure 4.11 present the results of the M-N Interaction Analysis according to SAP 2000 V15 and MSC Marc 11 for the detailed model. The comparison of the results show that the results of the numerical model are in accordance with the ones calculated by integration of the cross section.

	Sap	Marc
N (kN)	M (kNm)	M (kNm)
0	17.15	17.06
-50	19.42	19.44
-100	20.79	20.99
-150	22.08	22.25
-200	22.86	23.1
-250	22.51	22.96
-300	21.48	22.06
-350	20.42	20.96
-400	18.57	19.39
-450	15.61	14.81
-450	-9.52	-8.59
-400	-13.13	-14.29
-350	-16.66	-17.575
-300	-19.27	-19.94
-250	-20.81	-21.48
-200	-22.1	-22.72
-150	-23.14	-23.59
-100	-23.12	-23.36
-50	-22.18	-22.44
0	-21.15	-21.34

Table 4.11 Results of the M-N Interaction Analysis

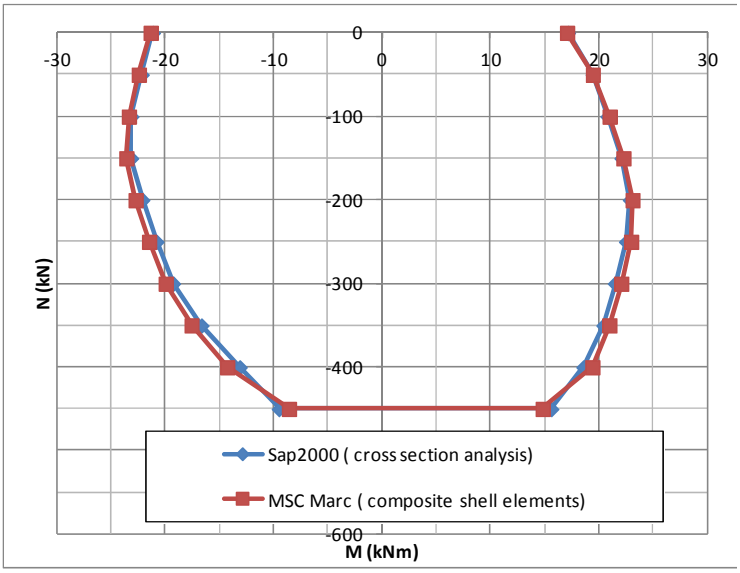

Figure 4.11 M-N Interaction Curves According to SAP and Composite Detailed Model in Marc. No Strain Restrictions.

Institutional Repository - Library & Information Centre - University of Thessaly
20/05/2024 20:20:43 EEST - 3.139.81.117

4.3.8 M-N Interaction for the detailed model elastic design

For the analysis of such structures and depending both on the material used and the analysis and design procedure the designer may have to impose certain strain or stress limitations to the numerical model. Thus, to further examine the accuracy of the model and verify that the material nonlinearity is accurately taken under consideration, a comparison between the elastic capacity of the section, as calculated by direct integration of the section (SAP2000) and the one calculated by a four point bending test in MSC Marc, is performed. Table 4.12 and Figure 4.12 demonstrate this comparison. As seen from Figure 4.12 the detailed composite shell model accurately simulates the behavior of the cross section both for pure bending and under the presence of compressive axial loads.

	Sap	Marc
N (kN)	M (kNm)	M (kNm)
0	9.78	9.69
-50	11	10.93
-100	10.85	11.01
-150	10.75	10.92
-200	10.36	10.40
-250	9.27	9.17
-300	7.66	7.45
-350	6.08	5.75
-400	4.49	4.074
-450	2.9	2.50
-450	2.9	2.50
-400	-1.05	-0.95
-350	-2.89	-2.87
-300	-5.30	-4.92
-250	-6.63	-6.78
-200	-8.32	-8.66
-150	-9.51	-9.90
-100	-10.45	-10.73
-50	-11.44	-11.81
0	-12.52	-12.61

Table 4.12 Results of the M-N Interaction Analysis

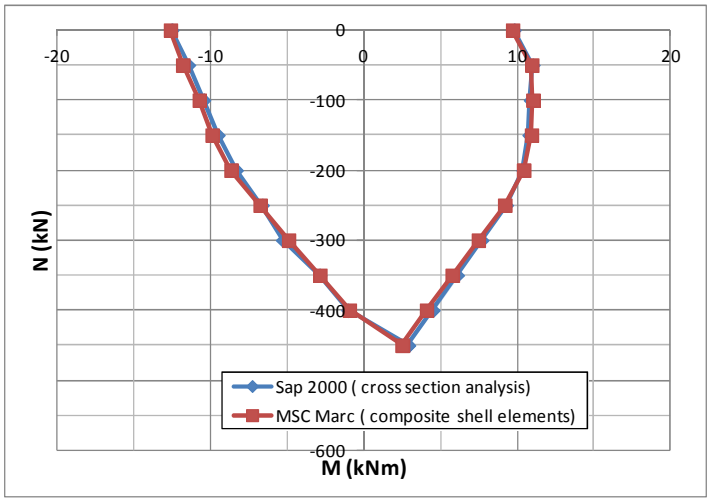

Figure 4.12 M-N Interaction Curves According to SAP and Composite Detailed Model in Marc. Elastic Region.

Institutional Repository - Library & Information Centre - University of Thessaly
20/05/2024 20:20:43 EEST - 3.139.81.117

4.3.9 M-N Interaction for the Detailed Model with Strain Limitation

Finally, a last set of analysis is performed by imposing strain limitations to the materials according to the corresponding regulations and standards. Table 4.13 and Figure 4.13 summarize the results of the analysis. Again, the results verify that the detailed model accurately simulates the cross section of the rib-*y*.

Ultimate concrete compressive strain under pure compression $\varepsilon_{xu,c}$ = 0.2%
Ultimate concrete compressive strain under bending $\varepsilon_{xu,b}$ = 0.35%
Ultimate steel tensile strain ε_{su} = 2 %

	Sap	Marc
N (kN)	M (kNm)	M (kNm)
0	16.44	16.7
-50	18.67	18.85
-100	20.33	20.40
-150	20.82	20.97
-200	20.92	21.18
-250	20.06	20.32
-300	18.93	19.27
-350	17.56	17.9
-400	15.84	16.25
-450	13.68	12.78
-450	-7.08	-5.63
-400	-10.06	-10.26
-350	-12.61	-12.94
-300	-14.88	-15.11
-250	-16.95	-17.25
-200	-18.87	-18.94
-150	-20.62	-20.63
-100	-21.20	-21.48
-50	-21.23	-21.20
0	-20.49	-20.53

Table 4.13 Results of the M-N Interaction Analysis

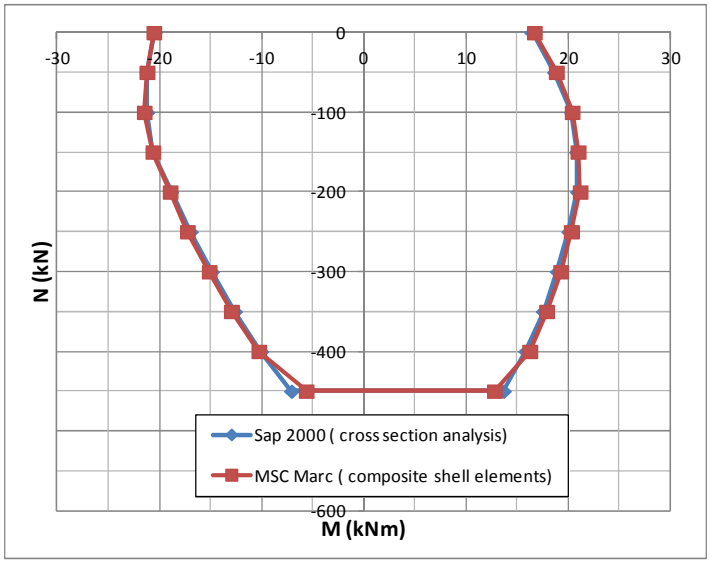

Figure 4.13 M-N Interaction Curves According to SAP and Composite Detailed Model in Marc. Strain restrictions.

Institutional Repository - Library & Information Centre - University of Thessaly
20/05/2024 20:20:43 EEST - 3.139.81.117

4.4 Discussion of the Results

It is obvious that the most accurate results are achieved by the use of a detailed model in which all reinforcement layers and rods are simulated at their actual position, both in the height and in the thickness directions. The results for bending around the strong axis and M-N interaction of all models in Marc are in agreement to the results calculated by direct integration of the corresponding cross section. Thus, no significant error arises from the use of composite layered shells. However, the model that most efficiently simulate the behavior of the actual rib is the detailed one, because, in comparison to the beam shell model, overlaps of material do not exist and compared to the other composite shell models, it simulates more accurately the position of all reinforcement rods and meshes. Also, for various strain limitations, the detailed composite shell model accurately calculates the ultimate bending resistance. Figure 4.14 presents a comparison of the ultimate capacity of the rib for various strain limitations. Finally, needless to say that the out of plane bending of the rib can only be simulated by composite shell models because a beam shell model cannot simulate the position of the steel mesh and rods in the thickness direction. This is more clearly demonstrated in the next section where the modeling of the shell is discussed.

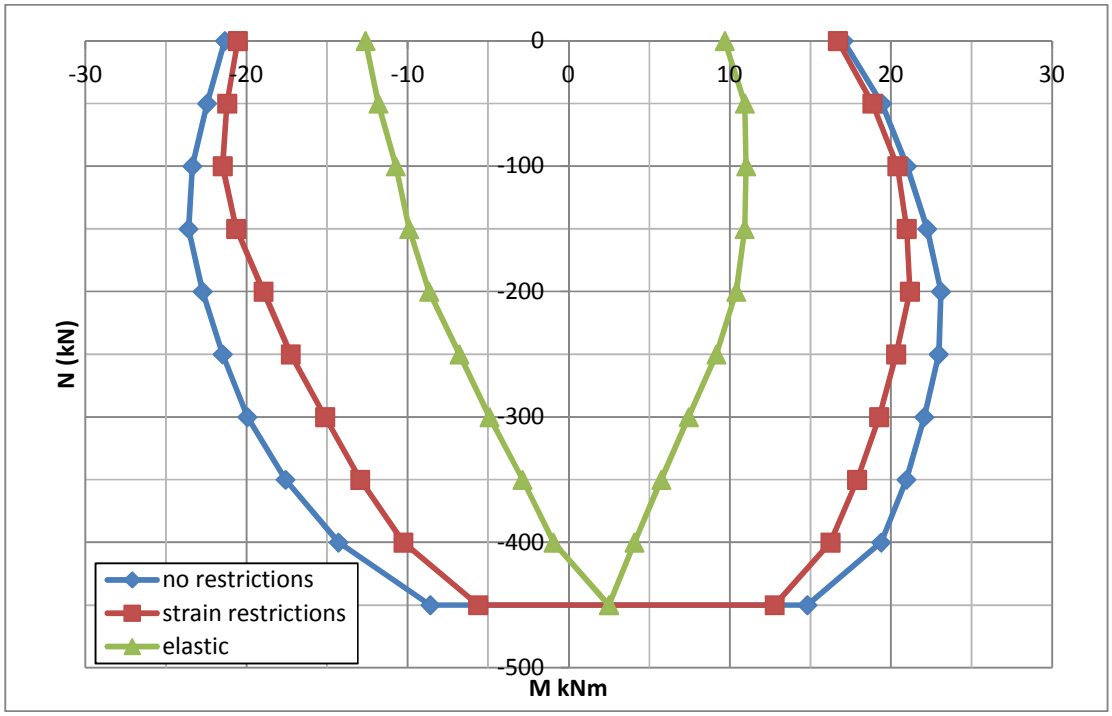

Figure 4.14 Summary of the M-N Interaction Curves According to the Detailed Numerical Model

Institutional Repository - Library & Information Centre - University of Thessaly
20/05/2024 20:20:43 EEST - 3.139.81.117

5 Nonlinear Modeling of the Shell

As with the grid of ribs, before proceeding to a nonlinear finite element analysis the validation of the modelling technique regarding the material nonlinearity is necessary. As the out of plane bending needs to be simulated, a composited layered shell model was used. Each layer of reinforcement rods was simulated as an equivalent layer of steel. Bond slip effects where not taken under consideration. The models were solved by an iterative full Newton-Raphson procedure and the convergence criterion was based on residual forces. Second order effects were not taken under consideration as the scope of this investigation is to verify that material nonlinearity is accurately simulated and not geometrical nonlinearity.

5.1 Material Properties and Geometry

For the modeling of the ferrocement shell a composite material was created in MSC Marc 2011 that consists of grade C60 concrete and B500C reinforcing steel. Again, three materials were created in MSC Marc. The first one representing the C60 cement mortar was considered isotropic with a Young's modulus of 34000 MPa and a bilinear constitutive law, it had an ultimate compressive stress of the concrete of 40 MPa, while under tension it was considered to have an ultimate strength of 2 MPa with a softening modulus of 34000MPa. Plasticity and cracking were handled by the built-in capabilities of the finite element analysis program MSC Marc and the Tresca yield criterion was used. As reinforcement is considered to have stiffness only in its longitudinal direction, two materials were created to simulate the B500c steel. Both of them were considered orthotropic and had a Young's modulus of 200000 MPa only in one direction. Thus, a steel material with stiffness along the 1st local axes of the shell element was created (B500c-*x*) and another one with stiffness only parallel to the 2nd local axis of the shell (B500c-*y*). Both materials had a bilinear constitutive law with a yield stress of 435 MPa. The Von Mises criterion was used and no strain limitations applied. Table 5.1 summarizes the properties of the materials used.

	Behavior	E (MPa)	F_c (MPa)	F_t (MPa)
Concrete C60/75	Isotropic Elastic-perfectly plastic	34000	40	2 Cracking with softening modulus 34000 MPa
Steel B500c	Orthotropic Elastic-perfectly plastic	200000	435	435

Table 5.1 Material Properties for the Analysis

The geometry of the shell under study was based on the geometry of the 20mm thick shell case and is shown in Figure 5.1 below. As mentioned before its reinforcing mesh layer is simulated as an equivalent layer of B500c steel. Table 5.2 and Table 5.3 summarize the calculations performed in order to simulate the ferrocement shell and the composition of the shell element used to model the shell. A graphical representation of the composite shell is shown in Figure 5.2. The shell was 78.125mm wide and was subjected to four point bending with a zone of constant moment equal to 468.75mm.

Institutional Repository - Library & Information Centre - University of Thessaly
20/05/2024 20:20:43 EEST - 3.139.81.117

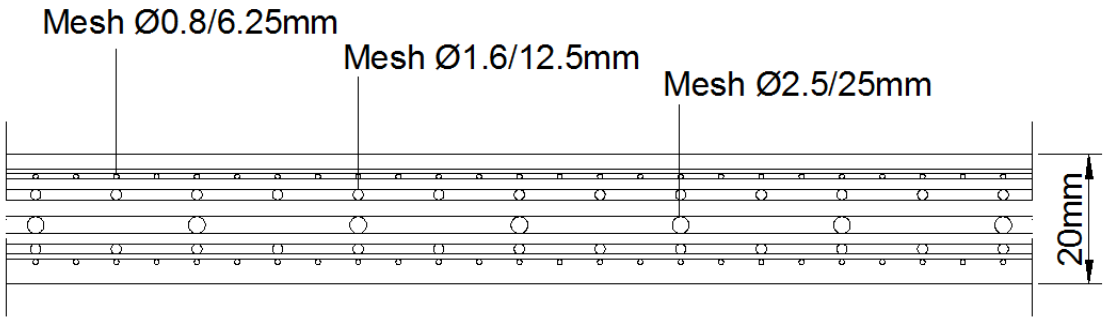

Figure 5.1 Cross Section of the Shell

	As per wire ($\pi D^2/4$) (mm^2)	Number of wires per meter per layer (1000/spacing)	As of one layer in each direction (mm^2/m)	Effective thickness of layer in Marc (mm)
Mesh 1	0.50265482	160	80.4247712	0.0804247712
Mesh 2	2.01062	80	160.8496	0.1608496
Mesh 3	4.9087385	40	196.34954	0.19634954

Table 5.2 Preliminary calculations for the composite shall model.

Composition of layered composite material (top to bottom)			
Layer ID	Material	Thickness (mm)	notes
1-2	C60/75	1.530	Cover
3	B500c – y	0.080	Mesh1
4	C60/75	0.720	Concrete between layers
5	B500c – x	0.080	Mesh1
6	C60/75	1.079	Concrete between layers
7	B500c – y	0.161	Mesh 2
8	C60/75	1.439	Concrete between layers
9	B500c – x	0.161	Mesh 2
10	C60/75	1.871	Concrete between layers
11	B500c – y	0.196	Mesh 3
12	C60/75	2.304	Concrete between layers
13	B500c – x	0.196	Mesh 3
14	C60/75	1.871	Concrete between layers
15	B500c – y	0.161	Mesh 2
16	C60/75	1.439	Concrete between layers
17	B500c – x	0.161	Mesh 2
18	C60/75	1.079	Concrete between layers
19	B500c – y	0.080	Mesh 1
20	C60/75	0.720	Concrete between layers
21	B500c – x	0.080	Mesh1
22-23	C60/75	1.530	Concrete between layers

Table 5.3 Composition of the composite shell.

Institutional Repository - Library & Information Centre - University of Thessaly
20/05/2024 20:20:43 EEST - 3.139.81.117

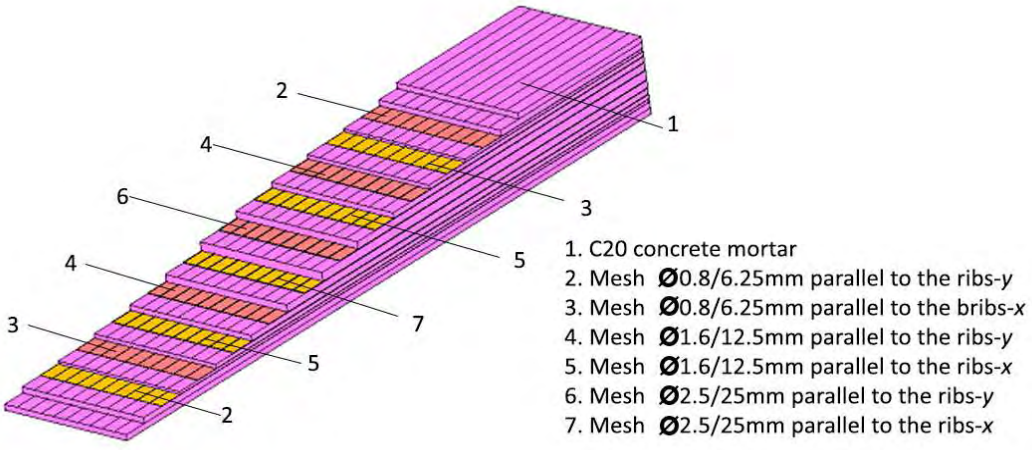

Figure 5.2 Composite Shell Element Simulating the Shell

5.2 Results for Pure Bending

The bending resistance (positive – top of the shell under compression) calculated by direct integration of the cross section by SAP 2000 15 is 1.85 kNm. Because SAP does not calculate the center of mass of the section but performs all the calculation using the center of the concrete cross section, all forces in Marc where applied at the center of the shell so that the result can be compared. The numerical simulation performed by MSC Marc calculates a bending resistance of 1.95 kNm (5.4% difference). The negative bending resistance according to Sap is -2.29 kNm while Marc calculates -2.35 kNm (3% difference).

5.3 M-N Interaction and Conclusions

As mentioned during the analysis of the rib, it is important for the model to simulate the behavior of the structure not only under pure bending but also under the presence of axial compressive loads. Finally, the M-N interaction curves are calculated by direct integration of the cross section (Sap) and according to the composite shell model in Marc. Because SAP does not calculate the center of mass of the section but performs all the calculation using the center of the concrete cross section, all forces in Marc were applied at the center of the shell so that the result are comparable. The comparison (Table 5.4 and Figure 5.3) shows a deviation of the results, especially in high compressive loads. The main reason for the deviation is that in Marc, as the model enters the plastic region, compressive stresses in the transverse direction appear in the concrete layers causing the stresses in the main direction to increase. As the compressive axial load increases a larger part of the section is under compression and thus the error increases. However, this error is considered insignificant and will be eliminated in the actual model where stresses will exist in both directions. Thus, the simulation method is considered accurate enough.

Institutional Repository - Library & Information Centre - University of Thessaly
20/05/2024 20:20:43 EEST - 3.139.81.117

Axial Load KN/m	Bending Moment – Marc 2011 KNm	Bending Moment – SAP 2000 KNm
0	1.95	1.85
180	2.81	2.673
360	3.13	2.97
540	3.21	3.00
720	2.674	2.46
900	2.04	1.56
900	-1.66	-1.13
720	-2.57	-2.135
540	-3.1	-2.83
360	-3.47	-3.06
180	-3.04	-2.90
0	-2.35	-2.29

Table 5.4 M-N interaction.

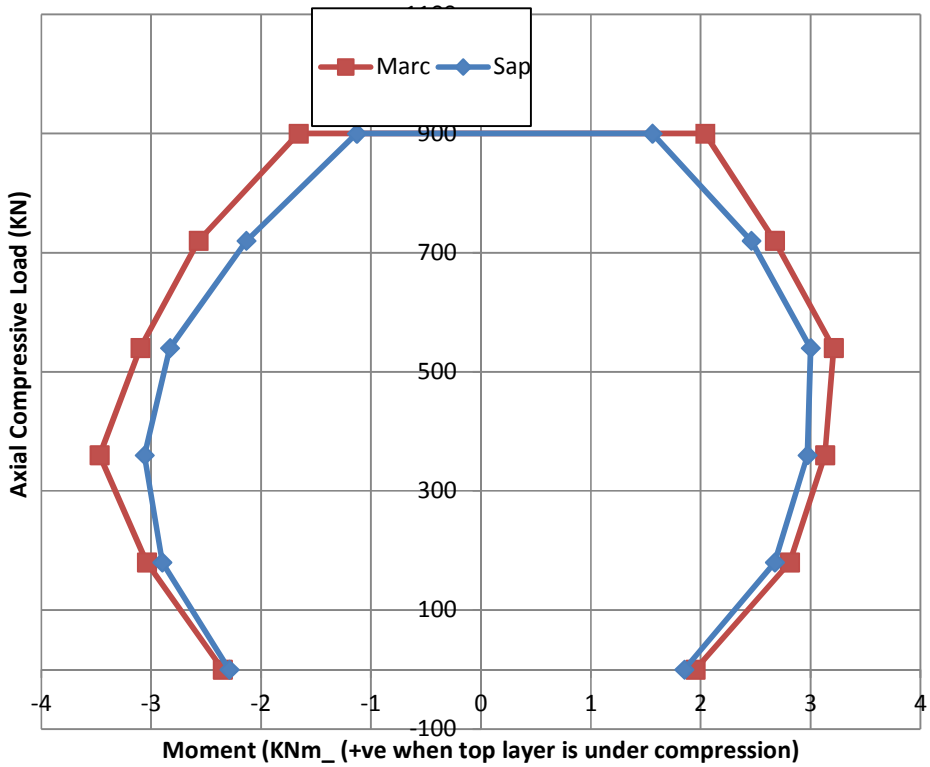

Figure 5.3 M-N Interaction curve under compression.

Institutional Repository - Library & Information Centre - University of Thessaly
20/05/2024 20:20:43 EEST - 3.139.81.117

6 Geometrical and Material Nonlinear Analysis

As mentioned in the previous chapters, due to the lack of detailed analysis and design recommendations in the Eurocode parts related to the design of concrete or cementitious structures (Eurocode 2 (2005)), methodologies followed in the design of steel structures are applied here (Eurocode 3 (2007)).

The approaches available to the designer are the hand calculation, the semi-analytical calculation (mixed hand and computer) and the numerical calculation. As the European design recommendations mention (ECCS TC8 TWG 8.4 (2008)), when numerical analysis is performed a part or even all the hand calculation can be replaced by the numerical results. Eurocode provides two alternative FE analysis approaches. The design by global numerical analysis using material nonlinear analysis (MNA) and linear buckling analysis (LBA) analyses and the design by global numerical analysis using GMNIA. The structure is studied following the fully numerical calculation procedure by global numerical analysis using GMNIA analysis (GMNIA: Geometrical and Material Nonlinear analysis of the Imperfect shell).

In order to specify the elastic-plastic buckling resistance, EN1993-1-6 (2007) provides the following criteria, which are shown in Figure 6.1:

Criterion C1: The maximum load factor on the load-deformation-curve (limit load);
Criterion C2: The bifurcation load factor, where this occurs during the loading path before reaching the limit point of the load-deformation-curve;
Criterion C3: The largest tolerable deformation, where this occurs during the loading path before reaching a bifurcation load or a limit load.
Criterion C4 is a conservative estimation by a geometrically nonlinear analysis of the imperfect elastic shell

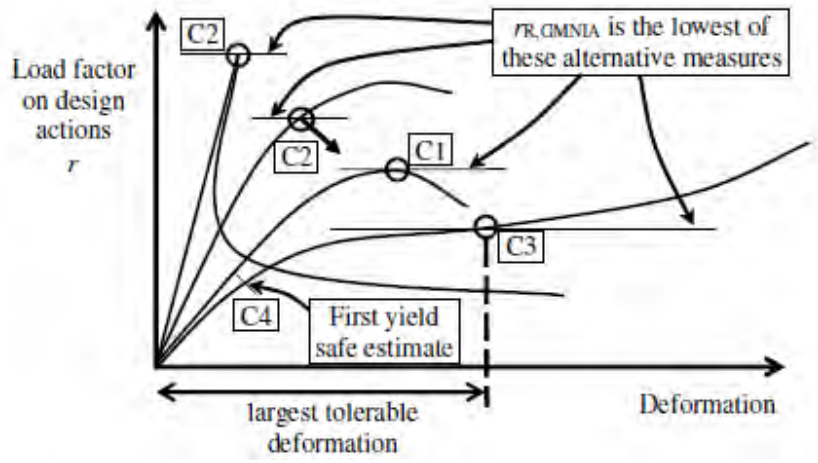

Figure 6.1 The criteria of EN1993-1-6 to determine the elastic-plastic buckling resistance. EN1993-1-6 (2007).

Institutional Repository - Library & Information Centre - University of Thessaly
20/05/2024 20:20:43 EEST - 3.139.81.117

6.1 20mm Thick Model Nonlinear Buckle Analysis Along the *x* Axis

The preliminary modal buckle analysis along the heavily stiffened direction showed that the shell has a relatively high elastic buckling load due to the global buckling mode in the y direction. A set of nonlinear large strain analyses with initial imperfection equal to 20mm confirmed that the shell buckles in a global mode along the y-axis. However, as the local buckling parallel to the x axis results in significantly lower resistance, only the buckling along the critical x direction is further investigated.

During the validation of the simulation of the ribs and shell, reinforcing steel was considered to be anisotropic with stiffness only in the direction of the reinforcement rods equal to 200000 MPa. Its elastic-plastic constitutive law was considered bilinear with a yield stress of 435 MPa and no hardening (Fig. 8a), and the Von Mises yield criterions was used. As far as the concrete mortar is concerned, it was considered isotropic with a Young's modulus of 34000 MPa. The mortar had an ultimate compressive strength of 40 MPa, while cracking was taken under consideration by enabling the damage effect capabilities of MSC Marc. The ultimate tensile stress was considered to be 2 MPa and the softening modulus was equal to 34000 MPa (Fig. 8b). The Tresca yield stress criterion was used.

The models were solved by an iterative full Newton-Raphson procedure and the convergence criterion was based on residual forces. The inverse power sweep method was used for the buckle solution, from which the shape of the initial imperfections was determined. The nonlinear analysis solution was based on the large strain theory and the full layer integration method was used for the composite layered shells.

6.1.1 Preliminary Nonlinear Analysis

When both geometric and material nonlinearities are considered, the problem becomes highly complex. Therefore, taking advantage of the symmetry or anti-symmetry of the dominant buckling mode that develops, initially, only the central rib including half span at each side (2.5x5m) was modeled and analyzed. In order to eliminate, as possible, the instabilities of the model, internal restraints were imposed in each plane of symmetry and anti-symmetry. In more detail, these restrains impose the deflection in each plane of anti-symmetry and the rotation about the y axis in each plane of symmetry to be equal to zero as shown in Figure 6.2. In the sequel, these models will be referred to as "restrained" ones. As the model is forced to buckle according to the mode discussed in Section 3.3.1, this set of analyses provides an upper bound for the buckling load, corresponding to the simultaneous buckle of all spans. A "restrained" 2.5x5 m model with initial imperfection according to the local buckling shape of maximum magnitude equal to 3mm was created and analyzed.

Institutional Repository - Library & Information Centre - University of Thessaly
20/05/2024 20:20:43 EEST - 3.139.81.117

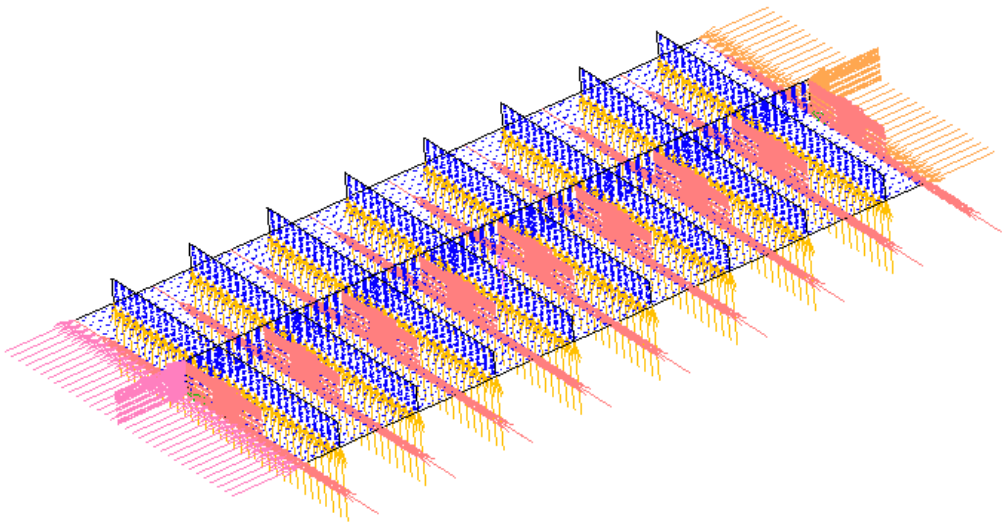

Figure 6.2 Boundary Conditions of the 2.5 x 5 m Model

The results of the analysis showed that the simultaneous buckling of all spans, shown in Figure 6.3, corresponds to a buckle load of 753 kN/m. Figure 6.4 shows the axial load – compressive strain curve of the ribbed shell. It should be noted that the ultimate compressive strength of the stiffened shell according to a material nonlinear analysis is equal to 1509 kN/m. Thus, this buckling load corresponds to a reduction factor equal to 0.499.

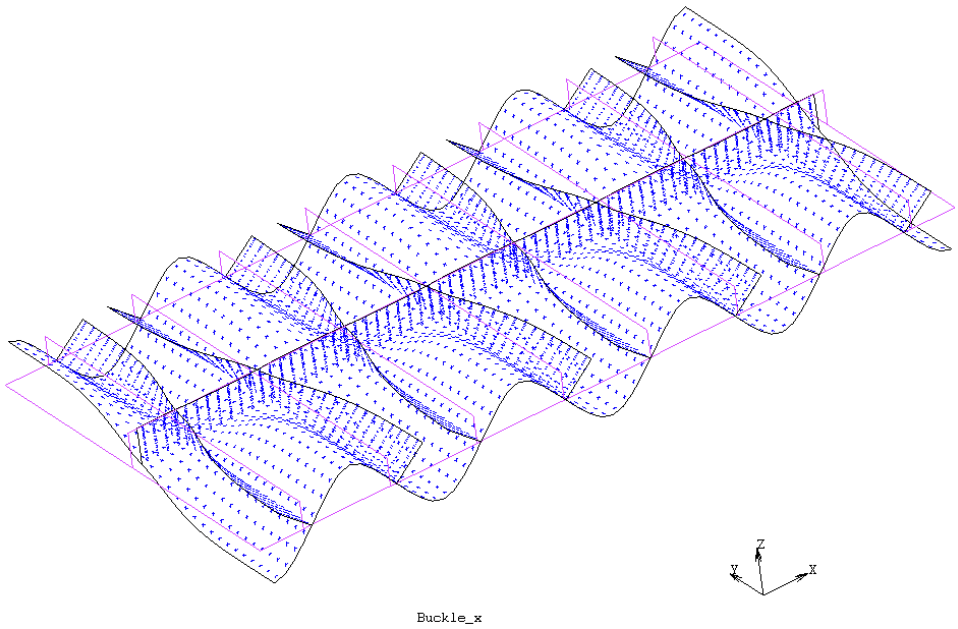

Figure 6.3 Deformed and Original shape after the buckling of the structure

Institutional Repository - Library & Information Centre - University of Thessaly
20/05/2024 20:20:43 EEST - 3.139.81.117

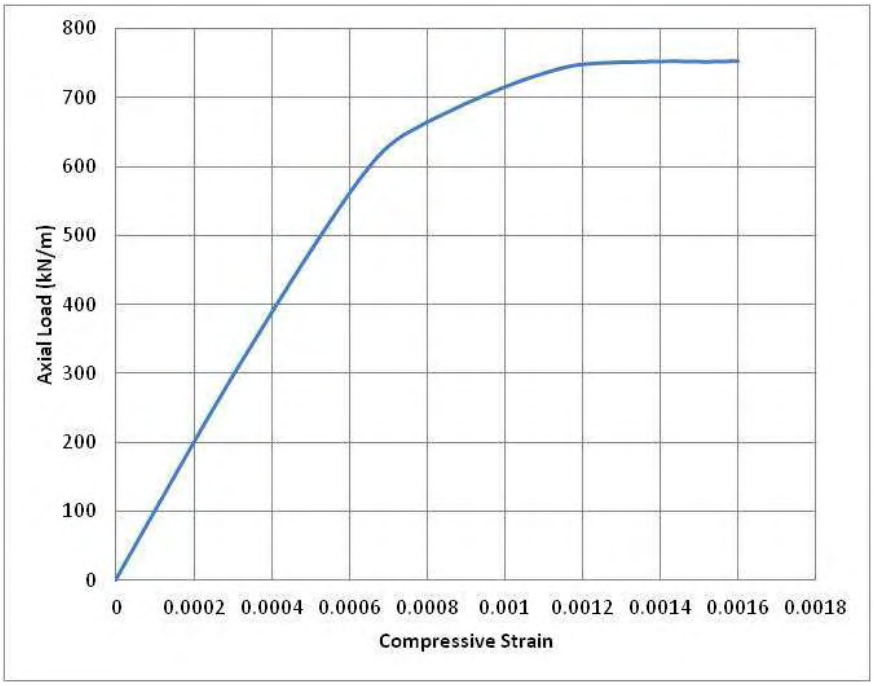

Figure 6.4 Axial Load - Compressive Strain Curve

Although the 2.5x5 m model can accurately calculate the ultimate plastic buckling load of the structure, it cannot be used to investigate the interaction of the loads along the two axis. In order to study the interaction of the axial loads in the perpendicular directions, a 5x5m model must be used with appropriate boundary conditions (symmetry along the *y* edges and antisymmetry along the *x* edges). Because the plane of symmetry along the *x* axis cuts the outer rib-*x* in half and in order to simulate accurately the nonlinear behavior, an equivalent rib-*x* was created with an ultimate bending resistance in and out of plane, and stiffness half of that of the actual whole rib. This was achieved by reducing the Young's modulus and yield stress of the materials used in those ribs to half of the actual material properties. The 2.5x5 m model was used for reference and three other models, one with internal restrains corresponding to the desired buckle mode, another one without internal restrains and, finally, one with only boundary conditions of symmetry along the *y* edges were formulated and analysed. The results are shown in Figure 6.5 to Figure 6.8. Figure 6.5 compares the two "restrained" models and demonstrates that the 5x5m equivalent beam model accurately simulates the behavior of the shell and can be used to further investigated the interaction of the axial loads. Figure 6.6 presents a comparison between the three 5x5 m models with different boundary conditions. Both unrestrained models have the same pre-buckle behavior with the restrained one and lose stability under the same axial load of 681 kN per meter of stiffened shell. This phenomenon is caused by the small variations of the imperfection magnitude between spans, as well as by the nonlinearity of the material. As certain spans fail earlier than others, the surrounding areas release their stored strain energy, pushing them further in the plastic region (Figure 6.7 and Figure 6.8).

Institutional Repository - Library & Information Centre - University of Thessaly
20/05/2024 20:20:43 EEST - 3.139.81.117

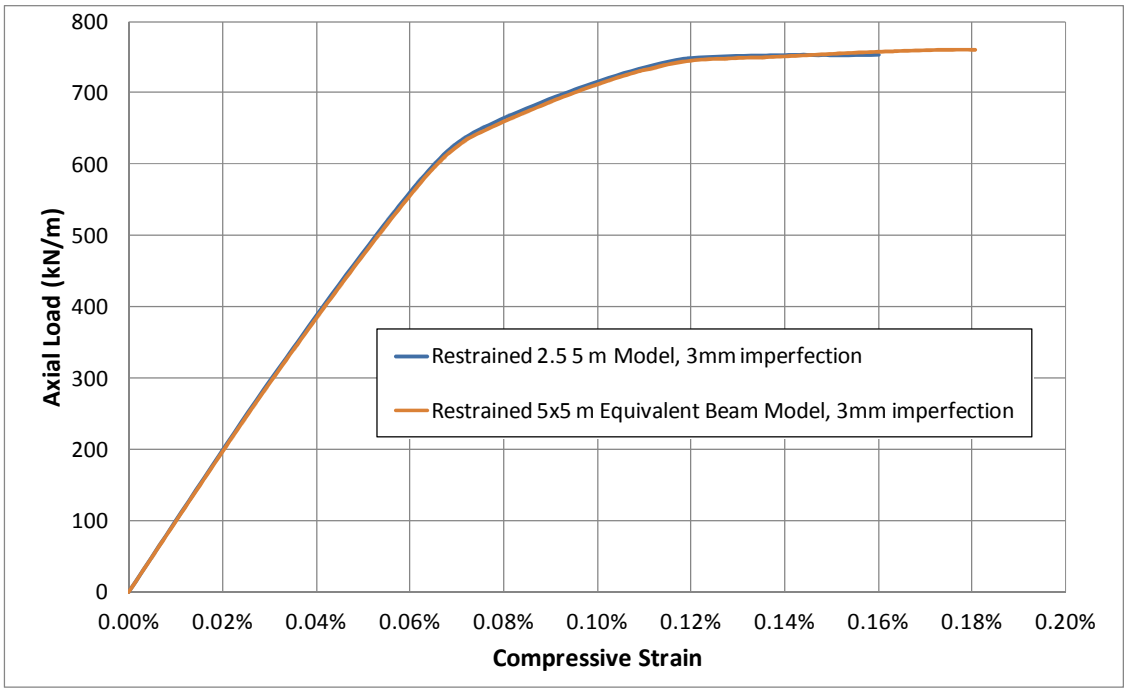

Figure 6.5Axial Load - Compressive Strain Curve Comparison of the Equivalent beam model to the 2.5x5m model

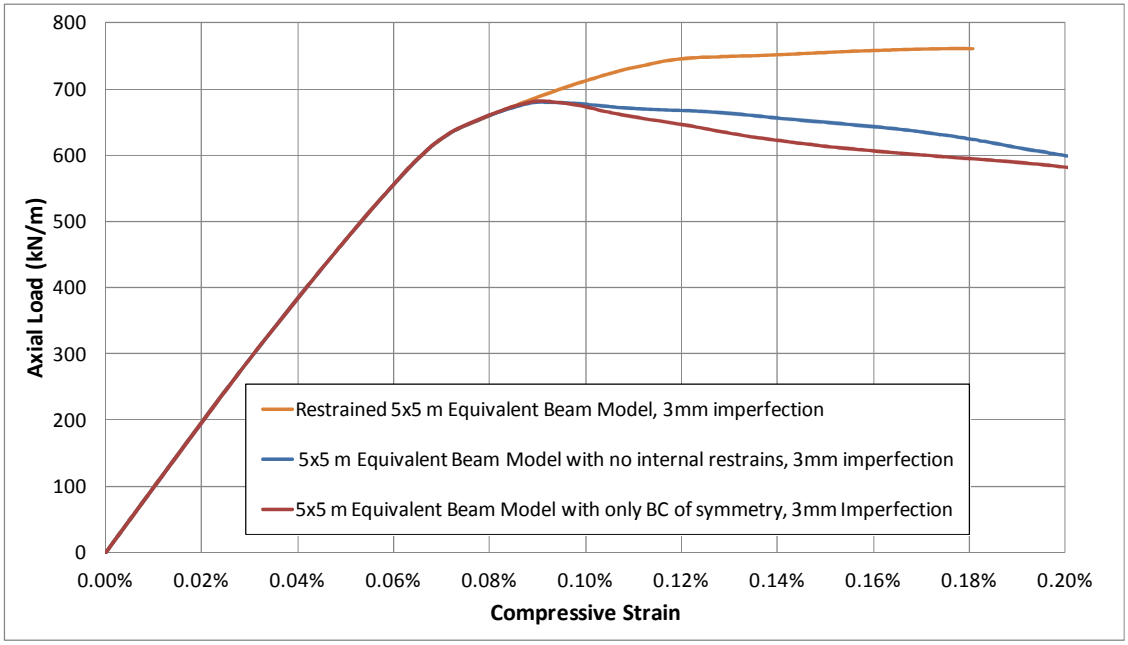

Figure 6.6 Axial Load - Compressive Strain Curve Comparison of the Equivalent beam model with different BCs

Institutional Repository - Library & Information Centre - University of Thessaly
20/05/2024 20:20:43 EEST - 3.139.81.117

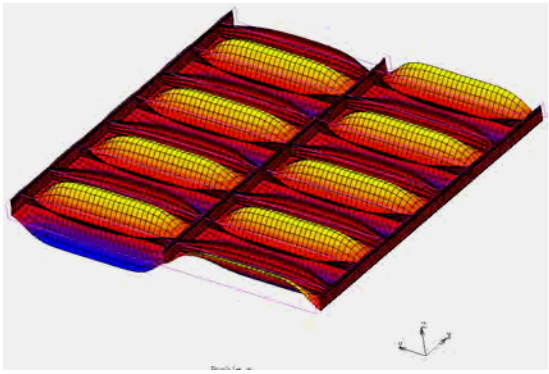

Figure 6.7 Failure of the restrained model

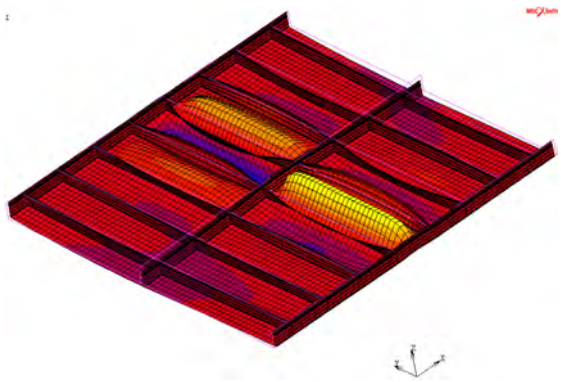

Figure 6.8 Failure of the unrestrained model. Localization of the failure

The results of the above analysis show that the equivalent 5x5m model accurately simulates the behavior of the stiffened shell. Both the 2.5x5m model, in which the outer rib-*x* are not simulated and thus have no effect on the buckling resistance, and the 5x5m models with an equivalent outer rib-*x* , formulated to take into account that only half the rib-*x* belongs to the simulated area, have identical behavior. Also, the analysis of the above five models shows that the buckling along the *x* axis is very sensitive to localization. Both the restrained models demonstrate similar behavior with simultaneous buckling of all spans. On the other hand, when the internal restraints are removed, caused by the small variation of the imperfection between spans, the shell fails at a lower axial load by the buckling of certain spans. Keeping in mind that an actual structure will not have a shape with the same amplitude of imperfections in all spans the unrestrained model seems to be closer to reality. The load of 760 kN/m is considered to be the upper bound of the buckling resistance of the shell and thus cannot be used in the design of such structures. Both “unrestrained” models have the same pre-buckle behavior with the restrained ones and lose stability under the same axial load of 681 kN/m, even though they have different boundary conditions on the longitudinal edges. Thus it seems that this load is an ultimate load, safe for design purposes.

6.1.2 Impact of the Imperfections

After determining the behavior of the shell, the impact of the imperfections on the buckling load was studied. In addition to the 2.5 x 5 m model with 3mm imperfection, three more models where analysed. Figure 6.9 shows the comparison of the axial load vs. compressive strain curves of the four models. Although as the imperfections become greater the model loses initial stiffness, all models buckle under the same axial load. Next, as we are interested in determining the buckling resistance of an unrestrained model so that the possibility of localization of the failure is taken into account, three 5x5 m models without internal restrains were formulated and analysed. As expected, the unrestrained models have exactly the same prebuckle behavior and a lower ultimate load capacity, due to localization of the failure to certain spans. At a low axial load, the restrained and unrestrained models have the same behavior, with all spans having almost the same deflection. After a specific point, certain spans in the unrestrained models fail and the structure loses stability, while in the restrained models, as mentioned earlier, all spans fail and lose stability at the same time. The buckling load for different magnitude of initial

Institutional Repository - Library & Information Centre - University of Thessaly
20/05/2024 20:20:43 EEST - 3.139.81.117

imperfection is also about the same as with the restrained models (679 , 697 and 709 kN/m for 3, 4 and 5 mm maximum magnitude of initial imperfection respectively). Thus, we can say that the magnitude of the initial imperfection has very little effect on the ultimate strength of the stiffened shell. Figure 6.10 provides a comparison between all analyses. As the imperfections become greater, the buckling load slightly increases, something that is not surely expected. This is likely caused by the fact that the buckling behavior of stiffened shells can be very sensitive to the used imperfections and small differences between the imperfections used in the various areas can cause differences in the numerically calculated load bearing capacity of the structure. Even in the formulation of a numerical model, such cases cannot be eliminated and are also affected by the intense material non-linearity. This phenomenon has been also observed in experimental data. However, it is usually neglected during the design of such shells and a lower bound of the buckling load should be used on the grounds that this increase is usually followed by a more violent loss of strength.

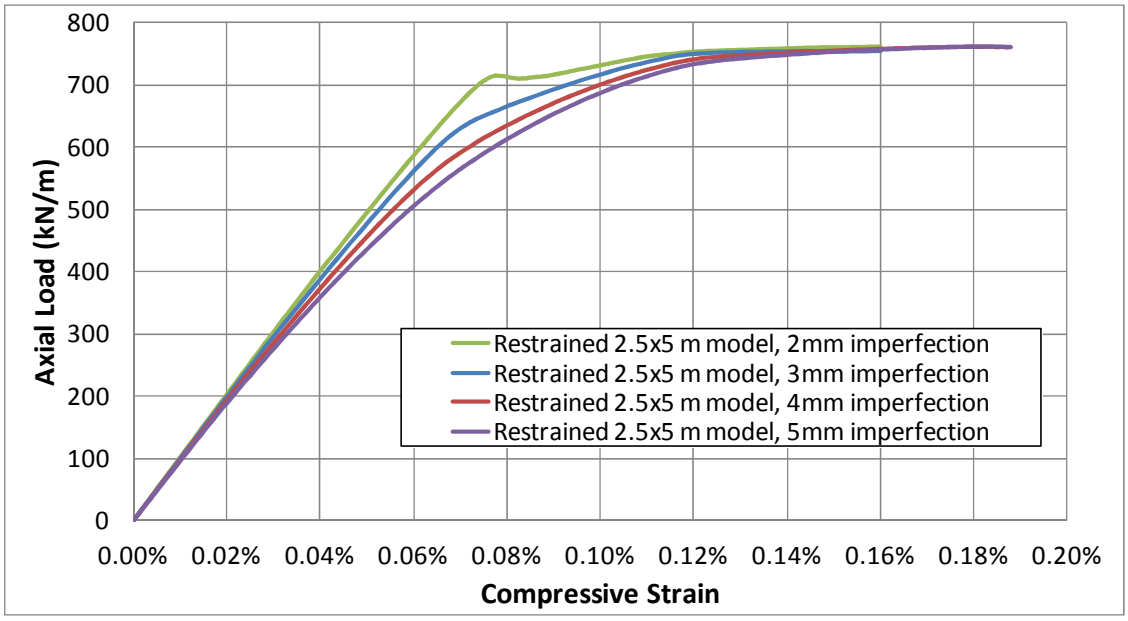

Figure 6.9 Axial Load - Compressive Strain Curve Comparison for Different Initial Imperfections

Institutional Repository - Library & Information Centre - University of Thessaly
20/05/2024 20:20:43 EEST - 3.139.81.117

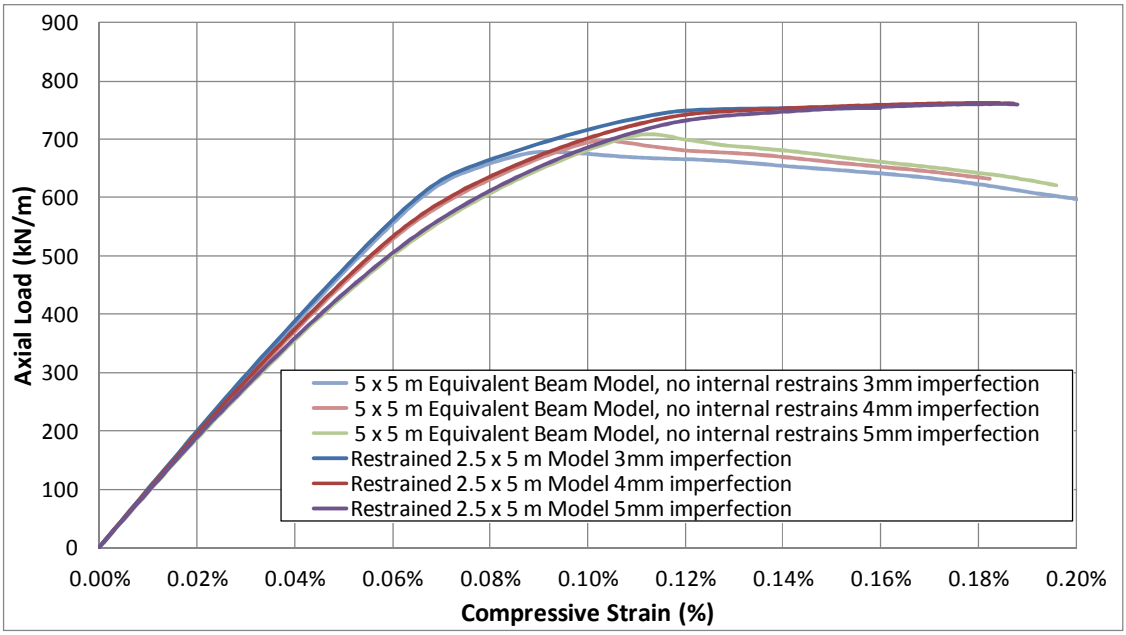

Figure 6.10 Summary of Buckling Behavior of the Stiffened Shell. Buckle Along the X Axis

6.1.3 The influence of combined bi-axial compression

Finally, the influence of the axial load in the *y* direction (N_y) is investigated. The models used in this set of analysis were equipped with internal restrains. Axial loads up to 600 kN/m were applied in the *y* direction. Figure 6.11 demonstrates the results for axial load in the *y* direction equal to 200, 400 and 600 kN/m, while Figure 6.12 presents the interaction curve obtained by this set of analyses, which is in agreement with interaction curves found in the literature (Byklum et al (2004)) for similar problems. The influence of bi-axial compression seems to be insignificant for the structure at hand. Such behavior is expected from a structures non-slender in the *y* direction, with small aspect ratio of the spans and high length-to-shell thickness ratio.

Institutional Repository - Library & Information Centre - University of Thessaly
20/05/2024 20:20:43 EEST - 3.139.81.117

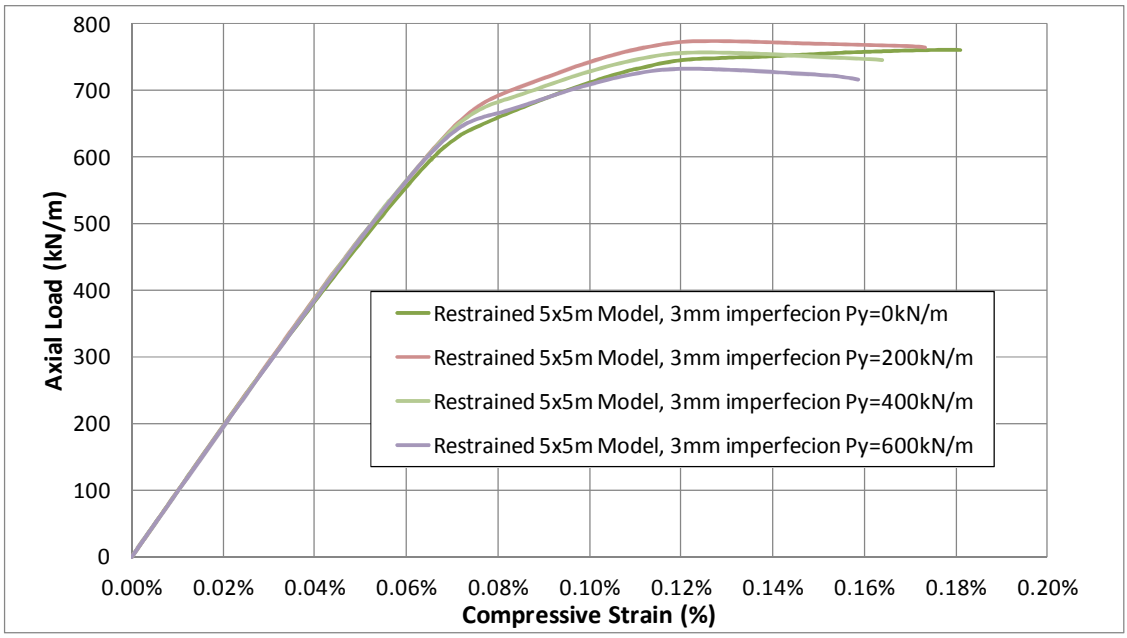

Figure 6.11 influence of combined bi-axial compression

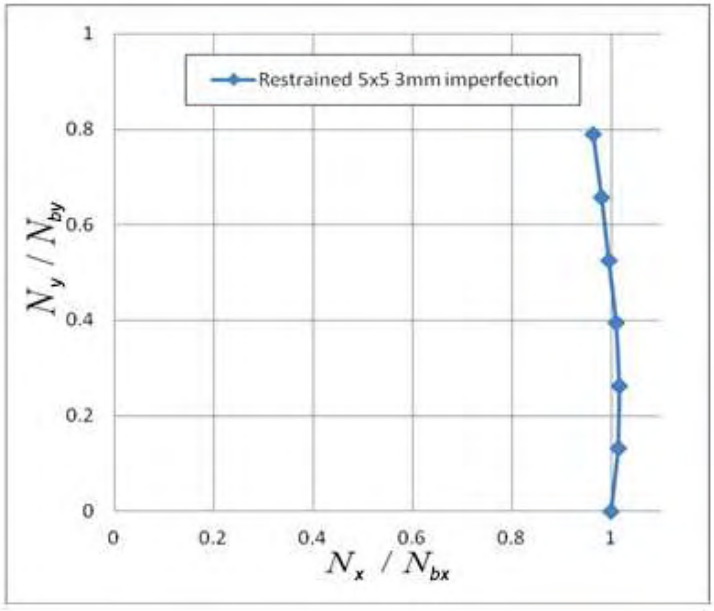

Figure 6.12 Interaction Curve

Institutional Repository - Library & Information Centre - University of Thessaly
20/05/2024 20:20:43 EEST - 3.139.81.117

7 Conclusions

An investigation of the buckling behavior of a stiffened ferrocement shell was presented in this study. The fully numerical approach of EC-3 part 1.6 was followed. The analysis procedure consists of:

- A linear buckling analysis (LBA). This set of analyses is used to determine the dominant buckling modes, the shape of the initial imperfections used in the geometrical and material nonlinear analysis and, finally, the periodic boundary conditions that can be used to reduce the size of the model.
- A geometrical and material nonlinear analysis of the imperfect shell (GMNIA) to determine the plastic buckling resistance of the structure.

The LBA showed that two buckling modes are critical. The global buckling mode between supports with half-wave length of 5m and the local buckling one of the subpanels between ribs. The main factor that affects the buckling shape is the relative stiffness ratio of the stiffeners to the shell γ. The other important factor is the applied boundary conditions that also control the interaction between modes.

In order to verify that the nonlinear behavior of ferrocement is accurately taken into account a simulation method by the use of composite layered shells was investigated. The comparison of the results obtained by the numerical analysis to the ones calculated by direct integration of the cross section demonstrate that this simulation method is capable of simulating very well both the in plane and out of plane behavior of the structural elements. The numerical results were adequately accurate for various strain limitations and for both pure bending and bending under the presence of axial loads.

Plasticity, as the results of the GMNIA show, causes a drop of the buckling resistance by 40%. It is quite obvious that an analytical approach is impossible to be applied as the geometrical and material nonlinearities, together with the effect of the stiffeners, cause high complexity. The numerical approach of the EC-3 part 1.6 seems to be appropriate for the design and analysis of such structures.

As far as the impact of the imperfections is concerned, they seem to have little influence on the ultimate load capacity, however, local buckling is very sensitive to localization and thus small deviation of the magnitude of the initial imperfections between subpanels may cause the structure to fail before reaching its maximum resistance.

Finally, the influence of bi-axial compression seems not to be dominant for the structure at hand. Based on existing research on similar problems (Ventsel and Krauthammer (2001)), such behavior is expected for structures which are non-slender in one of the two loading directions, with small aspect ratio of the span edges and with high length-to shell thickness ratios.

Institutional Repository - Library & Information Centre - University of Thessaly
20/05/2024 20:20:43 EEST - 3.139.81.117

8 References

ACI Committee 549 (Reapproved 1999) , *ACI 549.1R-93 Guide for the Design, Construction, and Repair of Ferrocement.*

Amdahl, J. (2009), *TMR4205 Buckling and Ultimate Strength of Marine Structures Chapter 3: Buckling of Stiffened Shells*, MTS-2009.05.18.

Computers and Structures, Inc. (2011), *"SAP2000 analysis reference manual"*, Computers and Structures, Inc. Berkeley, California, USA.

EN1992-1-2 (2005), *Eurocode 2: Design of concrete structures - Part 1-1: General rules and rules for buildings*, Brussels.

EN1993-1-6 (2007), *Eurocode 3: Design of steel structures Part 1-6 : Strength and Stability of Shell Structures*, Brussels.

ECCS TC8 TWG 8.4 (2008), *Shells, Buckling of steel shells European design recommendations*, ECCS, 5th Edition.

Amdahl, J. (2009), *TMR4205 Buckling and Ultimate Strength of Marine Structures Chapter 3: Buckling of Stiffened Shells*, MTS-2009.05.18.

Bergan, P.G., Holand, I. (1979), "Nonlinear Finite Element Analysis Of Concrete Structures, J Computer Methods in Applied Mechanics and Engineering", **17-18**, 443-467.

Byklum,E., Steen, E., Amdahl, J. (2004), "A semi-analytical model for global buckling and postbuckling analysis of stiffened panels", *Thin-Walled Structures*, **42**, 701–717.

ECCS TC8 TWG 8.4 (2008), *Shells, Buckling of steel shells European design recommendations*, ECCS, 5th Edition.

Fujikubo, M., Harada, M., Yao, T., Khedmati, M.R., Yanagihara, D. (2006), "Estimation of ultimate strength of continuous stiffened panel under combined transverse thrust and lateral pressure Part 2: Continuous stiffened panel", *Marine Structures*, **18**, 411-427.

Khedmati, M.R., Zareei, M.R., Rigo, P. (2009), "Sensitivity analysis on the elastic buckling and ultimate strength of continuous stiffened aluminium shells under combined in-plane compression and lateral pressure", *Thin-Walled Structures*, **47**, 1232-1245.

Mittelstedt, C. (2007), "Closed-form analysis of the buckling loads of uniaxially loaded blade-stringer-stiffened composite shells considering periodic boundary conditions", *Thin-Walled Structures*, **45**, 371-382.

Mittelstedt, C. (2009), "Explicit local buckling analysis of stiffened composite shells accounting for periodic boundary conditions and stiffener–shell interaction", *Composite Structures*, **91**, 249-265.

MSC Software Corporation (2011), "*MSC Marc, Volume A: Theory and user information",* MSC Software Corporation, USA.

Naaman A. E., (2000), *Ferrocement and Laminated Cementitious Composites*, Techno Press 3000., Ann Arbor, Michigan, USA.

Paik, J.K., Kim, B.J., Seo, J.K. (2008), "Methods for ultimate limit state assessment of ships and ship-shaped offshore structures: Part II stiffened panels", *Ocean Engineering*, **35**, 271–280.

Paik, J.K., Seo, J.K. (2009), "Nonlinear finite element method models for ultimate strength analysis of steel stiffened-shell structures under combined biaxial compression and Lateral pressure actions—PartII: Stiffened panels", *Thin-Walled Structures*, **47**, 998-1007.

Stamatelos, D.G., Labeas, G.N., Tserpes, K.I. (2011), "Analytical calculation of local buckling and post-buckling behavior of isotropic and orthotropic stiffened panels", *Thin-Walled Structures*, **49**, 422-430.

Tvergaard V. (1973) , "Imperfection-Sensitivity of a wide integrally stiffened panel under compression", *Int. J. Solid Structures*, **9**, 117-192,

Institutional Repository - Library & Information Centre - University of Thessaly
20/05/2024 20:20:43 EEST - 3.139.81.117

Ueda, Y., Rashed, S.M.H., Paik J.K. (1995), “Buckling and ultimate strength in shells and stiffened panels under combined in plane biaxial and shearing forces”, *Marine Structures*, **8**., 1-36.

Ventsel E., Krauthammer, Th. (2001), Thin Shells and Shells Theory, Analysis, and Applications, Marcel Dekker INC., New York Basel.

Institutional Repository - Library & Information Centre - University of Thessaly
20/05/2024 20:20:43 EEST - 3.139.81.117

9 APPENDIX

Institutional Repository - Library & Information Centre - University of Thessaly
20/05/2024 20:20:43 EEST - 3.139.81.117

Marc Shell Element 75

(Reproduction of important parts as written in Marc 2011 Volume B: Element Library)

This is a four-node, thick-shell element with global displacements and rotations as degrees of freedom. Bilinear interpolation is used for the coordinates, displacements and the rotations. The membrane strains are obtained from the displacement field; the curvatures from the rotation field. The transverse shear strains are calculated at the middle of the edges and interpolated to the integration points. In this way, a very efficient and simple element is obtained which exhibits correct behavior in the limiting case of thin shells. The element can be used in curved shell analysis as well as in the analysis of complicated shell structures. For the latter case, the element is easy to use since connections between intersecting shells can be modeled without tying.

Due to its simple formulation when compared to the standard higher order shell elements, it is less expensive and, therefore, very attractive in nonlinear analysis. The element is not very sensitive to distortion, particularly if the corner nodes lie in the same plane. All constitutive relations can be used with this element.

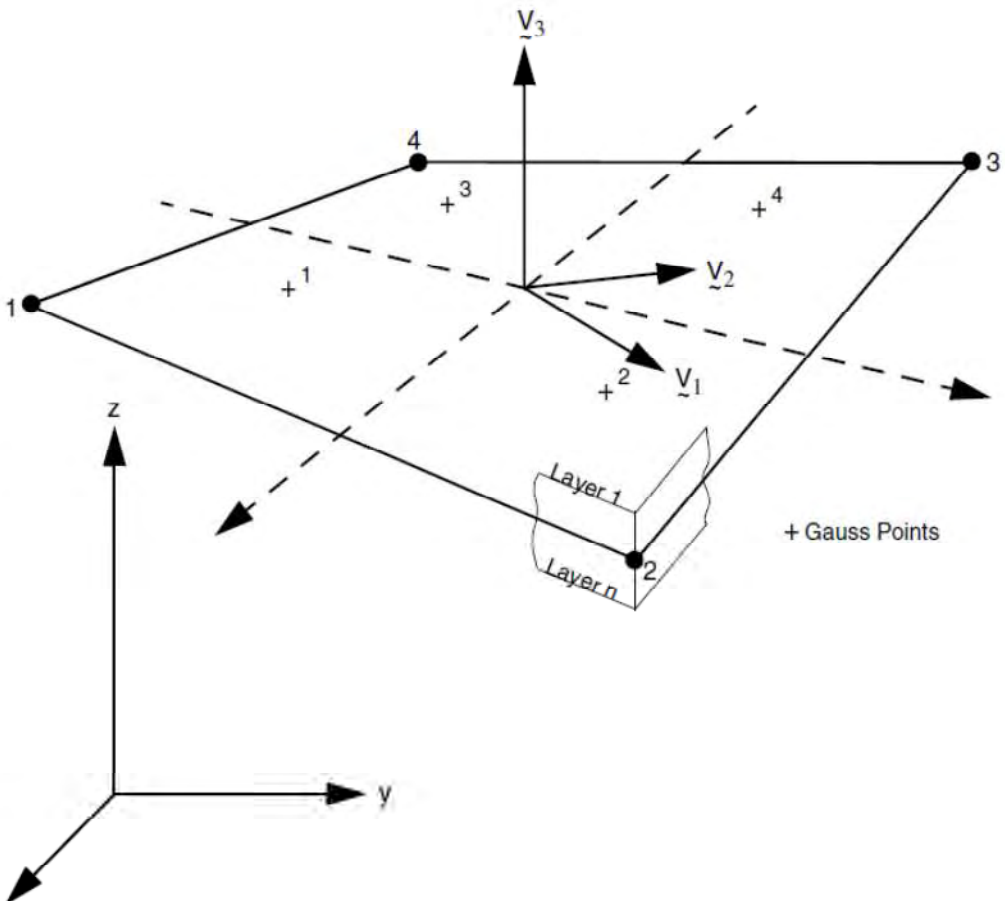

Institutional Repository - Library & Information Centre - University of Thessaly
20/05/2024 20:20:43 EEST - 3.139.81.117

Marc Solid Element 7

(Reproduction of important parts as written in Marc 2011 Volume B: Element Library)

Element type 7 is an eight-node, isoparametric, arbitrary hexahedral. As this element uses trilinear interpolation functions, the strains tend to be constant throughout the element. This results in a poor representation of shear behavior. The shear (or bending) characteristics can be improved by using alternative interpolation functions. This assumed strain procedure is flagged through the GEOMETRY option. For the assumed strain formulation, the interpolation functions are modified to improve the bending characteristics of the element.

In general, you need more of these lower-order elements than the higher-order elements such as types 21 or 57. Hence, use a fine mesh.

This element is preferred over higher-order elements when used in a contact analysis.

The stiffness of this element is formed using eight-point Gaussian integration.

This element can be used for all constitutive relations.

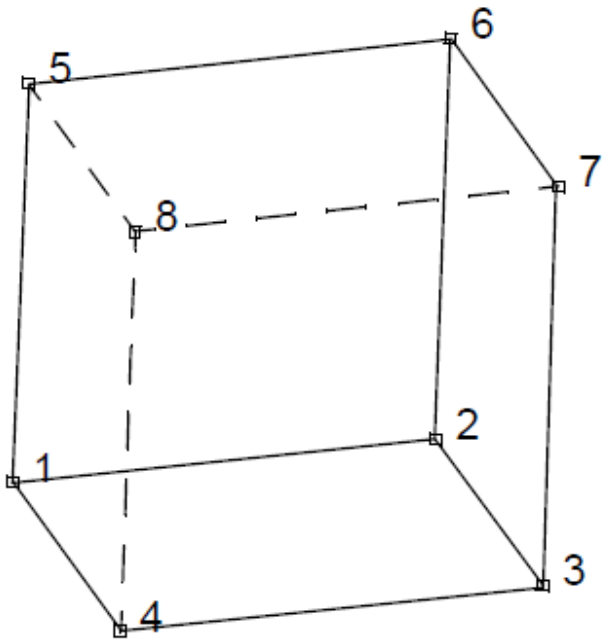

Three global degrees of freedom u, v, and w per node.

Institutional Repository - Library & Information Centre - University of Thessaly
20/05/2024 20:20:43 EEST - 3.139.81.117

Marc Beam Element 98

(Reproduction of important parts as written in Marc 2011 Volume B: Element Library)

This is a straight beam in space which includes transverse shear effects with linear elastic material response as its standard material response, but it also allows nonlinear elastic and inelastic material response. Large curvature changes are neglected in the large displacement formulation. Linear interpolation is used for the axial and the transverse displacements as well as for the rotations.

This element can be used to model linear or nonlinear elastic response by direct entry of the cross-section properties. Nonlinear elastic response can be modeled when the material behavior is given in the UBEAM user subroutine (see *Marc Volume D: User Subroutines and Special Routines*). This element can also be used to model inelastic and nonlinear elastic material response when employing numerical integration over the cross section. Standard cross

sections and arbitrary cross sections are entered through the BEAM SECT parameter if the element is to use numerical cross-section integration. Inelastic material response includes plasticity models, creep models, and shape memory models, but excludes powder models, soil models, concrete cracking models, and rigid plastic flow models. Elastic material response includes isotropic elasticity models and NLELAST nonlinear elasticity models, but excludes finite

strain elasticity models like Mooney, Ogden, Gent, Arruda-Boyce, Foam, and orthotropic or anisotropic elasticity models. With numerical integration, the HYPELA2 user subroutine can be used to model arbitrary nonlinear material response (see Note). Arbitrary sections can be used in a pre-integrated way. In that case, only linear elasticity and nonlinear elasticity through the UBEAM user subroutine are available.

Geometric Basis

The element uses a local (x,y,z) set for section properties. Local x and y are the principal axes of the cross section.

Local z is along the beam axis. Using fields 4, 5, and 6 in the GEOMETRY option, a vector in the plane of the local x-axis and the beam axis must be specified. If no vector is defined here, the local coordinate system can alternatively be defined by the global (x,y,z) coordinates at the two nodes and by (x1, x2, x3), a point in space which locates the local x-axis of the cross section. This axis lies in the plane defined by the beam nodes and this point, pointing from the beam

axis toward the point. The local x-axis is normal to the beam axis. The local z-axis goes from node 1 to node 2, and the local y-axis forms a right-handed set with local x and z.

Numerical Integration

The element uses a one-point integration scheme. This point is at the midspan location. This leads to an exact calculation for bending and a reduced integration scheme for shear. The mass matrix of this element is formed using three-point Gaussian integration.

Degrees of Freedom

1 = ux = global Cartesian x-direction displacement
2 = uy = global Cartesian y-direction displacement
3 = uz = global Cartesian z-direction displacement
4 = θx = rotation about global x-direction
5 = θy = rotation about global y-direction
6 = θz = rotation about global z-direction

Institutional Repository - Library & Information Centre - University of Thessaly
20/05/2024 20:20:43 EEST - 3.139.81.117

RBE2

(Reproduction of important parts as written in Marc 2011 Volume A: Theory and User Information)

The nonlinear relation of an RBE2 can be expressed as follows:

$x_t = R(\theta_r)(x_t - x_r)$

where x_t is the coordinate of the tied node, x_r is the coordinate of the reference node, and θ_r is the rotation matrix of the retained node. The linearized relation between the incremental displacement of a tied node to a retained node and its correction term is expressed as follows:

$$\Delta u_t^i = S\Delta u_r^i + C_{non}$$

where the tying matrix *S* is derived from the linearized rigid body relation. For linear analysis C_{non}, is zero. For large displacement analysis, $S\Delta u_r^i$ may not match the nonlinear constraint exactly. Therefore, an error vector, , is required to meet the constraint. It is defined as the difference between the expected coordinates (x_{te}), using the rigid body kinematics, and the current coordinates (x_t) of the tied node.

$$x_{te}^{n+i} = x_r^n R(\theta_r^{n+i})(x_t^0 - x_r^0)$$
$$C_{non} = x_{te}^{n+i} - x_t^{n+i}$$

Where *i* is increment number, is iteration number, and zero is the original value

When the rotation is finite, then the coordinate system attached to the tied node will be co-rotated according to the rotation of the retained node. The degrees of freedom of the tied node will be assigned with this co-rotated system.

Institutional Repository - Library & Information Centre - University of Thessaly
20/05/2024 20:20:43 EEST - 3.139.81.117